

**Surface Heterogeneity Effects on the Atmospheric
Boundary Layer: Parameterizations and Applications to
Wind Energy**

**A DISSERTATION
SUBMITTED TO THE FACULTY OF THE GRADUATE SCHOOL
OF THE UNIVERSITY OF MINNESOTA
BY**

Leonardo Chamorro

**IN PARTIAL FULFILLMENT OF THE REQUIREMENTS
FOR THE DEGREE OF
DOCTOR OF PHILOSOPHY**

Fernando Porté-Agel

August, 2010

© Leonardo Chamorro 2010
ALL RIGHTS RESERVED

Acknowledgements

I am heartily thankful to my advisor, Fernando Porté-Agel, whose support and encouragement enabled me to explore different aspects of the turbulent flows in the atmospheric boundary layer. It has been an honor to be his PhD student.

I would also like to thank and acknowledge all the people that directly and indirectly helped me in this process, in particular:

Professor Aldo Tamburrino at University of Chile for his support and encouragement to pursue graduate studies. Certainly, he made possible my academic life to be a reality.

Professor John Gulliver for his help and support from the beginning of my graduate studies.

Professors and friends at the Saint Anthony Falls Laboratory, Department of Civil Engineering, University of Minnesota.

Silberman family for their financial assistance through the Silberman Fellowship program.

The University of Minnesota Graduate School and the Doctoral Dissertation Fellowship program for financial assistance.

The rest of the final examining Committee, Professors Heinz Stefan and Jian Sheng for their willingness to always help.

Lastly, I would like to thank my parents, brothers and family for all their love, encouragement and their unconditional support through all this period.

ABSTRACT

Understanding the effects of surface roughness transitions on the spatial distribution of surface shear stress and velocity is key to improving predictions of turbulent transport in the atmospheric boundary layer (ABL). This is particularly important as a boundary condition for the design of wind energy projects.

In the first part of this research, the effects of surface roughness heterogeneity on the ABL were studied in the boundary layer wind tunnel of the Saint Anthony Falls Laboratory (SAFL) at the University of Minnesota. We specifically developed a numerical model that accurately predicts, for the first time, the change of wind velocity and surface shear stress downwind of a surface roughness transition. In this context, different surface boundary conditions for large-eddy simulation were tested downwind of a rough-to-smooth surface transition. Results show substantial differences between measured and modeled shear stress using standard boundary conditions based on the direct application of the similarity theory with local fluctuating filtered velocities. The best performance is obtained using the proposed model for estimating the adjustment of the mean velocity and surface shear stress downwind of the transition, while the surface shear stress fluctuations were modeled proportionally to the velocity fluctuations. This improves the prediction of the variance and spectrum of the fluctuating shear stress with respect to standard boundary conditions.

In the second part of this research, the complex interaction between the ABL and wind turbine wake(s) was studied in the SAFL wind tunnel using model wind turbines. The structure and behaviour of the turbulent flow around the wind turbines were characterized under both thermally neutral and stable stratifications. Non-axisymmetric behavior of turbulence statistics in the wake was observed in response to the non-uniformity of the incoming boundary layer flow. Nevertheless, the velocity deficit with respect to the average incoming flow was nearly axisymmetric everywhere except near

the surface in the far wake. In the wind farm scenario, results suggest that the turbulent flow can be characterized into two main regions. The first, located below the turbine top tip height, has a direct effect on the performance of turbines. Here the mean flow statistics appear to reach an equilibrium as close as 3-4 turbines downwind of the first turbine. In the second region, which is located immediately above the turbine top tips, flow adjustment is slower. Here, two distinct layers were found: an internal boundary layer where the flow starts to adjust to the new farm surface conditions, yet is still affected by the upwind flow characteristics; and an equilibrium layer, where the flow statistics are fully adjusted to the wind farm conditions. Our results also show that wind turbine wakes reduce the mean surface heat flux, where a large wind farm implied the most significant change. This observation points to the necessity of new parameterizations for large scale models.

Contents

Acknowledgements	i
Abstract	ii
List of Figures	vii
1 Introduction	1
1.1 The atmospheric boundary layer, surface heterogeneity, and implications for wind energy assessments	1
2 Velocity and surface shear stress distributions behind a rough-to- smooth surface transition: A simple new model	5
2.1 Introduction	6
2.2 Experimental set-up	9
2.3 Analysis of Elliott and Panofsky-Townsend models for surface shear stress	13
2.4 Alternative simple model for velocity and surface shear stress predictions	15
2.5 Evaluation of the new model	17
2.6 Summary	20
3 Wind-tunnel study of surface boundary conditions for large-eddy sim- ulation of turbulent flow past a rough-to-smooth surface transition	24
3.1 Introduction	25

3.2	Experimental set-up	29
3.3	Surface Shear Stress Model Analysis	32
3.4	Summary	44
4	A wind-tunnel investigation of wind-turbine wakes: Boundary-layer turbulence effects	47
4.1	Introduction	48
4.2	Experimental set-up	53
4.3	Wake characteristics	57
4.3.1	Wake in a rough-wall boundary layer	57
4.3.2	Wake in a smooth-wall boundary layer	70
4.4	Summary	74
5	Effects of thermal stability and incoming boundary-layer flow characteristics on wind-turbine wakes: A wind-tunnel study	77
5.1	Introduction	78
5.2	Experimental set-up	80
5.3	Wake properties	85
5.4	Summary	101
6	Flow structure around a variable size wind farm. A wind tunnel study	104
6.1	Introduction	105
6.2	Experimental set-up	107
6.3	Flow characterization	110
6.3.1	Mean velocity distribution	112
6.3.2	Turbulence intensity distribution	117
6.3.3	Other flow statistics	124
6.3.4	On the wind farm roughness	130
6.4	Summary	132

7	Wind-turbine wake effects on the surface heat flux in a stable boundary layer	134
7.1	Introduction	135
7.2	Experimental setup	136
7.3	Spatial distribution of Surface heat flux	142
7.3.1	Case of single turbine and simple 4-turbine array	142
7.3.2	Case of 12 by 3 wind turbine array	147
7.3.3	Summary	148
	Bibliography	150

List of Figures

2.1	Schematic of the rough-to-smooth transition and measurement locations (top) and photograph of the single hotwire and crosswire probes placed downwind of the surface transition (bottom).	12
2.2	Comparison between measured average surface shear stress and the predictions from the models of Elliott (Equation 2.2) and Panofsky-Townsend (Equation 2.6). Downwind distance is normalized with the boundary-layer height $\delta = 0.4$ m. Surface shear stress is normalized with its downwind equilibrium value (τ_0)	14
2.3	Measured and modeled surface shear stress obtained with Elliott's log-law model (Equation 2.2) using velocity measurements at different heights z . Downwind distance and height are normalized using the boundary-layer height $\delta = 0.4$ m. Surface shear stress is normalized with its downwind equilibrium value (τ_0)	15
2.4	Adjustment of wind velocity profiles behind rough-to-smooth transition ($z_{01} = 0.5$ mm, $z_{02} = 0.0064$ mm) measured in the wind tunnel (continuous lines correspond to predictions from the new model).	18

2.5	Measured and modeled surface shear stress obtained with Elliott’s log-law model (Equation 2.2) and the proposed new model using velocity measurements at two different heights. Downwind distance and height are normalized using the boundary-layer height $\delta = 0.4$ m. Surface shear stress is normalized with its downwind equilibrium value (τ_0)	18
2.6	Spatial distribution of the weighting factor λ as a function of downwind distance for three different vertical positions: (a) $z=13.5$ mm; (b) $z/\delta_i = 0.5$; and (c) $z/\delta_i = 0.75$. Dashed lines correspond to the model weighting factor as given by equation 13. The solid lines correspond to the ‘exact’ factor obtained from the measurements.	19
2.7	Wind velocity profiles behind rough-to-smooth transition. Dotted lines and opens symbols correspond to the measurements of Bradley (1968), while the solid lines are the predictions given by the new model.	21
2.8	Surface shear stress distribution measured in the field experiment of Bradley (1968) (symbols) and corresponding predictions obtained with the new model as well as Elliott’s and P-T’s models. (τ_s and τ_r are the smooth and rough surface shear stress respectively).	22
3.1	Schematic of the rough-to-smooth transition and measurement locations (top) and photograph of the single hotwire and crosswire probes placed downwind of the surface transition (bottom).	32
3.2	Representative box filtering application for the measured velocity and surface shear stress after transition at locations $x/\delta = 0.75$ and $z/\delta = 1.35/40$	34
3.3	Representative comparison of modeled and measured surface shear stress at $z/\delta = 1.35/40$ and $x/\delta = 0.75$. (a) SG model; (b) shifted-SG model; (c) local-SG model and (d) MKP model.	35
3.4	P.d.f. comparison between measured and modeled non-dimensional kinematic shear stress at $x/\delta = 0.5$ and $z/\delta = 1.35/40$	36

3.5	Measured and modeled surface shear stress obtained with log-law model and ChPA model using velocity measurements at two different heights. Downwind distance and height are normalized using the boundary layer depth $\delta = 0.4$ m. Surface shear stress is normalized with its downwind equilibrium value (τ_o)	37
3.6	Correlation function between measured and modeled surface shear stress using the SG model. (a) $z/\delta = 1.35/40$; (b) $x/\delta = 1.0$	38
3.7	Correlation function between modeled and measured surface shear stress using the local-SG model. (a) $z/\delta = 1.35/40$; (b) $x/\delta = 1.0$	39
3.8	Correlation between measured and modeled surface shear stress behind the transition. (a) $z/\delta = 1.35/40$; (b) $z/\delta = 2.45/40$	40
3.9	Normalized spectra of measured and modeled surface shear stress at $z/\delta = 1.35/40$ and $x/\delta = 1.0$ using filter sizes of $\Delta_F = \Delta z$ (left) and $\Delta_F = 2\Delta z$ (right).	41
3.10	MKP model: α -coefficient behaviour after roughness transition	42
3.11	Non-dimensional ratio of measured surface shear stress and its variance with distance	43
3.12	Third order moment (skewness) comparison between measured and modeled surface shear stress.	44
4.1	Schematic of the wind turbine (front and side views), coordinate system and measurement locations (top and middle), and photograph of the test section with the wind turbine (bottom).	55
4.2	Background characteristics of the turbulent boundary layer over both rough and smooth surfaces: normalized mean velocity (left), turbulence intensity (middle) and kinematic shear stress (right). The horizontal lines represent the turbine axis. Height is normalized with the turbine radius r	57

4.3	Non-dimensional cross-sectional distribution of the mean velocity at different downwind positions inside the wake over the rough surface. (a) $x/d = 3$; (b) $x/d = 5$; (c) $x/d = 10$; and (d) $x/d = 15$. The horizontal line represents the turbine axis.	59
4.4	Non-dimensional cross-sectional distribution of the velocity deficit at different downwind positions inside the wake over the rough surface. (a) $x/d = 3$; (b) $x/d = 5$; (c) $x/d = 10$; and (d) $x/d = 15$. The horizontal line represents the turbine axis.	60
4.5	Non-dimensional cross-sectional distribution of turbulence intensity at different downwind positions inside the wake over the rough surface. (a) $x/d = 3$; (b) $x/d = 5$; (c) $x/d = 10$; and (d) $x/d = 15$. The horizontal line represents the turbine axis.	61
4.6	Non-dimensional cross-sectional distribution of the added turbulence intensity at different downwind positions inside the wake over the rough surface. (a) $x/d = 3$; (b) $x/d = 5$; (c) $x/d = 10$; and (d) $x/d = 15$. Horizontal lines represent the top tip and bottom tip levels.	62
4.7	Normalized added turbulence quantities as a function of distance. Rough case.	63
4.8	Non-dimensional cross-sectional kinematic shear stress distribution over a rough boundary layer. (a) $x/d = 3$; (b) $x/d = 5$; (c) $x/d = 10$; and (d) $x/d = 15$. The horizontal line represents the turbine axis.	64
4.9	Contour of non dimensional kinematic shear stress distribution over a rough boundary layer at $x/d = 5$	65
4.10	Skewness of the streamwise velocity component at $y = 0$ and different positions downwind ($x/d = 3, 5, 10, 15$) and upwind of the turbine. Rough case. Horizontal lines represent the top tip and bottom tip levels.	67

4.11	Power spectrum of the streamwise velocity at different heights (top-tip level, hub height and bottom-tip level) and different downwind positions in the center plane of the wake ($y = 0$). (a) without turbine; (b) $x/d = 1$; (c) $x/d = 3$; (d) $x/d = 5$; (e) $x/d = 10$ and (f) $x/d = 15$	69
4.12	Non-dimensional cross-sectional distribution of the velocity deficit at different downwind positions inside the wake over the smooth surface. (a) $x/d = 3$; (b) $x/d = 5$; (c) $x/d = 10$; and (d) $x/d = 15$. The horizontal line represents the turbine axis.	70
4.13	Non-dimensional cross-sectional distribution of the added turbulence intensity at different downwind positions inside the wake over the smooth surface. (a) $x/d = 3$; (b) $x/d = 5$; (c) $x/d = 10$; and (d) $x/d = 15$. Horizontal lines represent the top tip and bottom tip levels.	72
4.14	Power spectrum of streamwise velocity at the top tip and $x/d = 1$	73
5.1	Background characteristics of the stable boundary layer: normalized mean velocity, mean temperature, turbulence intensity, kinematic shear stress and kinematic heat flux. The horizontal lines represent the turbine axis. Height is normalized with the turbine radius r	82
5.2	Schematic of the wind turbine (front and side views), coordinate system and measurement locations (top and middle), and photograph of the test section with the wind turbine (bottom).	84
5.3	Non-dimensional distribution of mean velocity downwind of the turbine at zero span in the neutral (top) and in the stable stratified (bottom) boundary layer. Horizontal-dashed lines represent the turbine bottom and top tip heights and dots indicate measurement locations.	86
5.4	Non-dimensional distribution of mean velocity (left plot) and velocity deficit (right plot) downwind of the turbine at zero span. Turbine in the neutral boundary layer. Horizontal-dotted lines represent the turbine bottom and top tip heights.	87

5.5	Normalized velocity deficit at hub height for the two stratification cases and its comparison with simple models.	89
5.6	Schematic of the cylindrical coordinate system and velocity components.	90
5.7	Turbulence intensity distribution downwind of the turbine at zero span in the neutral (top) and in the stable stratified (bottom) boundary layer. Horizontal-dashed lines represent the turbine bottom and top tip heights and dots indicate measurement locations.	91
5.8	Contours of turbulence intensity, σ_u/U_{hub} , (left) and non-dimensional kinematic shear stress, $-\overline{u'w'}/U_{hub}^2$, (right) distributions in the neutral boundary layer at $x/d = 5$. Dots indicate measurement locations.	92
5.9	Non-dimensional distribution of kinematic shear stress downwind of the turbine at zero span in the neutral (top) and in the stable stratified (bottom) boundary layer. Horizontal-dashed lines represent the turbine bottom and top tip heights and dots indicate measurement locations.	93
5.10	Turbulent energy production ($-\overline{u'w'}dU/dz$ component) at different positions downwind of the turbine (at zero span) in the neutral boundary layer (top) and in the stable boundary layer (bottom). Horizontal-dashed lines represent the turbine axes.	94
5.11	Power spectrum of velocity (streamwise and vertical components) at $x/d=1$ in the neutral and stable boundary layers. (a) Streamwise velocity spectrum in the neutral boundary layer; (b) Streamwise velocity spectrum in the stable boundary layer; (c) vertical velocity spectrum in the neutral boundary layer and (d) vertical velocity spectrum in the stable boundary layer	96

5.12	Measured and modelled power spectrum of the streamwise (u) and vertical (w) velocity components in the neutral boundary layer at the turbine top tip height. (a) u -component, incoming flow; (b) w -component, incoming flow; (c) $x/d = 1$, u -component; (d) $x/d = 1$, w -component; (e) $x/d = 5$, u -component and (f) $x/d = 5$, w -component.	98
5.13	Non-dimensional distribution of turbulent heat flux at different locations downwind of the turbine (at zero span) in the stable boundary layer. Horizontal dashed lines represent the turbine bottom and top tip heights and dots indicate measurement locations.	99
5.14	Mean temperature distribution ($^{\circ}C$) at different locations downwind of the turbine (at zero span) in the stable boundary layer. Horizontal dashed lines represent the turbine bottom and top tip heights and dots indicate measurement locations.	100
5.15	Power spectrum of the low frequency components of the radial velocity at the turbine hub height and $x/d = 1$: (a) neutral boundary layer; (b) stable boundary layer.	101
6.1	Schematic of the 10 by 3 wind turbine array. Turbine dimensions and measurement locations (top and bottom), and photograph of the test section with the turbines (middle).	111
6.2	Non-dimensional distribution of mean velocity around the wind farm with $S_x = 5$ (top) and normalized angular velocity distribution of the different wind turbines with $S_x = 5$ and $S_x = 7$ (bottom). Dots indicate measurement locations.	113
6.3	Normalized streamwise velocity component distribution (left) and its deficit (right) in the wind farm.	114
6.4	Non-adjusted (left) and adjusted (right) mean velocity profiles above the top tip in the wind farm at different locations ($S_x = 5$). Horizontal lines represent the turbine bottom and tip heights.	115

6.5	Normalized streamwise velocity component distribution in the wind farm. $S_x = 5$ (top) and $S_x = 7$ (bottom).	116
6.6	Turbulence intensity distribution around the wind farm. $S_x = 5$ (top) and $S_x = 7$ (bottom). Dots indicate measurement locations.	120
6.7	Turbulence intensity distribution in the wind farm at bottom, hub and top tip heights. $S_x = 5$ (top) and $S_x = 7$ (bottom).	121
6.8	Turbulence intensity distribution at different heights above the wind farm. (a) $z = 1.25H$; (b) $z = 1.5H$; (c) $z = 2H$. $H =$ turbine height. . .	123
6.9	Conceptual description of the different regions and layers in a wind farm.	124
6.10	Non-dimensional distributions of kinematic shear stress (top) and turbu- lent kinetic energy production (bottom) inside and above a 10-turbines wind farm ($S_x = 5$).	125
6.11	Non-dimensional distribution of kinematic shear stress at different heights above the wind farm. (a) $z = 1.25H$; (b) $z = 1.5H$; (c) $z = 2H$. $H =$ turbine height.	126
6.12	P.d.f. of streamwise velocity component at top tip height inside the wind farm ($S_x = 5$).	127
6.13	Power spectrum of the streamwise (u) and vertical (w) velocity compo- nents at top tip height inside the wind farm. (a) u -component at $x/d = 1$ behind the 1 st turbine ($S_x = 5$); (b) w -component at $x/d = 1$ behind the 1 st turbine; (c) u -component at $x/d = 1$ behind the 10 th turbine ($S_x = 5$); (d) w -component at $x/d = 1$ behind the 10 th turbine ($S_x = 5$); (e) u - component at $x/d = 1$ behind the 10 th turbine ($S_x = 7$); (f) w -component at $x/d = 1$ behind the 10 th turbine ($S_x = 7$).	129
6.14	Aerodynamic roughness length of the wind farm array for the case $S_x = 5$.	131

7.1	Experimental set-up for the single wind turbine and the 4-aligned wind turbine array cases. Wind turbine dimensions (top), measurement locations and photograph of the single wind turbine (middle) and its counterpart for the 4-turbine case (bottom).	138
7.2	Experimental set-up for the 12 by 3 wind turbine array. Photograph of the model wind farm (top) and measurement locations (bottom).	140
7.3	Angular velocity of the different turbines for the simple 4-turbine array normalized with respect to the first turbine.	141
7.4	Background characteristics of the incoming turbulent boundary layer: normalized mean velocity (left), kinematic shear stress (middle) and turbulent heat flux (right). The horizontal lines represent the turbine axis. Height is normalized with the turbine radius r	142
7.5	Spatial distribution of non-dimensional surface heat flux around a wind turbine placed in a stably stratified boundary layer over a smooth surface.	144
7.6	Non-dimensional surface heat flux distribution around a single wind turbine at zero span ($y = 0$).	144
7.7	Conceptual schematic of a wind turbine wake with the different mechanisms affecting surface heat flux distribution.	145
7.8	Spatial distribution of non-dimensional surface heat flux around a simple array of four aligned wind turbines placed in a stably stratified boundary layer over a smooth surface.	146
7.9	Non-dimensional surface heat flux distribution around the 4-turbine array at zero span ($y=0$).	147
7.10	Non-dimensional surface heat flux distribution of a single turbine in the wind farm.	148

Chapter 1

Introduction

1.1 The atmospheric boundary layer, surface heterogeneity, and implications for wind energy assessments

Air flow in the atmospheric boundary layer (ABL), which is the lowest layer of the atmosphere (approximately 1 km deep during the daytime to 100 m under stratified conditions), is highly turbulent and is strongly affected by local, non-linear interactions with topography and land-surface heterogeneity. This complex interplay between wind and the underlying terrain results in wind fields that can have large variability within short distances ($O(m)$) and short time scales ($O(s)$). Not surprisingly, the numerical modeling of such a system, needed to improve forecasts of air quality and assessments of wind energy resources, is a daunting task. Even in very high-resolution numerical models, such as large-eddy simulations (LES), where much of the surface heterogeneity is explicitly resolved, the surface boundary condition still requires the calculation of local surface shear stress and heat flux as a function of the local fluctuating velocity and temperature at the lowest computational grid points. These models currently rely on the application of Monin-Obukhov similarity theory [70]. However, the accuracy of this approach is questionable since this theory is only valid when applied over homogeneous

surfaces and for time-averaged quantities.

The benefits associated with improved predictions of ABL wind and turbulence over heterogeneous surfaces are particularly important during the design process of wind energy projects. Currently, this design (siting of turbines in the landscape) is commonly based on rather sparse wind information, namely average wind measurements (no turbulence) collected at one location, or predictions from numerical models that are either too simple (mass-conserving models) or have spatial and temporal resolutions that are too coarse to accurately predict local wind variability at turbine scales (mesoscale models). In addition to those issues, the complex interaction between the ABL and wind turbine(s) is not well understood. In particular, and from an engineering perspective, there are two characteristics that are of considerable interest: the velocity deficit, which is related to the power loss from the wind turbine; and the turbulence levels, which may affect flow-induced rotor loads on other turbines located downwind in a wind farm. Most of the formulations that describe the turbulence statistics behind a wind turbine assume axisymmetric properties in the wake, which could lead to important errors in the prediction of both mean power and dynamic loads. Considering the large investments made every year on new wind energy projects, a better understanding of the complex interplay between the ABL and wind turbines could have a significant impact on the energy production levels and, consequently, on the economic value and feasibility of those projects.

The development of improved models for the prediction of heterogeneous ABL turbulent flow, and a fundamental understanding of the complex interaction between the ABL and wind turbine(s) are the primary focus of this research work. The new framework will provide valuable understanding for optimal designs (turbine siting) of wind energy projects. The specific objectives of this research include: a) To develop a new physical model for the improved prediction of mean velocity and surface shear stress distributions over surface roughness transitions. This will be achieved via analysis of high-resolution turbulence data collected in the St. Anthony Falls Laboratory (SAFL)

atmospheric boundary layer wind tunnel, as well as the analysis of published field data.

b) To improve our understanding of the effects of boundary-layer turbulence on the performance of wind turbines and the behavior of wind turbine wakes under different thermal stability conditions. This will be achieved through analysis of high-resolution turbulence measurements collected around miniature wind turbines in the SAFL wind tunnel.

Each chapter of this thesis contains a complete stand-alone research article including abstract, introduction, results, analysis, and conclusions. Chapter 2 is devoted to the analysis and development of an improved parameterization for wind velocity and surface shear stress downwind of a rough-to-smooth surface transition. Wind velocity is estimated as a weighted average between two limiting logarithmic profiles: the first log law, which is recovered above the internal boundary layer height, corresponds to the upwind velocity profile; the second log law is adjusted to the downwind aerodynamic roughness and local surface shear stress, and it is recovered near the surface, in the equilibrium sublayer. Unlike other simple analytical models, the new model does not rely on the assumption of a constant or linear distribution for the turbulent shear stress within the internal boundary layer. The performance of the new model is tested with our wind-tunnel measurements and also with the field data of Bradley [16]. Compared with other existing analytical formulations, the proposed model shows improved predictions of both surface shear stress and velocity distributions at different positions downwind of the transition. In Chapter 3, different surface boundary conditions for large-eddy simulation are tested downwind of a rough-to-smooth surface transition. Results show substantial differences between measured and modeled shear stress using standard boundary conditions based on the direct application of the similarity theory (the log law under neutral conditions) with local fluctuating filtered velocities. Those differences affect both the average value as well as higher order statistics of the predicted surface shear stress. The best performance is obtained with a model that calculates the average surface shear stress using the new formulation, proposed in Chapter 2, and its

fluctuations proportional to the velocity fluctuations. The fundamental issues associated with the interaction between the boundary layer and horizontal axis wind turbines are addressed in Chapters 4 and 5. Thermal stability effects on the turbulent properties of a turbine wake are also included in chapter 5. Chapter 6 is devoted to the characterization of the turbulent flow inside and above a wind farm under neutral stratification. Results suggest that the turbulent flow can be characterized in two broad regions. The first, located below the turbine top tip height, has a direct effect on the performance of turbines. The mean flow statistics appears to reach an equilibrium as close as 3-4 turbines downwind of the first. In the second region, which is located above the turbine top tips, flow adjusts much more slowly. Two layers were found: an internal boundary layer where flow starts to adjust to the new farm condition and an equilibrium layer, where flow statistics are adjusted. Surface heat flux, one of the essential components in the hydrologic cycle [44], was found to be affected by the flow pattern imposed by wind turbine(s). Chapter 7 addresses this problem by studying different wind turbine configurations placed in a boundary layer under thermally stable stratification. Important changes in the local surface heat flux were found compared to the scenario without a turbine. A large wind farm produced a net reduction of surface heat flux in stable stratification by roughly 11 percent. This is a significant change, which motivates the development of new parameterizations for large scale models (e.g. weather models) when dealing with large arrays of wind turbines.

Chapter 2

Velocity and surface shear stress distributions behind a rough-to-smooth surface transition: A simple new model

A simple new model is proposed to predict the distribution of wind velocity and surface shear stress downwind of a rough-to-smooth surface transition. The wind velocity is estimated as a weighted average between two limiting logarithmic profiles: the first log law, which is recovered above the internal boundary layer height, corresponds to the upwind velocity profile; the second log law is adjusted to the downwind aerodynamic roughness and local surface shear stress, and it is recovered near the surface, in the equilibrium sublayer. The proposed non-linear form of the weighting factor is equal to $\ln(z/z_{01})/\ln(\delta_i/z_{01})$, where z , δ_i and z_{01} are the elevation of the prediction location, the internal boundary-layer height at that downwind distance, and the upwind surface roughness, respectively. Unlike other simple analytical models, the new model does not rely on the assumption of a constant or linear distribution for the turbulent shear

stress within the internal boundary layer. The performance of the new model is tested with our wind-tunnel measurements and also with the field data of Bradley. Compared with other existing analytical models, the proposed model shows improved predictions of both surface shear stress and velocity distributions at different positions downwind of the transition.

2.1 Introduction

Understanding the effects of surface roughness transitions on the spatial distribution of surface shear stress and velocity is key to improving predictions of turbulent transport in the atmospheric boundary layer (ABL). For example, most atmospheric numerical models require as a lower boundary condition the specification of the surface shear stress as a function of the grid-averaged velocity field. In large-scale numerical models, such as weather and climate models, the surface boundary condition needs to account for the effects of subgrid surface heterogeneity on the spatial distribution of the surface shear stress and its relation with the velocity in the surface layer [107, 98, 65, 33, 14]. In the case of higher resolution numerical models, such as large-eddy simulation (LES), where much of the surface heterogeneity is explicitly resolved, the surface boundary condition still requires the calculation of the local (spatially filtered) surface shear stress as a function of the filtered fluctuating velocity at the lowest computational grid points. Currently, these models rely on the application of Monin-Obukhov similarity theory (the logarithmic law under neutral conditions) using local values of the filtered velocity. However, the accuracy of this approach is questionable since similarity theory is strictly valid only when applied over homogeneous surfaces and considering averaged quantities. Improvement of these boundary condition parameterizations in simulations of ABL flow over heterogeneous surfaces requires a better understanding of the effects of surface roughness transitions on the relation between surface shear stress and velocity fields.

Several models with different levels of complexity have been proposed to estimate

the spatial distribution of surface shear stress and velocity after a roughness transition (e.g. [38, 72, 78, 99]). The simplest and most common analytical models, introduced by Elliott [38] and Panofsky and Townsend [78], were obtained assuming a constant and a linear vertical distribution (respectively) of the friction velocity within the internal boundary layer (IBL). Rao et al. [85] used a numerical approach based on the Reynolds-averaged Navier-Stokes equations with a second-order closure model that includes a set of differential transport equations for the components of the Reynolds stress tensor. Rao's simulated velocity and surface shear stress profiles showed good agreement with the experimental field measurements of Bradley [16]. Recently, Bou-Zeid et al. [15] used a small computational domain to perform a very high resolution large-eddy simulation of the same roughness transitions using Lagrangian dynamic subgrid-scale models and showed that the simulated surface shear stress fields agreed reasonably well with the experimental field data of Bradley [16].

A common simple approach used to relate surface shear stress and velocity in the surface layer is Elliott's model [38], which assumes that the downwind velocity profile is in equilibrium with the new surface and, therefore, follows a logarithmic profile all the way up to the top of the internal boundary layer (height δ_i),

$$U = \frac{u_{*2}}{k} \ln \left(\frac{z}{z_{02}} \right), \quad (2.1)$$

where U is the average velocity at elevation z , u_{*2} is the friction velocity, z_{02} is the downwind surface roughness, and k is the von Kármán constant. This equation can be derived by assuming a constant shear stress along the vertical for $z < \delta_i$ and an equilibrium value of unity for the nondimensional wind shear $\Phi_m = (kz/u_{*2})(\partial U/\partial z)$. For time-averaged surface shear stress (τ_s) predictions, Equation 2.1 can be written as

$$\tau_{s2} = - \left[\frac{kU}{\ln(z/z_{02})} \right]^2, \quad (2.2)$$

where $u_{*2} = \sqrt{-\tau_{s2}}$. It is important to note that, due to a constant vertical turbulent shear stress assumption, this model produces an unrealistically sharp stress discontinuity

at the top of the internal boundary layer $z = \delta_i$. For the IBL depth δ_i , Elliott proposed the following relation:

$$\eta = (0.75 - 0.03M') \xi^{0.8}, \quad (2.3)$$

where η , M' and ξ are non-dimensional parameters defined as $\eta = \delta_i/z_{02}$, $M' = \ln(z_{02}/z_{01})$ and $\xi = x/z_{02}$, z_{01} and z_{02} are the upwind and downwind aerodynamic surface roughness, respectively, and x is the distance measured from the roughness change.

To avoid an abrupt change in the surface shear stress at the internal boundary-layer height δ_i , Panofsky and Townsend [78] considered a linear variation of the friction velocity with respect to height within the IBL:

$$u_* = u_{*1} \left[(1 - S) + S \frac{z}{\delta_i} \right], \quad (2.4)$$

where $S = (u_{*1} - u_{*2})/u_{*1}$ is a nondimensional measure of the relative change in surface stress associated with the transition, and u_{*1} and u_{*2} are the upwind and downwind friction velocity respectively.

As in Elliott's model, the velocity and surface shear stress distributions are derived by assuming a value of unity for the nondimensional wind shear. This yields

$$\begin{aligned} U &= \frac{u_{*1}}{k} \left[(1 - S) \ln \left(\frac{z}{z_{02}} \right) + S \frac{z}{\delta_i} \right] \Leftrightarrow \\ U &= \frac{u_{*2}}{k} \ln \left(\frac{z}{z_{02}} \right) + \frac{u_{*1} - u_{*2}}{k} \left(\frac{z}{\delta_i} \right) \end{aligned} \quad (2.5)$$

which implies

$$\frac{\tau_{s2}}{\tau_{s1}} = \left[1 - \frac{kU/u_{*1} - \ln(z/z_{02})}{z/\delta_i - \ln(z/z_{02})} \right]^2, \quad (2.6)$$

where τ_{s1} and τ_{s2} are the upwind and downwind surface shear stresses, respectively. Note that Panofsky and Townsend's model (hereon referred also as P-T) requires an explicit estimation for the internal boundary-layer height δ_i . Panofsky and Townsend [78] proposed an IBL depth-fetch relationship given by

$$\begin{aligned}
4k^2(\xi - \xi_0)/\eta = & \ln\eta - 5 + \frac{1}{2}M + \frac{4 - \frac{7}{6}M - \frac{1}{4}M^2}{\ln\eta - 1 + \frac{1}{4}M} + \\
& + \frac{4 + \frac{7}{6}M + \frac{1}{24}M^2 + \frac{1}{16}M^3}{(\ln\eta - 1 + \frac{1}{4}M)^2}, \tag{2.7}
\end{aligned}$$

where $M = \ln(z_{01}/z_{02})$ and $\xi_0 = 0$ for $M = 1.65$ (smooth-to-rough transition) and $M = 2.17$ (rough-to-smooth transition). A recent review on this and other IBL height models can be found in Savelyev and Taylor [89].

Experience suggests that the predictions from both Elliott and P-T models can differ substantially from observations. This can be explained considering that, as shown by Rao et al. [85], the non-dimensional wind shear, dissipation length scale, mixing length scale, and ratio of stress to turbulent kinetic energy downwind of a roughness transition are found to differ significantly from their equilibrium values.

In this paper, a simple new analytical model is proposed to predict the spatial distribution of wind velocity and surface shear stress downwind of a rough-to-smooth surface transition. First, a wind-tunnel experiment is presented in Section 2.3. The experiment was designed to study the performance of different simple analytical models. In section 2.4, the models of Elliott and Panofsky-Townsend are tested, the proposed alternative new simple model is presented in Section 2.5, and its performance is evaluated in Section 2.6 using our wind-tunnel data as well as Bradley's field data. Finally, a summary is given in Section 2.7.

2.2 Experimental set-up

A rough-to-smooth surface transition has been designed and installed in the boundary-layer wind tunnel of the Saint Anthony Falls Laboratory at the University of Minnesota, U.S.A. with the goal of studying the performance of different models for the spatial distribution of wind velocity and surface shear stress downwind of the transition. The boundary-layer wind tunnel has a plan length of 37.5 m with a main test section fetch of

roughly 15 m. There is a contraction with a 6.6:1 area ratio upwind of the test section along with flow conditioning/turbulence control consisting of a coarse wire mesh and honeycomb flow-straightened. The tunnel is driven by a 200 horse-power fan and is operated as a closed return loop. The turbulence intensity in the centre of the wind tunnel is approximately 0.25% for a 10 m s^{-1} freestream velocity. More details on the wind tunnel can be found in Carper and Porté-Agel [23].

Wind-tunnel flow velocity was measured using Pitot static tubes (mainly for calibration) and constant temperature anemometry (CTA). Two types of CTA were considered: single-normal (SN) and crosswire (XW or x-wires) probes. The probes are made with $5.0 \mu\text{m}$ tungsten wire and are connected to an A.A. Lab Systems AN-1003 10-channel CTA system. During the calibration and measurements the temperature fluctuations were kept within a $\pm 0.5^\circ\text{C}$ range to avoid bias errors due to thermal drift of the voltage signal.

The rough-to-smooth transition was created by placing 7 m length of wire mesh on the wind-tunnel floor upstream of a smooth flat plate. The woven-wire mesh is considered a k-type roughness (see Jimenez [54]) and has an average height $k_0 = 3 \text{ mm}$ with an aerodynamic roughness length $z_{01} = 0.5 \text{ mm}$.

A turbulent boundary layer is developed upstream with the help of a tripping mechanism (80 mm picket fence) located at the exit of the wind-tunnel contraction where the test section begins. The turbulent boundary layer is allowed to grow in zero pressure gradient conditions by adjustment of the wind-tunnel ceiling. The upstream roughness induces a strong change in the momentum flux near the surface, maintaining a well-developed surface layer with constant shear stress and a logarithmic velocity profile. The experiments were conducted with a 10 m s^{-1} freestream flow velocity and a turbulent boundary-layer depth of $\delta = 0.4 \text{ m}$ at the roughness transition location.

A SN hotwire (boundary-layer type) probe and a crosswire anemometer were used to measure surface shear stress and wind velocity (respectively) at different positions downstream of the transition ($x/\delta = 0.1, 0.15, 0.2, 0.25, 0.375, 0.5, 0.75, 1.0$ and 1.5)

and various heights (for the crosswire) within the internal boundary layer. A schematic and photograph of the experimental set-up are shown in Figure 3.1. The single hotwire was placed in the viscous sublayer, directly over the smooth surface. This procedure is well established and has been used in previous experimental studies by Alfredsson et al. [4], Chew et al. [32] and Khoo et al. [57]. Here, the sensor was calibrated against a Preston tube following the procedure introduced by Patel [79]. During data collection the two sensors' voltage signatures were sampled simultaneously at a rate of 20 kHz for a measurement period of 60 s.

A review of rough-wall boundary layers by Jimenez [54] and an experimental study by Castro et al. [24] suggest that the boundary layer behaves differently depending on the ratio of boundary-layer height (δ/k_0), with a change in behaviour when $\delta/k_0 > 80$, which is typical for ABL. Previous wind-tunnel experiments [5, 72, 31, 24] have provided valuable results but use δ/k_0 on the order of 20. These relatively low ratios of boundary-layer height to roughness element height are not typical for land surface transitions because the effect of their roughness elements reaches further into the wind-tunnel boundary layer than does the effect of rough terrain in the ABL. Thus, the roughness chosen in those wind-tunnel studies may not provide a large enough range of length scales to allow a true equilibrium surface layer to develop. The set-up used in this study maintains a $\delta/k_0 = 133$ to ensure that inner and outer scales of the boundary layer, and hence its structure, are well developed.

The zero pressure gradient boundary layer, developed upstream of the transition, had a Reynolds number based on the surface shear stress of $Re_\nu = u_*\delta/\nu \approx 1.5 \times 10^4$, a boundary-layer thickness of $\delta = 0.4$ m, a friction velocity of $u_{*1} = 0.55$ m s⁻¹ and a freestream velocity $U_1 = 10$ m s⁻¹. In this condition, the upwind transition boundary layer is in the fully rough regime [54]. The smooth surface consists of the finished wooden floor of the tunnel with a window of flat plate that lies flush and sealed with the floor. A boundary layer forming over only the smooth floor has approximately the same height as the boundary layer over the rough surface but with a friction velocity

$$u_{x2} = 0.32 \text{ m s}^{-1}.$$

Calibrations of the single and crosswire anemometers were performed at the beginning of the experiment run. The crosswire was calibrated in the freestream region against a Pitot-static probe, at seven angles for each of seven velocities. A cubic-spline table calibration method was then used to determine the two instantaneous velocity components from the two instantaneous voltage signatures. For more details on the crosswire calibration see Bruun [18]. Calibration of the single hotwire against a Preston tube [79] was carried out using ten different velocities. The single hotwire and Preston tube were placed over a smooth flat plate in the freestream region to avoid any disturbance.

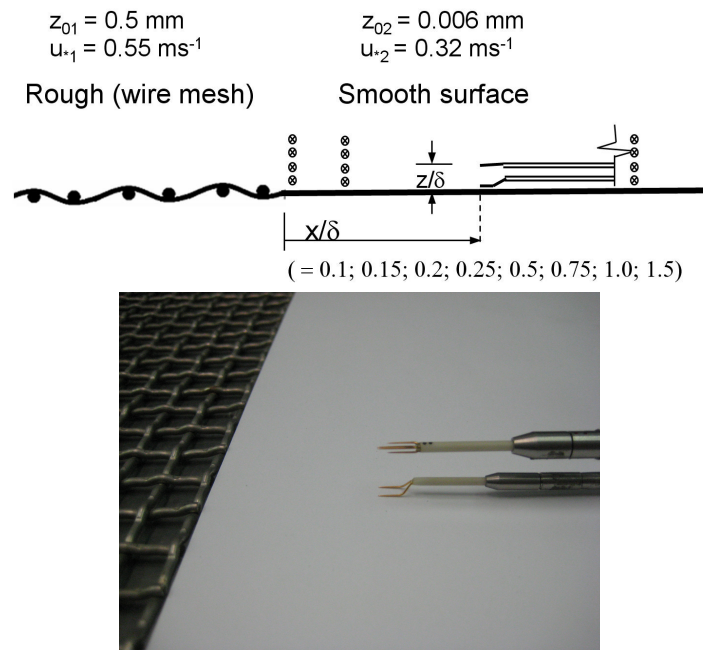


Figure 2.1: Schematic of the rough-to-smooth transition and measurement locations (top) and photograph of the single hotwire and crosswire probes placed downwind of the surface transition (bottom).

2.3 Analysis of Elliott and Panofsky-Townsend models for surface shear stress

The average surface shear stress measured with the single hotwire, normalized with the equilibrium downwind surface shear stress (τ_o), is plotted in Figure 2.2 as a function of the normalized distance downwind from the transition. As expected, the shear stress increases with distance from the transition and asymptotes to the equilibrium shear stress on the smooth surface. At a distance slightly larger than the boundary-layer depth, the shear stress is close to its equilibrium value. The surface shear stress predicted with the Elliott and P-T models, using the velocity measured at a height of $z = 13.5$ mm in Equations 2.2 and 2.6, respectively, are also plotted in Figure 2.2 for comparison. Both models clearly underestimate the value of the surface shear stress at each of the downwind locations under consideration.

It is important to notice that P-T's surface shear prediction should always be smaller than Elliott's prediction when they are based on the velocity at the same height. This is due to the fact that the P-T model (Equation 2.5) adds a positive term to Elliott's velocity relation, which necessarily implies a lower surface shear stress.

Ideally, the surface shear stress prediction, obtained with any given model, should have no (or small) dependence on the height at which the velocity is measured. Figure 2.3 shows Elliott's surface shear stress prediction at different downwind positions using velocities measured at different heights. From this it is clear that Elliott's surface shear stress prediction is strongly dependent on the height at which the model is applied. It is interesting to note that the prediction improves as the considered height approaches the IBL height. P-T's surface shear stress predictions were also found to have a similar strong dependence (not shown here) on the height at which the model is applied.

A particular case of Elliott's approach is given by Jensen [53], who proposed an expression for the ratio between downwind and upwind shear stresses (τ_{s2}/τ_{s1}) based on applying Elliott's equation at $z = \delta_i$:

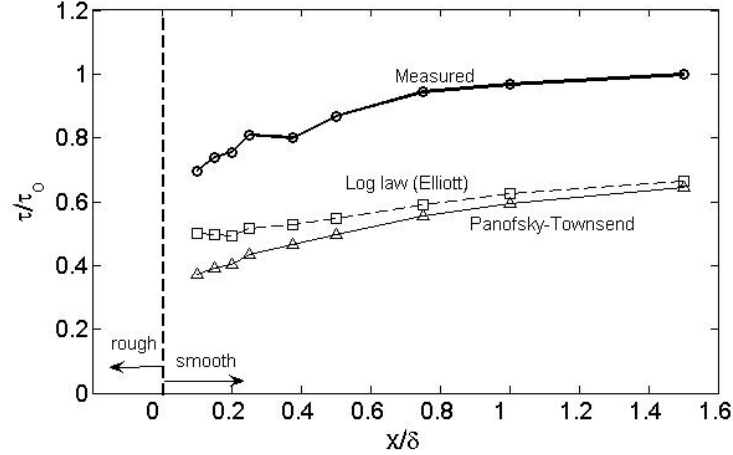


Figure 2.2: Comparison between measured average surface shear stress and the predictions from the models of Elliott (Equation 2.2) and Panofsky-Townsend (Equation 2.6). Downwind distance is normalized with the boundary-layer height $\delta = 0.4$ m. Surface shear stress is normalized with its downwind equilibrium value (τ_0)

$$\frac{\tau_{s2}}{\tau_{s1}} = \left[1 - \frac{M}{\ln(\delta_i/z_{02})} \right]^2. \quad (2.8)$$

As shown in Figure 2.3, this relation yields the right trend in the surface shear stress, but (in this case) it underestimates its magnitude by about 15% at all positions downwind of the transitions. It is important to note that, in order to use this model, an estimate for the internal boundary-layer height is required. In Figure 2.3, for the case of $z = \delta_i$ (Jensen’s model), the IBL growth equation proposed by Elliott (Equation 2.3) has been used. Note that, unlike Elliott and P-T parameterizations, Jensen’s model cannot predict the velocity distribution throughout the IBL.

Previous studies (e.g. [16]) suggest that vertical velocity profiles downwind of a roughness transition have a log-nonlinear behaviour, which differs from the log-linear models of Elliot and P-T. Next we propose a simple model that attempts to reproduce the log-nonlinear velocity distribution pattern observed within the internal boundary

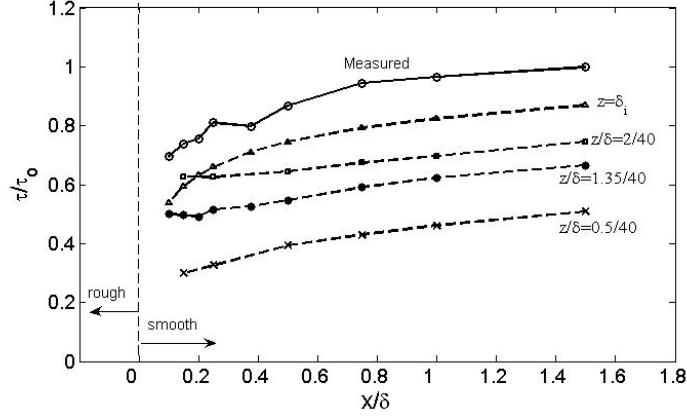


Figure 2.3: Measured and modeled surface shear stress obtained with Elliott’s log-law model (Equation 2.2) using velocity measurements at different heights z . Downwind distance and height are normalized using the boundary-layer height $\delta = 0.4$ m. Surface shear stress is normalized with its downwind equilibrium value (τ_0)

layer.

2.4 Alternative simple model for velocity and surface shear stress predictions

As pointed out by Garratt [43], the observed behaviour of velocity profiles within internal boundary layers suggests that they might be described through a modified logarithmic law of the general form

$$U = \frac{u_{*2}}{k} \ln \left(\frac{z}{z_{02}} \right) + f(z/\delta_i), \quad (2.9)$$

where the function $f(z/\delta_i)$ should have the following limiting values

$$f = \begin{cases} \frac{u_{*1}}{k} \ln \left(\frac{z}{z_{01}} \right) - \frac{u_{*2}}{k} \ln \left(\frac{z}{z_{02}} \right), & z/\delta_i \geq 1 \\ 0, & z/\delta_i \ll 1. \end{cases} \quad (2.10)$$

The limiting values for $f(z/\delta_i)$ reflect the effect of boundary conditions given by the

upstream logarithmic velocity profile at z/δ_i and the equilibrium logarithmic velocity profile close to the downwind surface.

One possible simple formulation for the function $f(z/\delta_i)$ that satisfies the conditions given by Equation 2.10 can be obtained by weighting the function $f(z/\delta_i)$ by a non-dimensional parameter λ such that $0 < \lambda < 1$ for $z/\delta_i < 1$. This yields the following equation for the velocity distribution within the IBL:

$$U \approx \frac{u_{*2}}{k} \ln \left(\frac{z}{z_{02}} \right) + \lambda \left(\frac{u_{*1}}{k} \ln \left(\frac{z}{z_{01}} \right) - \frac{u_{*2}}{k} \ln \left(\frac{z}{z_{02}} \right) \right), \quad (2.11)$$

which can also be written as

$$U \approx (1 - \lambda) \frac{u_{*2}}{k} \ln \left(\frac{z}{z_{02}} \right) + \lambda \frac{u_{*1}}{k} \ln \left(\frac{z}{z_{01}} \right). \quad (2.12)$$

Note that Equation 2.12 implies that $u(z)$ is estimated as a combination of two limiting log laws, one corresponding to the upwind velocity profile and the second corresponding to the so-called equilibrium sublayer, where the flow is in equilibrium with the downwind surface. In order to satisfy the conditions given in Equation 2.10, the weighting parameter λ should increase monotonically as z/δ_i increases. Our wind-tunnel measurements (Figure 2.4) and also previous studies (e.g., [16]) suggest that λ does not follow strictly a linear relation in terms of z/δ_i . In order to obtain a simple expression for the non-dimensional parameter λ , it is important to identify the variables that have a dominant effect in the shape of the velocity profile. In addition to z and δ_i , previous studies (e.g. [108]) have shown that the largest of the two aerodynamic roughnesses, z_{01} , is the more relevant parameter of the two. Taking this into consideration, a simple non-linear monotonically increasing function that satisfies the limiting conditions in Equation 2.10 and induces a non-linear log velocity profile behaviour is

$$\lambda = \ln(z/z_{01})/\ln(\delta_i/z_{01}). \quad (2.13)$$

2.5 Evaluation of the new model

Figure 2.4 shows a comparison between mean velocity profiles measured downwind of the rough-to-smooth transition and the corresponding profiles estimated using the simple new formulation given by Equations 2.12 and 2.13. Our results show an excellent agreement between modelled and measured velocities. It is important to observe that the velocity profiles do not follow a logarithmic law within the IBL. In fact, velocity profiles show a clear curvature (log-nonlinear behaviour) that cannot be reproduced by Elliott's log-law model.

Next, we evaluate the performance of the model to predict the local value of the surface shear stress as a function of the velocity at different locations in the IBL. Figure 3.5 shows a comparison between the surface shear stress measured at different positions downwind of the surface transition and the estimated surface shear stress obtained using the new formulation with the velocity measured at $z = 5$ and 13.5 mm. For comparison, results from the Elliott's model are also included. The new model markedly improves the surface shear stress prediction. Moreover, the prediction of the new model shows very small dependence on the height in the IBL at which the model is applied. Despite the remarkable performance of the model to capture the evolution of the surface shear stress near the transition, the model is found to overestimate the value of the equilibrium value of the surface shear stress away from the transition by nearly 15%.

In order to gain further insight on the performance of the new model, in Figure 2.6 the value of the parameter λ obtained with the new model (Equation 2.12) is compared with the 'exact' value calculated from the measured velocity. The value of λ is presented as a function of distance from the transition (x/δ_i) and for three different heights ($z = \text{constant} = 13.5$ mm, $z/\delta_i = 0.5$, and $z/\delta_i = 0.75$, respectively). Note that for a given height (e.g., $z = 13.5$ mm), the value of λ decreases with downwind distance (Figure 2.6a). This is consistent with the fact that, at that height, the wind velocity becomes more adjusted to the downwind surface and, consequently, the model should have a

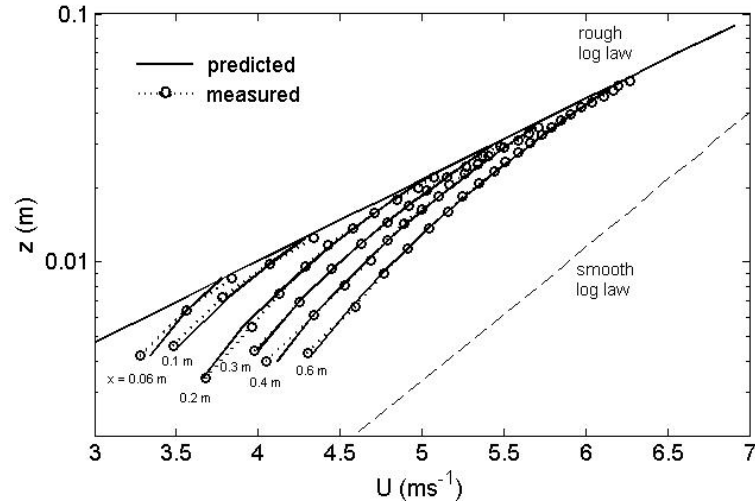


Figure 2.4: Adjustment of wind velocity profiles behind rough-to-smooth transition ($z_{01} = 0.5$ mm, $z_{02} = 0.0064$ mm) measured in the wind tunnel (continuous lines correspond to predictions from the new model).

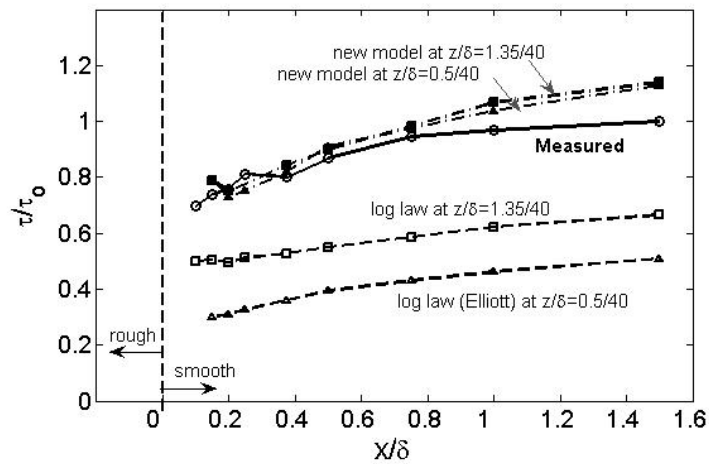


Figure 2.5: Measured and modeled surface shear stress obtained with Elliott's log-law model (Equation 2.2) and the proposed new model using velocity measurements at two different heights. Downwind distance and height are normalized using the boundary-layer height $\delta = 0.4$ m. Surface shear stress is normalized with its downwind equilibrium value (τ_0)

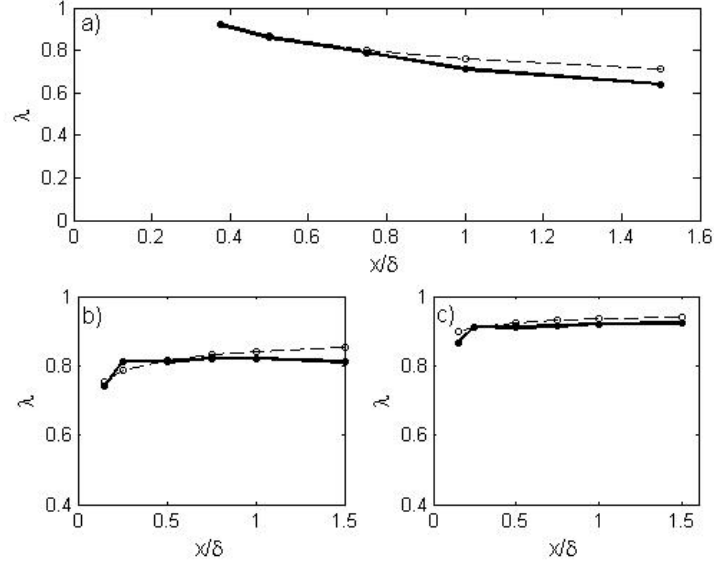


Figure 2.6: Spatial distribution of the weighting factor λ as a function of downwind distance for three different vertical positions: (a) $z=13.5$ mm; (b) $z/\delta_i = 0.5$; and (c) $z/\delta_i = 0.75$. Dashed lines correspond to the model weighting factor as given by equation 13. The solid lines correspond to the 'exact' factor obtained from the measurements.

larger relative contribution from the downwind log law (smaller λ in Eq. 2.12). In Figure 2.6b, c the value of λ is nearly constant due to the fact that the height relative to the boundary layer (z/δ_i) remains constant. In all cases, the new model is able to capture the spatial distribution of λ , which is key to the good performance of the model shown in Figures 2.4 and 3.5.

In order to further test the performance of the new formulation, we have also used the field data of Bradley [16]. In that experimental study, surface shear stress distribution and wind velocity profiles were carefully characterized downwind of a spikes-to-tarmac transition. The surface roughnesses estimated by Bradley [16] were $z_{01} = 2.5$ mm for the spikes and $z_{02} = 0.02$ mm for the tarmac. In a later study, Nemoto [73] showed that the values of z_{01} , estimated from Bradley's velocity profiles, range from 1.4 mm to 0.08

mm and those of z_{02} range from 0.015 mm to 0.0023 mm. This was later corroborated by Rao et al. [85] who reported that values of z_{02} in the range 0.0002 to 0.05 mm are equally plausible. He attributed this wide scatter for the smooth surface due to the difficulty associated with extrapolating the neutral equilibrium wind profile data. In this comparison, we follow the same procedure considered by Nemoto [73], i.e., we analyze each profile and adjust z_{01} to the velocity profile. The roughness z_{02} is estimated from the farthest velocity profile, which is better adjusted to the downwind roughness.

Figure 2.7 shows the comparison between the wind velocity profiles measured by Bradley at different positions ($x = 2.1, 4.0, 6.1$ and 8.3 m) downwind of the transition and the velocity profiles predicted with the new model. The modeled velocity profiles show overall good agreement with the measurements. In Figure 2.8, the prediction of the surface shear stress obtained with the new model is compared with the measurements of Bradley for different positions downwind of the surface transition. The modeled shear stress falls within the range of the measurements except for the further distance, where, as in the case of the wind-tunnel comparison, the model appears to slightly overestimate the value of the surface shear stress. These results contrast with Elliot's and P-T's predictions (also presented by Bradley and included in Figure 2.8) that systematically underestimate the surface shear stress at all positions.

2.6 Summary

A simple new model is proposed to describe the distribution of wind velocity and surface shear stress downwind of a rough-to-smooth surface transition. The wind velocity is calculated as a weighted average between two limiting logarithmic profiles: the first log law, which is recovered above the internal boundary-layer height, corresponds to the upwind velocity profile; and the second log law is adjusted to the downwind aerodynamic roughness and local surface shear stress, and it is recovered near the surface in the equilibrium sublayer. The proposed non-linear form of the weighting factor is equal to

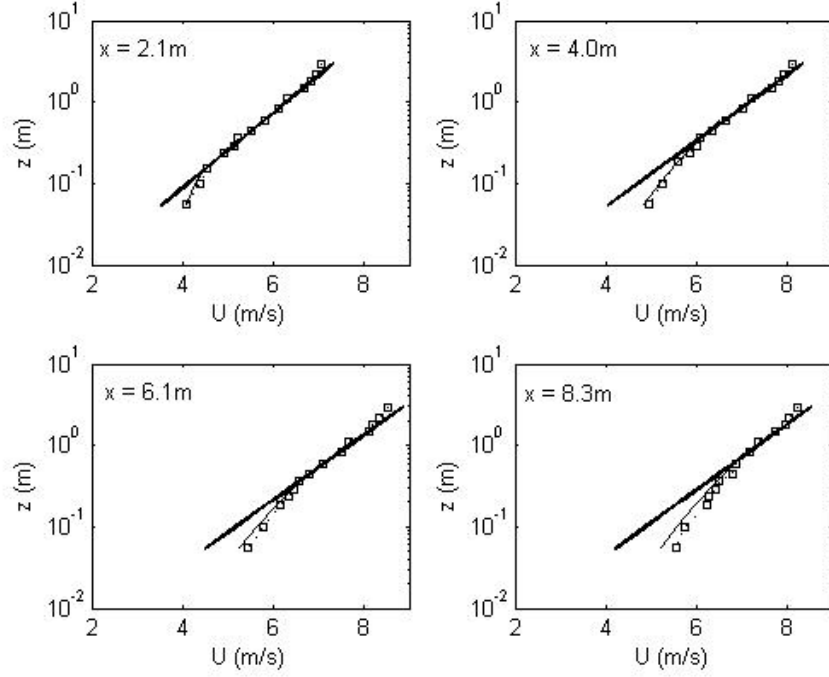


Figure 2.7: Wind velocity profiles behind rough-to-smooth transition. Dotted lines and opens symbols correspond to the measurements of Bradley (1968), while the solid lines are the predictions given by the new model.

$\ln(z/z_{01})/\ln(\delta_i/z_{01})$, where z , δ_i and z_{01} are the elevation of the prediction location, the internal boundary-layer height at that downwind distance, and the upwind surface roughness, respectively. Unlike other simple analytical models, the new model does not require the assumption of a constant or linear distribution for the turbulent shear stress within the internal boundary layer. By setting the weighting factor to zero, Elliott's model is recovered.

The performance of the new model is tested with our wind-tunnel measurements and also with the field data of Bradley [16]. The ability of the new model to reproduce both the surface shear stress and the velocity distributions is compared with other existing analytical models, namely Elliott's and P-T's models. These two models are

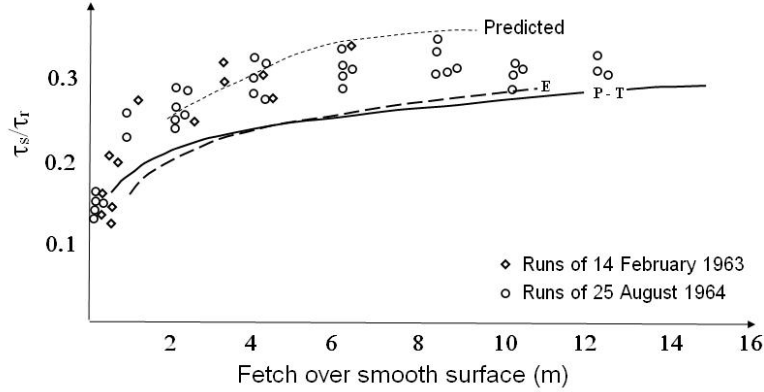


Figure 2.8: Surface shear stress distribution measured in the field experiment of Bradley (1968) (symbols) and corresponding predictions obtained with the new model as well as Elliott’s and P-T’s models. (τ_s and τ_r are the smooth and rough surface shear stress respectively).

found to underestimate the surface shear stress calculated using the wind velocity measured at different heights within the IBL. In addition, prediction of the surface shear stress obtained with both models shows a strong dependence on height. When the height approaches the internal boundary-layer depth δ_i , Elliott’s prediction improves. This particular case corresponds to the model of Jensen [53]. However, Elliott’s model consistently underestimates the surface shear stress when applied using the velocity at lower locations within the internal boundary layer. This underestimation is even more pronounced for the P-T model due to the fact that, by construction (Eq. 2.5), P-T’s model always predicts a smaller surface shear stress than Elliott’s model for any given height and corresponding velocity. The proposed new model yields surface shear stress distributions that are more realistic and, at the same time, have a much smaller dependence on height, compared with the predictions from the models of Elliott and P-T. These results highlight the potential of the new model for use in improved parameterizations for the surface shear stress in large-eddy simulations of turbulent boundary-layer

flows over heterogeneous surfaces. The new model is also found to capture the measured downwind evolution of the velocity profiles (including their curvature) with remarkable accuracy.

Future research will focus on developing and testing a similar model for smooth-to-rough surface transitions. In addition, tests will be performed to assess the potential of the new models to be implemented in surface boundary conditions for large-eddy simulations of boundary-layer flow over heterogeneous surfaces. These boundary conditions, used to calculate the local value of the surface shear stress as a function of the velocity, are currently based on direct application of similarity theory (i.e., the log law under neutral stability conditions).

Chapter 3

Wind-tunnel study of surface boundary conditions for large-eddy simulation of turbulent flow past a rough-to-smooth surface transition

A wind-tunnel experiment was performed to test surface boundary condition formulations for large-eddy simulation (LES) downwind of a rough-to-smooth surface transition in a turbulent boundary layer for $Re_\tau \approx 1.5 \times 10^4$. Single and x-wire anemometers were used to obtain simultaneous high-resolution measurements of surface shear stress and wind velocity at different heights and positions downwind of the transition. One-dimensional filtering, using Taylor's hypothesis, was used to obtain filtered signals of

both velocity and surface shear stress. Experimental results show substantial differences between measured and modeled shear stress using standard boundary conditions based on the direct application of the similarity theory (the log-law under neutral conditions) with local fluctuating filtered velocities. Those errors affect both the average value as well as higher order statistics of the predicted surface shear stress. The best performance is obtained with a model that calculates the average surface shear stress using a modified log-law that accounts for the adjustment of the mean velocity and surface shear stress downwind of the transition. The surface shear stress fluctuations are modeled proportional to the velocity fluctuations, which improves the prediction of the variance and spectrum of the fluctuating shear stress with respect to standard boundary conditions. The optimum value of the proportionality coefficient in that model is found to be slightly larger than the one reported for homogeneous boundary layers, and it has only a small dependence on distance from the transition.

3.1 Introduction

Large-eddy simulation (LES) has become a powerful tool to study turbulent fluxes of momentum and scalars (heat, water vapor and pollutants) in the atmospheric boundary layer -ABL- (e.g., [9, 49, 2, 87, 59, 95]). Despite the potential of LES, there are critical issues that need to be improved in order to make better prognostics. In particular, one of the main issues that affect LES performance is the treatment of the surface boundary condition. Due to the high Reynolds number of ABL flows, the lowest grid point is necessarily far away from the viscous sublayer, and typically in the so-called surface layer (logarithmic layer in homogeneous neutrally-stratified boundary layers). As a result, the surface boundary condition must account for all small scale and complex dynamic processes occurring between the surface and the first grid point. The most common boundary condition formulations for LES of ABL flows calculate the fluctuating (filtered) surface shear stress from the resolved (filtered) horizontal velocity at the lowest

grid point using similarity theory (the log-law under neutral conditions). However, the validity of this approach is questionable since similarity theory is strictly only valid for averaged quantities in homogeneous and stationary flows.

Different models have been proposed to predict the instantaneous surface shear stress over homogeneous surfaces (e.g. [91, 45, 82, 63]). One of the most common models for surface shear stress $\tau_{i3,s}(x, y, t)$ (where the subscripts $i=1$ and 2 represent the streamwise (x) and spanwise (y) components, respectively, and the subscript s denotes a surface value) used in LES of high-Reynolds-number boundary layer flows [91, 45, 82, 81] is:

$$\tau_{i3,s}(x, y, t) = \langle \tau \rangle \frac{\tilde{u}_i(x, y, z, t)}{U(z)} \quad (i = 1, 2), \quad (3.1)$$

where $(\tilde{})$ denotes the spatial filtering operation, the angular brackets $(\langle \rangle)$ indicate an averaging operation (typically over horizontal planes for homogeneous boundary layer simulations), $\langle \tau \rangle$ is the mean surface shear stress, $U(z)$ is the mean horizontal wind velocity at height z , and \tilde{u}_i is the instantaneous (filtered) velocity in the i -direction.

The mean surface shear stress $\langle \tau \rangle$ and velocity $U(z)$ are related through the similarity theory [70]:

$$U(z) = \frac{u_*}{k} \ln \left(\frac{z}{z_0} \right), \quad (3.2)$$

where z_0 is the local aerodynamic roughness length, k is the von Kármán constant (≈ 0.4), $u_*(= \sqrt{-\langle \tau \rangle})$ is the friction velocity. Then, Equation 3.1 can be written as

$$\tau_{i3,s}(x, y, t) = - \left[\frac{U(z)k}{\ln \left(\frac{z}{z_0} \right)} \right] \left[\frac{\tilde{u}_i(x, y, z, t)k}{\ln \left(\frac{z}{z_0} \right)} \right]. \quad (3.3)$$

Hereon this model will be referred to as the Schumann-Grötzbach (SG) model.

An alternative expression for the SG model is the well-known shifted Schumann-Grötzbach (shifted-SG) model. In this model, the instantaneous filtered velocity signature is shifted in the streamwise direction to improve the correlation with surface shear

stress. The shift (or displacement) applied to the velocity agrees with the idea that coherent structures in the surface layer are inclined with respect to the surface [82]. These coherent structures have been found in experiments and direct numerical simulations (DNS). Recent field studies (e.g. [22], [62]) have shown that the inclination of the flow structures in the ABL is very similar to the one reported in lower Re boundary layer flows (e.g., [17, 82]). The shifted-SG model is defined as:

$$\tau_{i3,s}(x, y, t) = \langle \tau \rangle \frac{\tilde{u}_i(x + \Delta_s, y, z, t)}{U(z)}, \quad (3.4)$$

where Δ_s is a streamwise displacement. Piomelli et al. [82] found, using direct numerical simulation (DNS), the shifted-SG model to be an improvement over the standard SG model. They suggest using $\Delta_s = z \cot(\gamma)$, where $8^\circ < \gamma < 13^\circ$ is the inclination of flow structures with respect to the surface (where the correlation between shear stress at the surface and velocity reaches a maximum along a plane inclined at approximately that angle). An experiment performed by Rajagopalan and Antonia [84] also showed this 'optimum' displacement.

Another common boundary condition model in ABL flow simulations, which does not require the flow to be homogeneous (to calculate $\langle \tau \rangle$), consists of using the log-law to compute the magnitude of the instantaneous local (resolved) surface shear stress as a function of the resolved velocity in the nearest grid point above the surface [69, 64, 3]:

$$\tau_s(x, y, t) = - \left[\frac{\tilde{u}_r(x, y, z, t)k}{\ln(z/z_0)} \right]^2, \quad (3.5)$$

where $\tilde{u}_r(x, y, z, t) = (\tilde{u}_1^2 + \tilde{u}_2^2)^{1/2}$ is the instantaneous (resolved) horizontal velocity magnitude. The two components of the surface shear stress vector are calculated using:

$$\tau_{i3,s}(x, y, t) = \tau_s(x, y, t) \frac{\tilde{u}_i(x, y, z, t)}{\tilde{u}_r(x, y, z, t)}. \quad (3.6)$$

Equation 3.6 can be written, using Equation 3.5, as:

$$\tau_{i3,s}(x, y, t) = \left[\frac{k}{\ln(z/z_0)} \right]^2 \tilde{u}_i(x, y, z, t) \tilde{u}_r(x, y, z, t). \quad (3.7)$$

Here the average surface shear stress is not necessarily preserved even when it is used in homogeneous boundary layer flows. Hereon this model will be referred to as the local-SG model.

Marusic et al. [63] used wind velocity and shear stress data collected in a wind-tunnel experiment to evaluate *a priori* the performance of different boundary condition formulations in a homogeneous boundary layer flow. In that study, the SG and shifted-SG models clearly underestimated the level of fluctuations of the surface shear stress and its spectral energy at all scales, compared with the measured stress. Motivated by their results, they proposed a new model (hereon referred to as MKP model) that aims at matching not only the average shear stress, but also the variance and energy spectrum. The proposed expression for the shear stress is of the form:

$$\tau_{i3,s}(x, y, t) = \langle \tau \rangle \frac{\langle \tilde{u}_i(z) \rangle}{U(z)} - \alpha u_* [\tilde{u}_i(x + \Delta_s, y, z, t) - \langle \tilde{u}_i(z) \rangle], \quad (3.8)$$

where α is a characteristic coefficient, which is expected to have only weak dependence on Reynolds number and the aerodynamic roughness length. Marusic et al. [63] found a value of $\alpha \approx 0.1$ provided the best match between modeled and measured filtered shear stress. Recently *a posteriori* simulations of homogeneous atmospheric boundary layers with the MKP model have also found an optimum value of $\alpha = 0.1$ [96].

It is important to note that all of the above boundary condition formulations calculate the average surface shear stress using similarity theory (the log-law under neutral stability conditions). As mentioned earlier, similarity theory is strictly only valid over homogeneous surfaces. In a recent *a priori* wind-tunnel study, Chamorro and Porté-Agel [25] demonstrated that large errors can result from the application of the log-law for the prediction of average surface shear stress downwind of a rough-to-smooth surface transition. This is due to the fact that a large fraction of the internal boundary layer

(IBL, i.e., the layer of flow that is affected by the downwind surface) velocity field is transitioning and, therefore, is not fully adjusted to the downwind surface. Indeed the velocity is in equilibrium with the surface, and thus follows the log-law, only in the lowest part of the IBL, commonly referred to as the equilibrium sublayer. That equilibrium sublayer is relatively shallow (about 10% of the IBL depth) and, even though it grows with distance from the transition, it often takes some distance to reach the height of the first grid point in LES. Since surface heterogeneity is a common feature of land surfaces, it is of interest to test the performance of LES boundary conditions over heterogeneous surfaces.

In this paper, the performance of SG, shifted-SG, local-SG and MKP models are studied in an heterogeneous boundary layer flow. A wind tunnel flow over a rough-to-smooth surface transition is used for this purpose. The experimental set up is described in section 3.3. In section 3.4, the boundary condition formulations are tested by *a priori* comparison of the statistical properties of the modeled surface shear stress with those of the measured shear stress. Finally, a summary and conclusions are given in section 3.5.

3.2 Experimental set-up

A rough-to-smooth surface transition was placed in the boundary-layer wind tunnel at the Saint Anthony Falls Laboratory (SAFL) of the University of Minnesota with the goal of studying the performance of different surface boundary condition formulations for LES behind a rough-to-smooth surface transition. The boundary-layer wind tunnel has a test section fetch of roughly 15 m and a cross-section of 1.7 m \times 1.7 m. There is a contraction with a 6.6:1 area ratio upwind of the test section along with flow conditioning/turbulence control consisting of a coarse wire mesh and honeycomb flow-straightener. The tunnel is driven by a 200 horse-power fan and is operated as a closed return loop. The turbulence intensity, in the centre of the wind tunnel is approximately

0.25% for a 10 m s^{-1} freestream velocity. More details on the wind tunnel can be found in Carper and Porté-Agel [23].

Wind-tunnel flow velocity was measured using Pitot static tubes (mainly for calibration) and constant temperature anemometry (CTA). Two types of CTA were used: single-normal (SN) and x-wire probes. The probes are made with $5.0 \mu\text{m}$ tungsten wire and are connected to an A.A. Lab Systems AN-1003 10-channel CTA system. During the calibration and measurements the temperature fluctuations were kept within a $\pm 0.5^\circ\text{C}$ range to avoid bias errors due to thermal drift of the voltage signal.

The rough-to-smooth transition was created by placing 7 m of wire mesh on the wind-tunnel floor upstream of a smooth floor. The woven-wire mesh is considered a k-type roughness (see Jimenez [54]) and has an average height $k_0 = 3.0 \text{ mm}$ with an aerodynamic roughness length $z_{01} = 0.5 \text{ mm}$. The roughness length was obtained by fitting a logarithmic velocity profile to the measured average velocity in the surface layer (approx. lowest 15% of the boundary layer) over the homogeneous surface.

A turbulent boundary layer is developed upstream with the help of a tripping mechanism (80 mm picket fence) located at the exit of the wind-tunnel contraction where the test section begins. The turbulent boundary layer is allowed to grow in zero pressure gradient conditions by adjustment of the wind-tunnel ceiling. The upstream roughness induces a strong change in the momentum flux near the surface, maintaining a well-developed surface layer with constant shear stress and a logarithmic velocity profile. The experiments were conducted with a 10 m s^{-1} freestream flow velocity and a turbulent boundary-layer depth, defined as the height where velocity reached the 99% of its free stream value, of $\delta = 0.4 \text{ m}$ at the roughness transition location.

A SN hotwire (boundary-layer type) probe and a x-wire anemometer were used to simultaneously measure surface shear stress and wind velocity (streamwise and spanwise components) at different positions downwind of the transition ($x/\delta = 0.1, 0.15, 0.2, 0.25, 0.375, 0.5, 0.75, 1.0$ and 1.5) and various heights (for the crosswire) within the internal boundary layer. A schematic and photograph of the experimental set-up are shown

in Figure 3.1. The SN hotwire was placed in the viscous sublayer, directly over the smooth surface. Here, the sensor was calibrated against a Preston tube following the procedure by Patel [79]. This procedure is well established and has been used in previous experimental studies by Alfredsson et al. [4], Chew et al. [32] and Khoo et al. [57]. During data collection the two sensors' voltage signatures were sampled simultaneously at a rate of 20 kHz for a measurement period of 120 s.

A review of rough-wall boundary layers by Jimenez [54] and an experimental study by Castro et al. [24] suggest that the boundary layer behaves differently depending on the ratio of boundary-layer height to roughness height (δ/k_0), with a change in behaviour when $\delta/k_0 > 80$, which is typical for the ABL. Previous wind-tunnel experiments [5, 72, 31, 24] have provided valuable results but use δ/k_0 on the order of 20. These relatively low ratios of boundary-layer height to roughness element height are not typical for land surface transitions because the effect of their roughness elements reaches further into the wind-tunnel boundary layer than does the effect of rough terrain in the ABL. Thus, the roughness chosen in those wind-tunnel studies may not provide a large enough range of length scales to allow a true equilibrium surface layer to develop. The set-up used in this study maintains $\delta/k_0 = 133$ to ensure that inner and outer scales of the boundary layer, and hence its structure, are well developed.

The zero pressure gradient boundary layer developed upstream of the transition had a Reynolds number based on the surface shear stress of $Re_\tau = u_*\delta/\nu \approx 1.5 \times 10^4$, a boundary-layer thickness of $\delta = 0.4$ m, a friction velocity of $u_{*1} = 0.55$ m s⁻¹ and a freestream velocity $U_1 = 10$ m s⁻¹. In this condition, the boundary layer upwind of the transition is in the fully rough regime [54]. The smooth surface consists of the finished wooden floor of the tunnel with a window of glass that lies flush and sealed with the floor. A boundary layer forming over the homogeneous smooth floor has approximately the same height as the boundary layer over the rough surface but with a friction velocity $u_{*2} = 0.32$ m s⁻¹ and aerodynamic roughness length $z_{02} = 0.006$ mm. Although z_{02} is a function of the friction velocity and kinematic viscosity for

aerodynamically smooth surfaces, here for simplicity it was assumed to be constant because the maximum difference in the estimation of the surface shear stress downwind of the transition was found to be about 2%.

Calibrations of the SN and crosswire anemometers were performed at the beginning of the experiment run. The crosswire was calibrated in the freestream region against a Pitot-static probe, at seven angles for each of seven velocities. A cubic-spline table calibration method was then used to determine the two instantaneous velocity components from the two instantaneous voltage signatures. For more details on the crosswire calibration see Bruun [18]. Calibration of the single hotwire against a Preston tube [79] was carried out using ten different velocities. The single hotwire and Preston tube were placed over a smooth flat plate in the freestream region to avoid any disturbance.

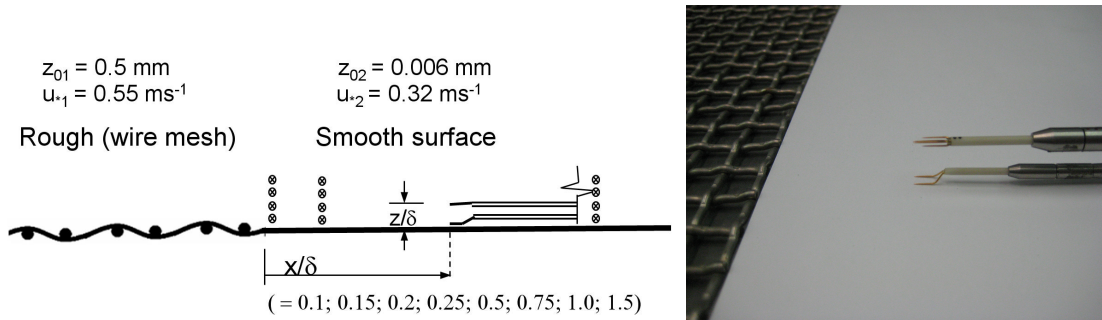


Figure 3.1: Schematic of the rough-to-smooth transition and measurement locations (top) and photograph of the single hotwire and crosswire probes placed downwind of the surface transition (bottom).

3.3 Surface Shear Stress Model Analysis

In this section, the filtered surface shear stress obtained from the single hotwire (boundary-layer type) sensor, hereon referred to as the measured surface shear stress, is compared to the 'modeled' surface shear stress obtained from the filtered velocity measurements

using the models detailed in section 1. Taylor's hypothesis, with a local velocity as a convection velocity, was used to filter the signals.

As in LES, the size of the filter (Δ_F) was chosen to be slightly larger than the height of the first grid point (typically $\Delta z/2$, where Δz is the vertical grid spacing). Specifically, one-dimensional box filters of lengths $\Delta_F = \Delta z$ and $2\Delta z$ were applied to obtain the filtered signatures of velocity and surface shear stress. Negligible differences were found when applying other types of filters (e.g. spectral and Gaussian). The box filter function is defined as

$$G_\Delta = \begin{cases} \frac{1}{\Delta}, & \text{if } |x| \leq \frac{\Delta}{2} \\ 0, & \text{otherwise,} \end{cases} \quad (3.9)$$

with G_Δ being a homogeneous filter function. With the box filter, $\tilde{u}(x)$ is the average of $u(x')$ in the interval $x' \in (x - \frac{1}{2}\Delta, x + \frac{1}{2}\Delta)$, where Δ represents the length of the filter.

Figure 3.2 shows a representative application of the box filtering function for the measured velocity (streamwise component) and surface shear stress at location $x/\delta=0.75$ and $z/\delta = 1.35/40$ after the transition. From this figure it is possible to notice the remarkable differences in the statistical properties of the two signals.

A representative comparison of the modeled shear stress (Equations 3.3, 3.4, 3.7 and 3.8) with its measured counterpart is shown in Figure 3.3 for a particular location downwind of the transition ($x/\delta = 0.75$ and $z/\delta = 1.35/40$). Specifically, Figure 3.3(a) shows the comparison between measured and modeled surface shear stress using the SG model (Equation 3.3). Similarly, Figure 3.3(b) shows the comparison using the shifted-SG model (Equation 3.4), Figure 3.3(c) shows the application of the local-SG model (Equation 3.7) and Figure 3.3(d) shows the case of MKP model (Equation 3.8). Both SG and its modified version, the shifted-SG model, clearly underestimate the level of fluctuations of the shear stress leading to an important departure of its statistical properties. In contrast, the MKP model is able to capture the level of fluctuations. Even though none of these models is able to reproduce the probability density function (pdf) of the normalized measured surface shear stress (see Figure 6.12 for $x/\delta = 0.5$ and

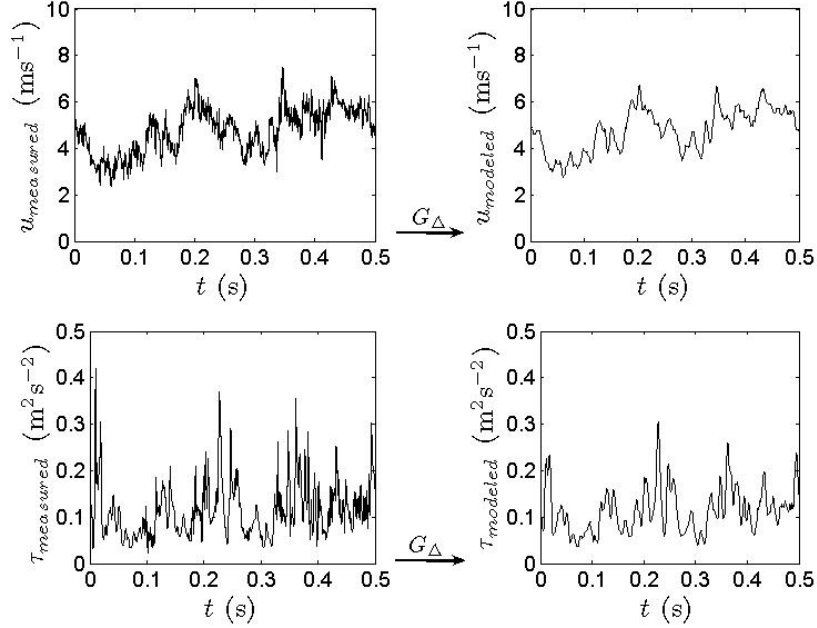


Figure 3.2: Representative box filtering application for the measured velocity and surface shear stress after transition at locations $x/\delta = 0.75$ and $z/\delta = 1.35/40$

$z/\delta = 1.35/40$), the local-SG model yields a pdf with a level of kurtosis that is closest to that of the measurements.

It is important to remark that all models under study require the specification of the mean value of the local shear stress. As mentioned before, common practice is to apply the log-law in a local sense (as indicated in Equation 3.2). A recent study of Chamorro and Porté-Agel [25] has shown that the direct application of the log-law (Monin-Obukhov similarity theory) for prediction of surface shear stress downwind of transitions can lead to large errors. In rigor, similarity theory is strictly valid only when applied over homogeneous surfaces and considering averages quantities. Chamorro and Porté-Agel [25] showed that, downwind a rough-to-smooth transition, the log-law underestimates the average surface shear stress. Moreover, that underestimation shows

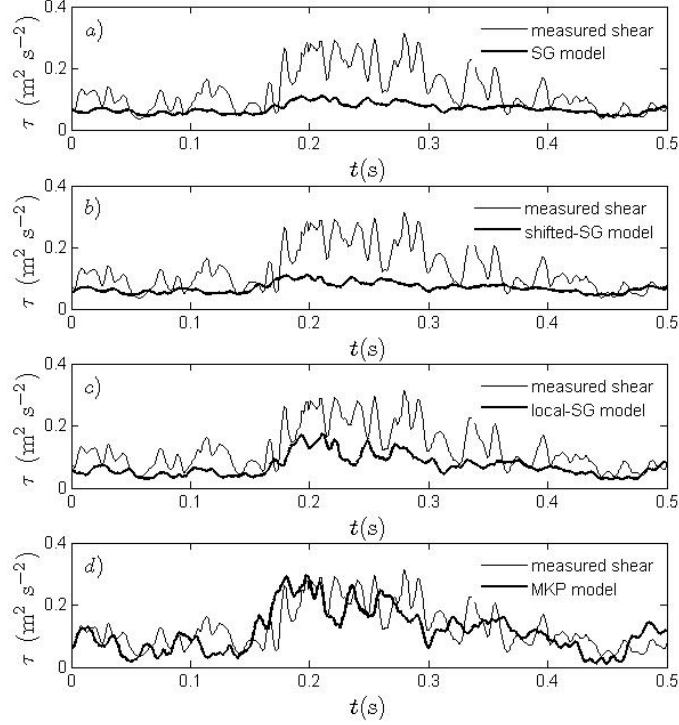


Figure 3.3: Representative comparison of modeled and measured surface shear stress at $z/\delta = 1.35/40$ and $x/\delta = 0.75$. (a) SG model; (b) shifted-SG model; (c) local-SG model and (d) MKP model.

a strong dependence with the height at which the model is applied (see Figure 3.5).

To improve the estimation of the mean shear stress at the surface as well as the mean velocity in the internal boundary layer, Chamorro and Porté-Agel [25] proposed a simple new model for the mean values of the local surface shear and velocity downwind of the transition. In particular, the mean velocity is estimated as a weighted average between two limiting logarithmic profiles: the first log law, which is recovered above the internal boundary layer depth, corresponds to the upwind velocity profile; the other log law is adjusted to the downwind aerodynamic roughness and local surface shear stress,

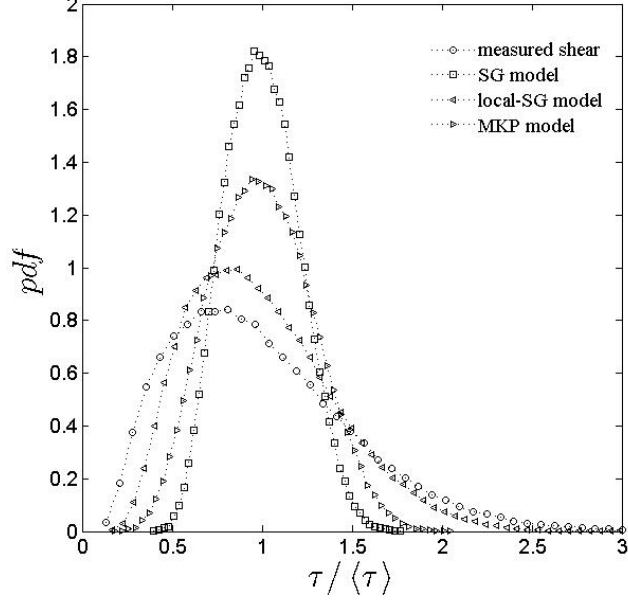


Figure 3.4: P.d.f. comparison between measured and modeled non-dimensional kinematic shear stress at $x/\delta = 0.5$ and $z/\delta = 1.35/40$

and it is recovered near the surface, in the equilibrium sublayer. The model (hereon referred to as ChPA) states:

$$U \approx \frac{u_{*2}}{k} \ln\left(\frac{z}{z_{02}}\right) + \lambda \left(\frac{u_{*1}}{k} \ln\left(\frac{z}{z_{01}}\right) - \frac{u_{*2}}{k} \ln\left(\frac{z}{z_{02}}\right) \right), \quad (3.10)$$

which can also be written as

$$U \approx (1 - \lambda) \frac{u_{*2}}{k} \ln\left(\frac{z}{z_{02}}\right) + \lambda \frac{u_{*1}}{k} \ln\left(\frac{z}{z_{01}}\right), \quad (3.11)$$

where u_{*1} is the upwind friction velocity, u_{*2} is its local counterpart, z_{01} and z_{02} are the aerodynamic roughness lengths upwind and downwind of the surface transition, respectively. The weighting parameter λ is defined as

$$\lambda = \ln(z/z_{01})/\ln(\delta_i/z_{01}). \quad (3.12)$$

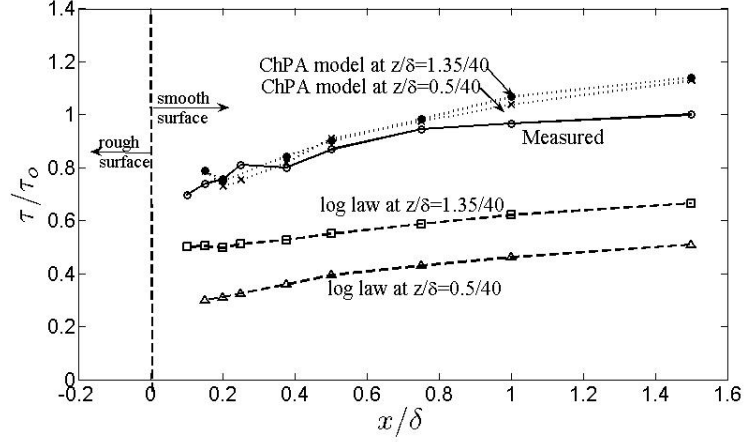


Figure 3.5: Measured and modeled surface shear stress obtained with log-law model and ChPA model using velocity measurements at two different heights. Downwind distance and height are normalized using the boundary layer depth $\delta = 0.4$ m. Surface shear stress is normalized with its downwind equilibrium value (τ_o)

Here δ_i is the internal boundary layer depth at location x . Figure 3.5 shows a comparison between measured and modeled average surface shear stress, considering both the log-law model and the ChPA model, for the same set-up as in this study. Here, the ChPA model is used in the MKP model for estimating the average shear stress.

To account for the statistical significance of the differences between the models and measurements, correlations and power spectra were calculated at different locations downwind of the transition. The correlation function between the modeled, τ_m , and measured, τ , surface shear stress signatures is defined as:

$$R_{\tau, \tau_m}(T) = \frac{\langle \tau'(t) \tau_m'(t - T) \rangle}{(\langle \tau'^2 \rangle \langle \tau_m'^2 \rangle)^{1/2}}, \quad (3.13)$$

where T is the time delay between the two signals, which are non-dimensionalized by their r.m.s. values, and primes indicate fluctuations with respect to their long time averages.

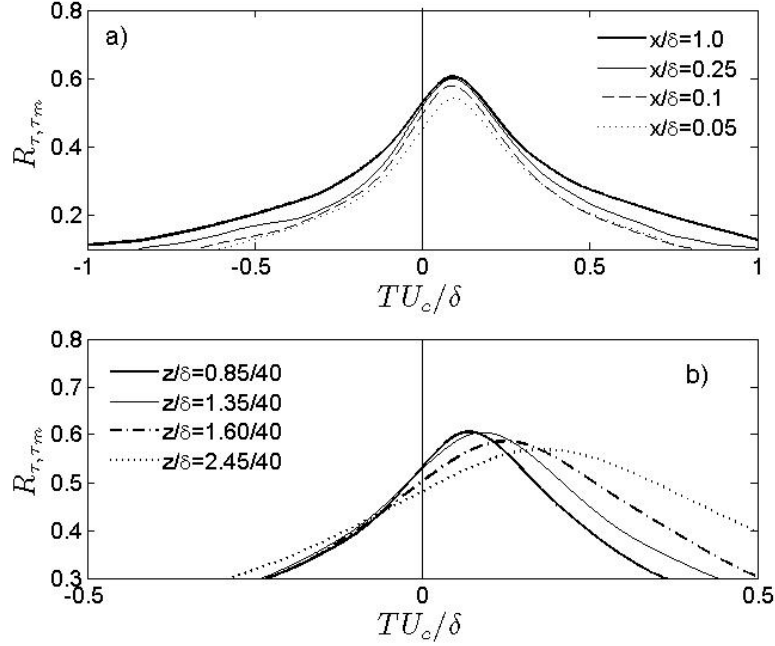


Figure 3.6: Correlation function between measured and modeled surface shear stress using the SG model. (a) $z/\delta = 1.35/40$; (b) $x/\delta = 1.0$

Figures 3.6 and 3.7 show the correlation function between the measured and modeled surface shear stress using the SG and local-SG models at different locations. In particular, Figure 3.6(a) shows the correlation at different downwind positions ($x/\delta = 0.05, 0.1, 0.25, 0.5$ and 1.0) for a constant height ($z/\delta = 1.35/40$) and Figure 3.6(b) shows the correlation at different heights ($z/\delta = 0.85/40, 1.35/40$ and $1.60/40$) for a particular location downwind of the transition ($x/\delta = 1.0$). Note that the correlation coefficient between measured and modeled surface shear stress using the SG model (Equation 3.3) is found at zero non-dimensional lag ($TU_c/\delta = 0$) in Fig. 3.6. The fact that the maximum of the correlation function is associated with some lag between the two signals justifies the use of a lag in the formulation of the shifted-SG and MKP models. It is found that the lag to the maximum correlation is very close to the lag values used in

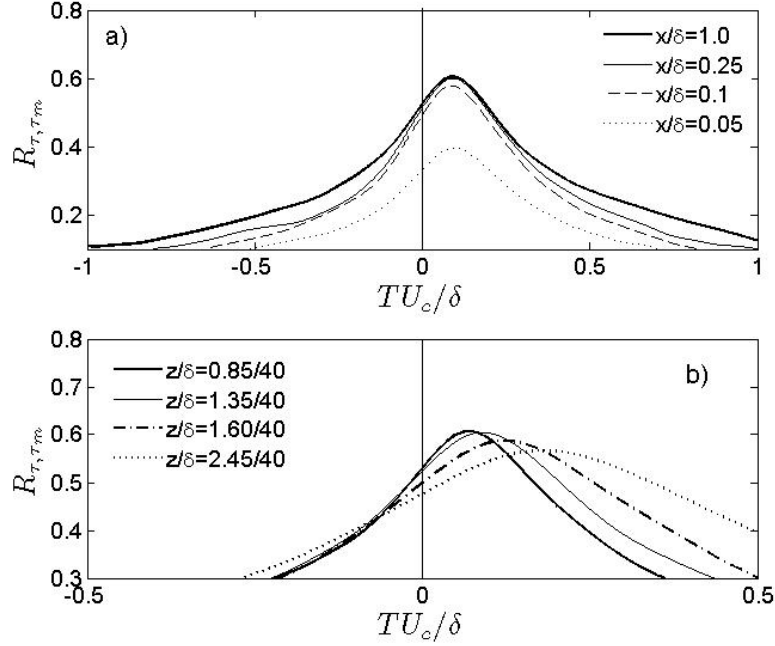


Figure 3.7: Correlation function between modeled and measured surface shear stress using the local-SG model. (a) $z/\delta = 1.35/40$; (b) $x/\delta = 1.0$

these model formulations.

Figure 3.7 shows the case of the local-SG model for the same locations of Figure 3.6. From Figures 3.6 and 3.7 it is also inferred that the peak of correlation decreases with increasing sensor height. The maximum correlation also decreases with decreasing distance from the transition. It is also found that the lag associated to the maximum correlation increases with sensor height (Figures 3.6(b) and 3.7(b)). This observation agrees with the idea that near-surface coherent flow structures are inclined with respect to the surface [82]. It is also consistent with the results of Brown and Thomas [17], Rajagopalan and Antonia [84] and Venugopal et al. [101] who studied single-point surface shear stress and velocity for homogeneous boundary layer flows. It is noted from Figures 3.6(a) and 3.7(a) that the peak of correlation keeps a relatively constant shift

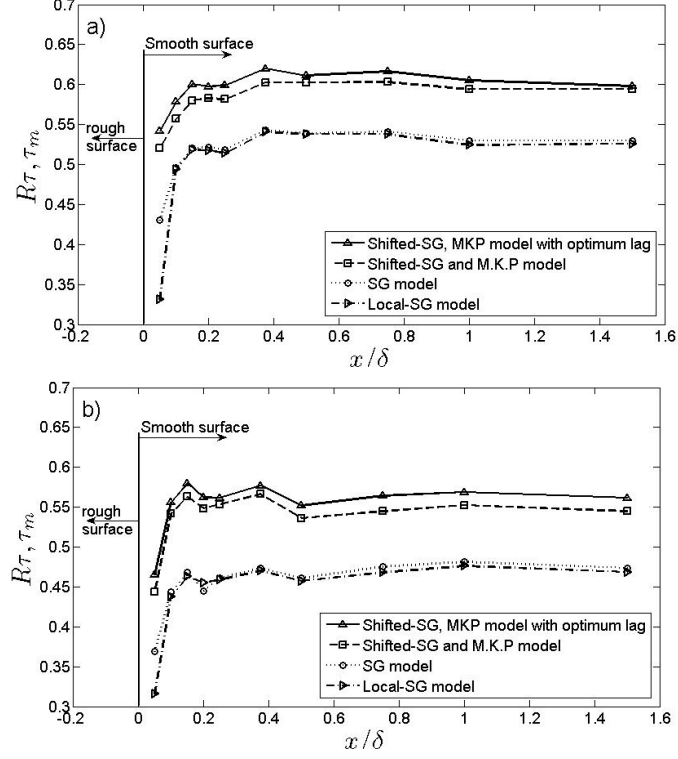


Figure 3.8: Correlation between measured and modeled surface shear stress behind the transition. (a) $z/\delta = 1.35/40$; (b) $z/\delta = 2.45/40$.

after the transition, indicating that the presence and angle of such coherent structures is not appreciably affected by the roughness transition. Overall, the correlation of SG and local-SG models does not show remarkable differences.

Figure 3.8 shows the modeled and measured shear stress correlation with distance for the SG, shifted-SG, local-SG and MKP models considering two different heights ($z/\delta = 1.35/40$ and $2.45/40$). By definition the shifted-SG gives the same correlation as the MKP model. From this figure it is possible to notice two aspects of particular interest: first, correlation reaches a plateau close to the (rough-to-smooth) transition. Second, the lag used for the shifted-SG and MKP models is very close to its optimum value at all the different locations downwind of the transition.

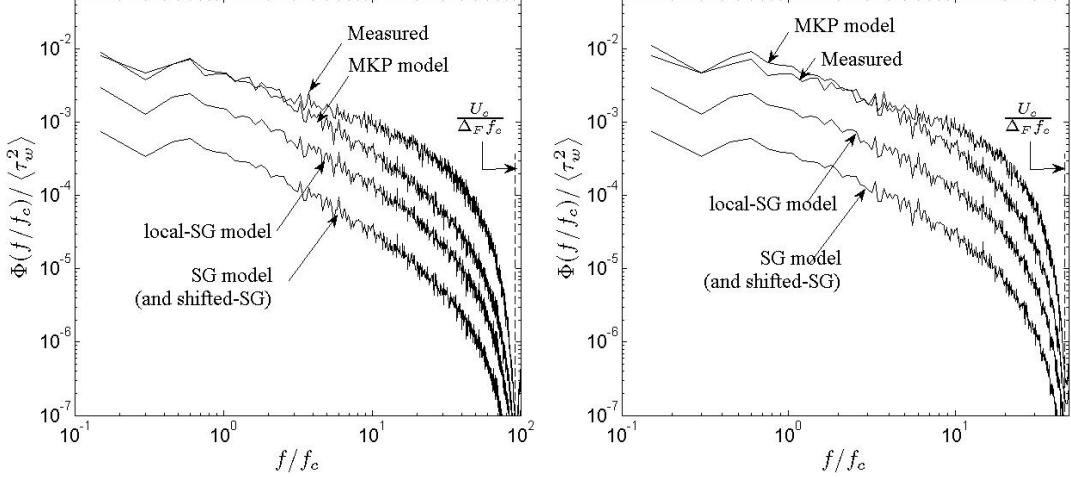


Figure 3.9: Normalized spectra of measured and modeled surface shear stress at $z/\delta = 1.35/40$ and $x/\delta = 1.0$ **using filter sizes of $\Delta_F = \Delta z$ (left) and $\Delta_F = 2\Delta z$ (right)**.

Power spectral density of the modeled and measured surface shear stress reveals relevant features of the signals. Figure 3.9 shows the power spectral density of the surface shear stress at location $x/\delta = 1.0$ and $z/\delta = 1.35/40$ downwind of the transition considering two filter sizes ($\Delta_F = \Delta z$ and $2\Delta z$), where:

$$\phi_\tau(f) = \lim_{T \rightarrow +\infty} \frac{1}{T} \{FT^*[\tau(t)] FT[\tau(t)]\}, \quad (3.14)$$

where f is the frequency, $FT[\]$ denotes the Fourier transform and $*$ indicates the complex conjugate. The spectra are normalized such that

$$\int_0^{+\infty} \phi_\tau(f) df = \langle \tau^2 \rangle \text{ or } \langle \tau_m^2 \rangle. \quad (3.15)$$

$\Phi(f/f_c)$ is defined as the power spectral density per non-dimensional frequency f/f_c , where $f_c = U_c/(2\pi\delta)$ and U_c is the convection velocity.

From Figure 3.9 it is clear that both SG and shifted-SG models underestimate the energy content of the measured shear at all scales of the flow by one order of magnitude.

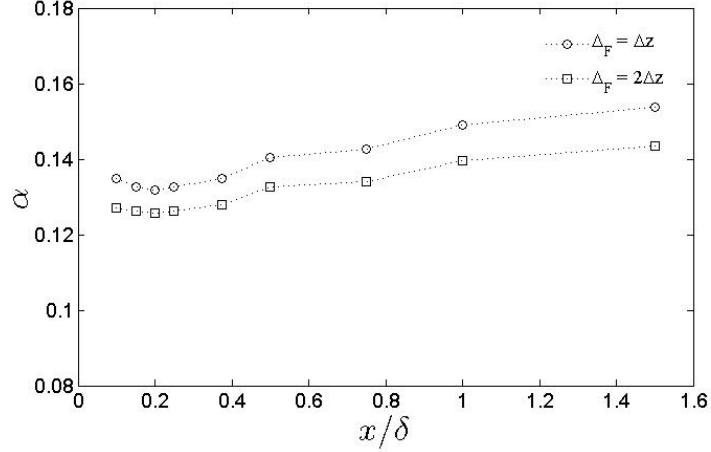


Figure 3.10: MKP model: α -coefficient behaviour after roughness transition

The local-SG model improves the prediction, but still underestimates its magnitude by about a factor of four. In contrast, MKP model is able to correctly estimate the energy content of the surface shear stress. This is due to the fact that, following Marusic et al. [63], the optimum value of the model coefficient α is chosen so that the variance of the modeled surface shear stress matches that of the measured stress. For example, a value of $\alpha = 0.14$ was adopted for the case presented in Figure 3.9.

Figure 3.10 shows the optimum value of α as a function of normalized downwind position (x/δ) for the two resolutions under consideration. We can see that α is slightly affected by surface heterogeneity and shows some departure from the previously reported value for homogeneous smooth surfaces (≈ 0.1). The coefficient exhibits also a weak dependence on the filter size.

Our results (Figure 3.10) show that the ratio between the variance and the average of the surface shear stress appears to be invariant with downwind distance from the transition, i.e., by expressing this ratio in a non-dimensional form:

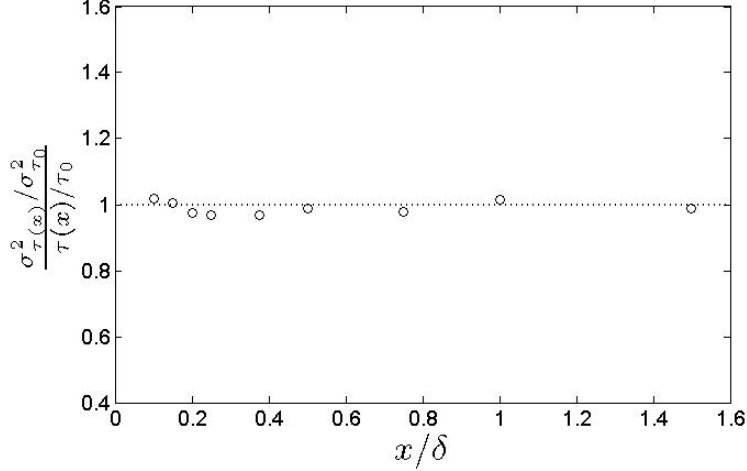


Figure 3.11: Non-dimensional ratio of measured surface shear stress and its variance with distance

$$\frac{\sigma_{\tau(x)}^2/\sigma_{\tau_0}^2}{\tau(x)/\tau_0} \approx 1, \quad (3.16)$$

where the subscript '0' indicates a reference location. In particular, a location where the flow is fully adjusted to the downwind surface can be used as a reference. From Equation 7.4, the variance of the surface shear stress can be estimated at any location downwind of the transition knowing its value at any particular point. This result could potentially be used to refine the formulation of models such as the MKP model (e.g., by accounting for the dependence of the coefficient α with distance) that aim at capturing not only the average local surface shear stress, but also its level of fluctuations (variance).

Higher order statistics such as skewness (see Figure 3.12) show, as expected, poor level of agreement between measured and modeled stresses for the SG, shifted-SG and MKP models. As indicated before, the linear-type relationship between velocity and surface shear stress used by these models precludes their ability to reproduce the skewness of the measured signal. The non-linear variant of the SG model, i.e., the local-SG model, is better able to capture a portion of the skewness of the surface shear stress

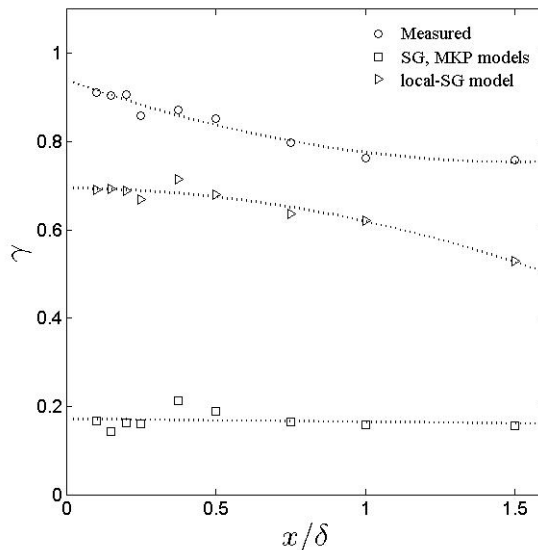


Figure 3.12: Third order moment (skewness) comparison between measured and modeled surface shear stress.

due to the non-linear nature of the model.

3.4 Summary

A wind-tunnel experiment was carried out to study the *a priori* performance of different surface boundary condition formulations downwind of a rough-to-smooth surface transition. Single hot-wire and x-wire anemometry were used to obtain simultaneous high-resolution measurements of surface shear stress and velocity at different locations from the transition. One-dimensional filtering, using Taylor's hypothesis, was used to obtain the measured filtered surface shear stress and filtered velocity. The measured filtered shear stress was then compared with the value of the surface shear stress modeled as a function of the filtered velocity using different boundary condition formulations.

Our results show substantial differences between the statistical properties (mean and higher order statistics) of the measured shear stress and the one modeled with

standard boundary conditions, which are based on surface layer similarity theory (the log-law under neutral stability corrections). Those models consistently underestimate the average surface shear stress downwind of the transition. This is due to the fact that throughout most of the internal boundary layer the flow is not fully adjusted to the underlying surface. Application of models that account for that effect on the log-law, such as the one recently introduced by Chamorro and Porté-Agel [25], can potentially correct the bias in the average shear stress prediction.

Comparison between spectra of the measured and modeled surface shear stress show that both SG and shifted-SG models underestimate the level of fluctuations of the modeled stress at all scales by roughly one order of magnitude. The local-SG model improves the prediction, but still underestimates its magnitude by about a factor of four. The MKP model yields the best prediction of the spectrum (and total variance) of the surface shear stress. It should be noted that the optimum value of the coefficient α in the MKP model is slightly larger ($\alpha \approx 0.12 - 0.16$) than the value of 0.1 reported by Marusic et al. [63] for homogeneous conditions. A weak dependence of α on distance from the transition and filter size was also observed. In addition, it is found that surface boundary condition formulations that assume a linear relationship between surface shear stress and velocity (e.g., SG, shifted-SG, and MKP models) cannot adequately capture the level of skewness of the PDF of the measured surface shear stress. The local-SG model yields a more realistic skewness due to the non-linear nature of the model.

The use of a shift in the velocity in boundary condition formulations (e.g., shifted-SG and MKP models) increases the correlation between the measured and modeled stresses. The optimum magnitude of the shift agrees with the results from previous studies over homogeneous surfaces [82], and appears to indicate that the characteristic inclination of the turbulent eddies is not noticeably affected by the presence of the transition. Our results also indicate that the ratio between the variance and average of the surface shear stress remain invariant with distance from the transition.

Overall, the results presented in this paper can be used to better understand the

limitations of existing boundary condition formulations, and to guide future efforts aiming to improve those models. Future research could also use the measurements presented here to pursue *a posteriori* testing of the models in large-eddy simulations of this heterogeneous boundary layer flow.

Chapter 4

A wind-tunnel investigation of wind-turbine wakes: Boundary-layer turbulence effects

Wind-tunnel experiments were performed to study turbulence in the wake of a model wind turbine placed in a boundary layer developed over rough and smooth surfaces. Hot-wire anemometry was used to characterize the cross-sectional distribution of mean velocity, turbulence intensity and kinematic shear stress at different locations downwind of the turbine for both surface roughness cases. Special emphasis was placed on the spatial distribution of the velocity deficit and the turbulence intensity, which are important factors affecting turbine power generation and fatigue loads in wind energy parks. Non-axisymmetric behaviour of the wake is observed over both roughness types in response to the non-uniform incoming boundary-layer flow and the effect of the surface. Nonetheless, the velocity deficit with respect to the incoming velocity profile is nearly axisymmetric, except near the ground in the far wake where the wake interacts with the surface. It is found that the wind turbine induces a large enhancement of turbulence levels (positive added turbulence intensity) in the upper part of the wake. This

is due to the effect of relatively large velocity fluctuations associated with helicoidal tip vortices near the wake edge, where the mean shear is strong. In the lower part of the wake, the mean shear and turbulence intensity are reduced with respect to the incoming flow. The non-axisymmetry of the turbulence intensity distribution of the wake is found to be stronger over the rough surface, where the incoming flow is less uniform at the turbine level. In the far wake the added turbulent intensity, its positive and negative contributions and its local maximum decay as a power law of downwind distance (with an exponent ranging from -0.3 to -0.5 for the rough surface, and with a wider variation for the smooth surface). Nevertheless, the effect of the turbine on the velocity defect and added turbulence intensity is not negligible even in the very far wake, at a distance of fifteen times the rotor diameter.

4.1 Introduction

Wakes of horizontal-axis wind turbines are complex turbulent flow structures with rotational motion induced by the turbine blades, longitudinal and radial pressure gradients, and spiral vortices originating from tip vortices shed by the blades. From a wind engineering perspective, there are two characteristics of wind turbine wakes that are of considerable practical interest: *(a)* the velocity deficit, which is related to the power loss from the wind turbine; and *(b)* the turbulence levels, which may affect flow-induced rotor loads on other turbines located downwind in a wind park. Understanding these effects is among the main reasons why turbine wakes have been the subject of intensive research, both experimentally and numerically, during the last few decades. A comprehensive review on wind-turbine-wake research is given by Vermeer et al. [102].

Detailed understanding of the turbulent properties of turbine wakes under different inflow and surface conditions is important to maximize the energy production and ensure the structural integrity of the wind turbines. In fact, the ability to predict the spatial distribution of the mean velocity deficit is essential to optimizing the design

(turbine siting) of wind farms. Understanding the spatial distribution of turbulence intensity generated inside turbine wakes is also important in determining fatigue loads on other wind turbines located downwind. In addition, a complete characterization of the turbulent properties in turbine wakes is desirable for validating and guiding the development of subgrid-scale parameterizations in numerical models of turbine wakes (e.g., large-eddy simulation (LES)).

The structure of wind turbines is known to be affected by the characteristics of the incoming flow. For example, Sheinman and Rosen [92] have shown that neglecting the effect of turbulence in the incoming flow can lead to an overestimation of turbine output by more than 10%. A wind-tunnel study performed by Medici and Alfredsson [66] has shown that the wake of a model turbine located in the free stream is substantially changed by the presence of turbulence in the flow. It is important to note that one expects even stronger differences in the structure and dynamics of the wake if the turbine is located inside (totally or partially) of the surface layer of a turbulent boundary layer. This layer is characterized by strong vertical gradients of velocity and turbulence intensity. The spatial variability in the incoming flow (not present in free stream flows), together with the anisotropy imposed by the presence of the ground, are expected to produce a non-axisymmetric wake structure. Among the factors that affect the incoming flow characteristics and, therefore, the wake structure are the aerodynamic surface roughness, the presence of surface inhomogeneities (e.g., surface roughness and temperature transitions), topography, and the effects of the wakes from other turbines located upwind in a wind park.

Turbulence intensity (I_u) plays a direct role on the mean force (\overline{F}) and bending moment (\overline{M}) acting on the turbine [13], and is commonly defined as the standard deviation of the wind velocity component in the average wind direction (σ_u) divided by the wind velocity at the turbine hub height (U_{hub}):

$$I_u = \frac{\sigma_u}{U_{hub}}. \quad (4.1)$$

In order to understand the effect of the turbulence intensity on the mean force \overline{F} , let us consider the instantaneous force acting on an element dA of the turbine:

$$dF = \frac{1}{2}\rho C_f dA (U + u)^2 = \frac{1}{2}\rho C_f dA (U^2 + 2Uu + u^2), \quad (4.2)$$

where ρ is the air density, C_f is the aerodynamic force coefficient, dA is the cross-sectional area of the element, U is the mean wind velocity, magnitude, and u is the turbulent velocity fluctuation. After time averaging, the mean force becomes:

$$\overline{dF} = \frac{1}{2}\rho C_f dA (U^2 + \sigma_u^2), \quad (4.3)$$

and if the flow is uniform, U and I_u are constant and the total force over the turbine is:

$$\overline{F} = \frac{1}{2}\rho \langle C_f \rangle AU^2 (1 + I_u^2), \quad (4.4)$$

where $\langle \rangle$ represents a spatial average over the turbine cross-sectional area.

Following a similar approach, the bending moment \overline{M} can be expressed as:

$$\overline{M} = \int_0^H \frac{1}{2}\rho C_f U^2 (1 + I_u^2) c(\xi) \xi d\xi \quad (4.5)$$

where $c(\xi)$ is the characteristic size of the turbine element at position ξ and H denotes the wind turbine height. Note that Equation 4.4 assumes a uniform distribution of U and I_u in the incoming flow. This is the case of free-stream flows. However, in the case of a wind turbine in a boundary-layer flow, characterized by non-uniform distributions of U and I_u in the surface layer, using that equation with a single value of U and I_u could lead to important errors.

As pointed out by Rosen and Sheinman [86], turbulence intensity is commonly used as a measure of the fatigue accumulation on various components of the turbine. In general, models for turbulence levels in turbine wakes are limited to single-point values or averaged magnitudes, thus not taking into account any cross-sectional variability. In particular, it is common practice to consider turbulence intensity at the hub of the wind turbine as representative for the whole rotor.

Several models have been proposed to estimate the so-called added turbulence intensity, I_+ , which is defined as a function of the ambient turbulent intensity, I_0 , and the turbulence intensity in the wake I_{wake} . In particular,

$$I_{wake}^2 = I_0^2 + I_+^2 \Rightarrow I_+ = \sqrt{I_{wake}^2 - I_0^2}. \quad (4.6)$$

Quarton and Ainslie [83] suggested the following empirical expression for the added turbulence (I_+) produced by the action of the rotor in a free-stream flow:

$$I_+ = 4.8C_T^{0.7}I_0^{0.68}(x/x_n)^{-0.57} \quad (4.7)$$

where C_T is the turbine thrust coefficient and x_n is the length of the near-wake region. This length is defined, according to [103], as:

$$x_n = \frac{\sqrt{0.214 + 0.144m}(1 - \sqrt{0.134 + 0.124m})}{(1 - \sqrt{0.214 + 0.144m})\sqrt{0.134 + 0.124m}} \frac{r_0}{(dr/dx)} \quad (4.8)$$

where $m = \frac{1}{\sqrt{1-C_T}}$, $r_0 = R\sqrt{\frac{m+1}{2}}$ and R is the rotor radius.

The wake growth rate, dr/dx , is given by the contributions of the ambient turbulence, $(dr/dx)_a$, the shear-generated turbulence, $(dr/dx)_m$, and the mechanical turbulence, $(dr/dx)_\lambda$, and defined as:

$$dr/dx = \sqrt{\left(\frac{dr}{dx}\right)_a^2 + \left(\frac{dr}{dx}\right)_m^2 + \left(\frac{dr}{dx}\right)_\lambda^2}, \quad (4.9)$$

where each contribution is estimated as $\left(\frac{dr}{dx}\right)_a^2 = 2.5I_0 + 0.005$, $\left(\frac{dr}{dx}\right)_m^2 = \frac{(1-m)\sqrt{1.49+m}}{9.76(1+m)}$ and $\left(\frac{dr}{dx}\right)_\lambda^2 = 0.012B\lambda$. B is the number of blades and λ is the tip speed ratio, which is defined as the ratio between the speed of the tip blade and the velocity of the incoming flow.

Crespo and Hernandez [35], based on both experimental and numerical approaches, proposed the following relation for the parameter ranges $5 < x/d < 15$, $0.07 < I_u < 0.014$ and $0.1 < a < 0.4$, where a is the induced velocity factor and d is the rotor diameter:

$$I_+ = 0.73a^{0.8325}I_0^{0.0325}(x/d)^{-0.32}. \quad (4.10)$$

Although they used the induced velocity factor a instead of the thrust coefficient C_T proposed by Quarton and Ainslie [83], these two are related. Specifically, according to the actuator disk theory, for $a < 0.5$, the relation between the induced velocity factor a and the thrust coefficient is $C_T = 4a(1 - a)$. Hassan [48], based on further work, proposed a similar expression for the added turbulence:

$$I_+ = 5.7C_T^{0.7}I_0^{0.68}(x/x_n)^{-0.96}, \quad (4.11)$$

and under a wind farm configuration, Frandsen and Thogersen [42] proposed a model for the added turbulence that takes into account the wind-farm layout. The model is based on the geostrophic drag law and takes into account the additional ‘surface roughness’ generated by the turbines:

$$I_+ = \frac{1}{2} \left(I_0 + \sqrt{I_0^2 + I_{++}^2} \right), \quad (4.12)$$

where

$$I_{++} = \frac{0.36}{1 + 0.2\sqrt{s_1s}/C_T}. \quad (4.13)$$

Here s_1 and s are the inter-turbine spacings (normalized by the rotor diameter) within a row and between rows, respectively. The Frandsen and Thogersen [42] model applies above the hub height, and has become the European standard. However, as pointed out by Burton et al. [19], to date there is no well-validated model for the prediction of turbulence intensity inside wind farms.

In this paper, the effect of boundary-layer flow on turbine wake characteristics is studied using detailed wind-tunnel measurements. Particular emphasis is placed on studying the distribution of streamwise mean wind velocity (and corresponding velocity deficit), turbulence intensity and kinematic shear stress in cross-sectional planes perpendicular to the axis of the wake at different downwind locations ($x/d = 3, 5, 10$ and 15 , where d is the turbine diameter). Experiments were carried out under neutral stability conditions over both rough and smooth surfaces in order to study the effect of roughness and the resulting velocity and turbulence fields on the wake characteristics.

First, the wind-tunnel experiments are presented in Section 4.3. In Section 4.4, the spatial distribution of flow statistics measured in the near and far regions of the turbine wake are analyzed for both the rough and smooth cases. Finally, a summary is given in Section 4.5.

4.2 Experimental set-up

A model 3-blade wind turbine was placed in the boundary-layer wind tunnel of the Saint Anthony Falls Laboratory at the University of Minnesota with the goal of studying turbulence characteristics of the turbine wake inside a fully developed neutrally-stratified boundary layer over both rough and smooth surfaces. The boundary-layer wind tunnel has a plan length of 37.5 m with a main test section fetch of 16 m. There is a contraction with a 6.6:1 area ratio upwind of the test section along with flow conditioning/turbulence control consisting of a coarse wire mesh and honeycomb flow-straightener. The tunnel is driven by a 200 h.p. fan and is operated as a closed return loop. The turbulence intensity in the centre (free stream) of the wind tunnel is approximately 1% for a 2.5 m s^{-1} freestream velocity. More details on the wind tunnel can be found in Carper and Porté-Agel [23].

Mean wind velocity in the tunnel free stream was measured using Pitot static tubes, mainly for calibration purposes. Constant temperature hot-wire anemometry (CTA) was used to obtain high-resolution measurements of the streamwise and vertical components of the wind velocity. The probe is made of $5.0 \mu\text{m}$ tungsten wires that are connected to an A.A. Lab Systems AN-1003 10-channel CTA system. During the calibration and measurements the temperature fluctuations were kept within a $\pm 0.2^\circ\text{C}$ range to avoid bias errors due to thermal drift of the voltage signal.

As shown in Figure 4.1, the rough surface was created by placing straight chains of approximately 5 mm height covering 10 m of the tunnel test section. The chains were aligned perpendicular to the flow direction and separated from each other by 0.20

m. This roughness set-up is ideal to incorporate thermal effects through heating or cooling of the test section floor. A similar roughness configuration was recently used by Ohya [75] to study stable boundary layers over rough surfaces. The smooth surface consists of a set of aluminum plates of 0.3 m length, each of which has a temperature control system to ensure the desired temperature level. Future experiments will use this heating/cooling system to study the effect of buoyancy (positive and negative) on the incoming boundary-layer wind and turbulence levels and, in turn, on the turbine wake characteristics.

A turbulent boundary layer was developed with the help of a tripping mechanism (40-mm picket fence) located at the exit of the wind-tunnel contraction, where the test section begins. The turbulent boundary layer was allowed to grow in zero pressure gradient conditions by adjustment of the wind-tunnel ceiling. The resulting boundary layer has a well-developed surface layer with constant shear stress and a logarithmic velocity profile.

The experiments were conducted at 2.5 m s^{-1} freestream flow velocity and a turbulent boundary-layer depth of $\delta \approx 0.4 \text{ m}$ at the turbine location. It is important to note that these flow conditions are also reasonable for future experiments that will aim at extending the analysis presented here to include the effects of thermal stratification on the wake structure. The wind turbine consists of a three-blade GWS/EP-6030x3 rotor attached to a small DC generator. The turbine angular velocity can be adjusted by changing the resistance of the generator. During the experiments, the tip speed ratio was approximately $\lambda = 4.4$ and $\lambda = 4.2$ for the smooth and rough cases, respectively.

The tip speed ratio was adjusted to match that of field-scale turbines (usually between 3.5 and 6). As shown in Figure 4.1, the bottom tip of the turbine was set to a height of 0.53 times the turbine radius, which is similar to that found in large-scale turbines ($\geq 2 \text{ MW}$). The turbine rotor was within the lowest half of the turbulent boundary layer. Despite the scaling issues associated with the difference in Reynolds number between the wind-tunnel flow and the atmospheric boundary-layer flow, our measurements

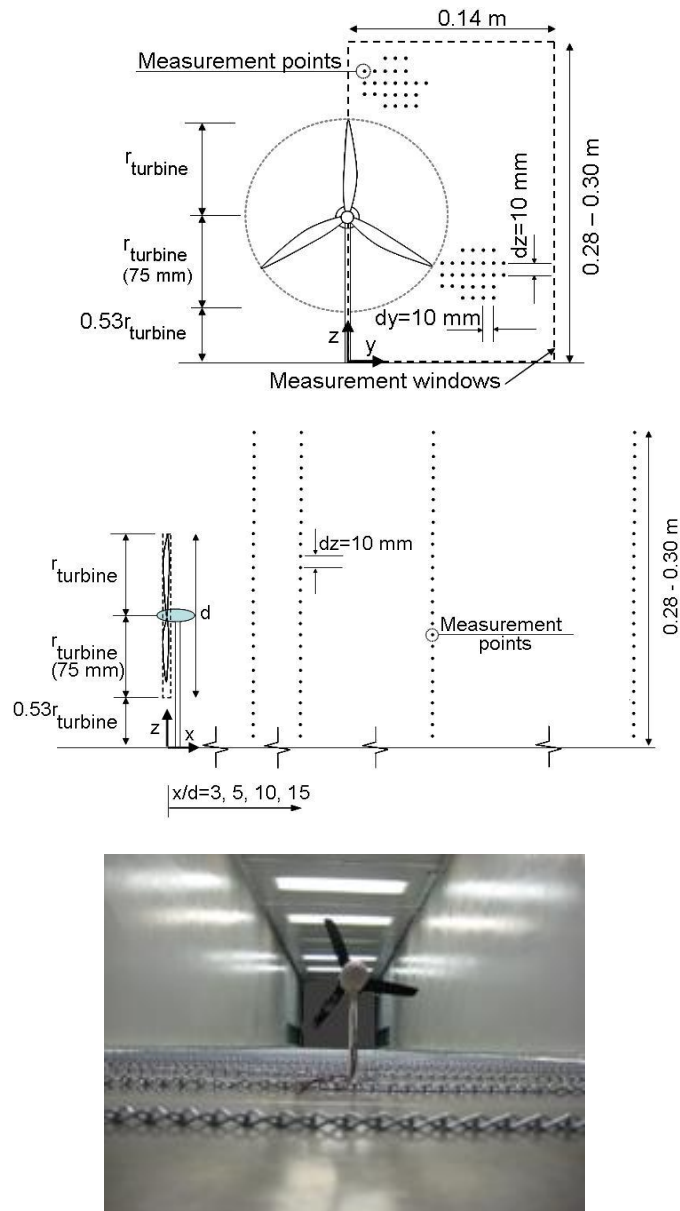


Figure 4.1: Schematic of the wind turbine (front and side views), coordinate system and measurement locations (top and middle), and photograph of the test section with the wind turbine (bottom).

provide detailed key information about the qualitative behaviour of turbine wakes in turbulent boundary-layer flows. It is also important to note that the high-resolution spatial and temporal measurements presented here can be used to systematically test the performance of numerical models (e.g., LES with different subgrid-scale models and wind turbine forces parameterizations) in the simulation of wind turbine wakes in turbulent boundary-layer flows.

As shown in Figure 4.1, the cross-wire anemometer was placed at different positions downwind of the turbine ($x/d = 3, 5, 10$ and 15). At each location detailed measurements were collected in a plane perpendicular to the mean flow direction. Specifically, measurements of streamwise and vertical velocity components were taken in a plane that spans from $z = 0$ to 0.28 m in the vertical direction, and from $y = 0$ to 0.14 m in the spanwise direction. On that plane, measurements were taken over a grid of points separated by $dy = dz = 10$ mm (spanwise and vertical direction). More than 1400 measurement locations were considered to characterize the turbine wake for each surface roughness case. At each location, the sensor voltage signature was sampled at a rate of 1 kHz for a measurement period ranging from 30 to 60 s. An ensemble average of two experiments was performed to reduce aleatory uncertainties.

The zero pressure gradient boundary layer, developed upstream of the transition, had a Reynolds number based on the friction velocity: $Re_\nu = u_*\delta/\nu \approx 0.4 \times 10^4$, a friction velocity of $u_{*r} = 0.16$ m s⁻¹ and $u_{*s} = 0.11$ m s⁻¹ for the rough and smooth surface, respectively. The aerodynamic surface roughness lengths were found to be $z_{0r} = 1.2$ mm and $z_{0s} = 0.05$ mm. These parameters (u_* and z_0) were obtained by fitting a logarithmic velocity profile to the measured average velocity in the surface layer (approximately lowest 15% of the boundary layer). Figure 7.4 shows the vertical profiles of the mean velocity, turbulence intensity and turbulent stress measured in the boundary layer over the rough and smooth surfaces .

Calibration of the crosswire anemometer was performed at the beginning of each

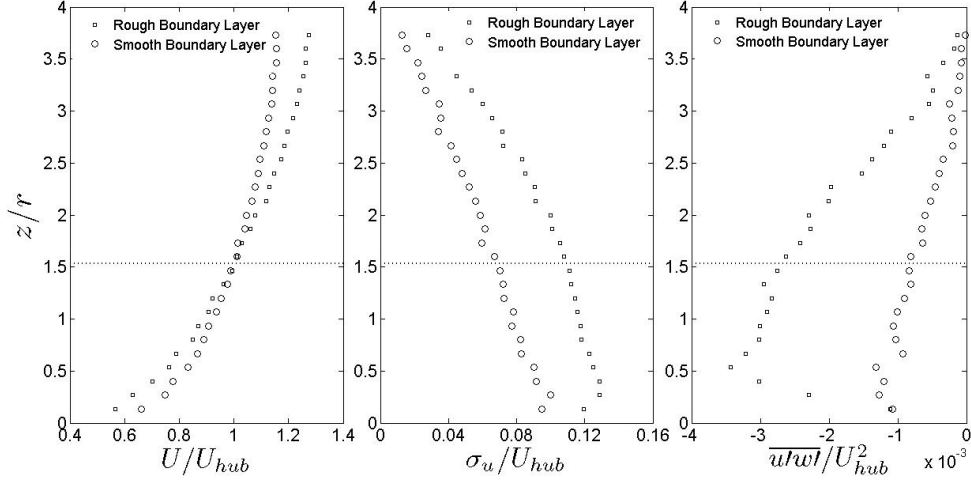


Figure 4.2: Background characteristics of the turbulent boundary layer over both rough and smooth surfaces: normalized mean velocity (left), turbulence intensity (middle) and kinematic shear stress (right). The horizontal lines represent the turbine axis. Height is normalized with the turbine radius r .

experimental run. Also a post-experiment calibration was carried out to check the validity of the calibration throughout the experiment. The anemometer was calibrated in the free-stream region against a Pitot-static probe, considering seven sensor inclination angles and seven wind velocities at each position. A cubic-spline table calibration method was then used to determine the two instantaneous velocity components from the two instantaneous voltage signatures. For more details on the calibration procedure, see Bruun [18].

4.3 Wake characteristics

4.3.1 Wake in a rough-wall boundary layer

A detailed cross-sectional characterization of the turbine wake over the rough surface is obtained from the high-resolution cross-wire anemometry measurements collected at different positions downwind of the turbine ($x/d = 3, 5, 10$ and 15 , see Figure 4.1).

Specifically, Figures 4.3, 4.5 and 4.8 show the cross-sectional distribution ($y - z$ plane) of the average streamwise velocity (U), turbulence intensity (I_u) and the kinematic shear stress ($\overline{u'w'}$). Our results show nearly symmetric behaviour of mean velocity and turbulence intensity around $y = 0$. For this reason, most of our measurements focused on one side ($y > 0$) of the wake. However, the kinematic shear stress showed roughly antisymmetric behaviour, with its axis of antisymmetry rotated approximately 45° . That behaviour is illustrated in Figure 4.9, which shows an entire cross-sectional distribution of the kinematic stress at $x/d = 5$.

Due to the effects of the non-uniform incoming boundary-layer velocity profile (logarithmic type) and the presence of the surface, the velocity distribution inside the turbine wake (Figure 4.3) does not show axisymmetric behaviour reported by previous studies in the case of free-stream flow (e.g., [36, 66]). The velocity reduction, modulated by the turbine, is superimposed on the logarithmic distribution of the incoming velocity, leading to a non-axisymmetric wake. However, as shown in Figure 4.4, the velocity deficit calculated with respect to the incoming wind velocity distribution, $\Delta U_x = U(x > 0, y, z) - U(x < 0, y, z)$, is approximately axisymmetric, with its axis of symmetry located slightly above the hub height. This is particularly relevant as it seems to point to the possibility of generalizing velocity-deficit formulations, developed for free-stream flow conditions, to non-uniform flows. As shown in Figure 4.4, the axisymmetry breaks down near the surface downwind of the position at which the wake has grown enough to reach the surface. In this case, that distance is close to $x/d = 5$.

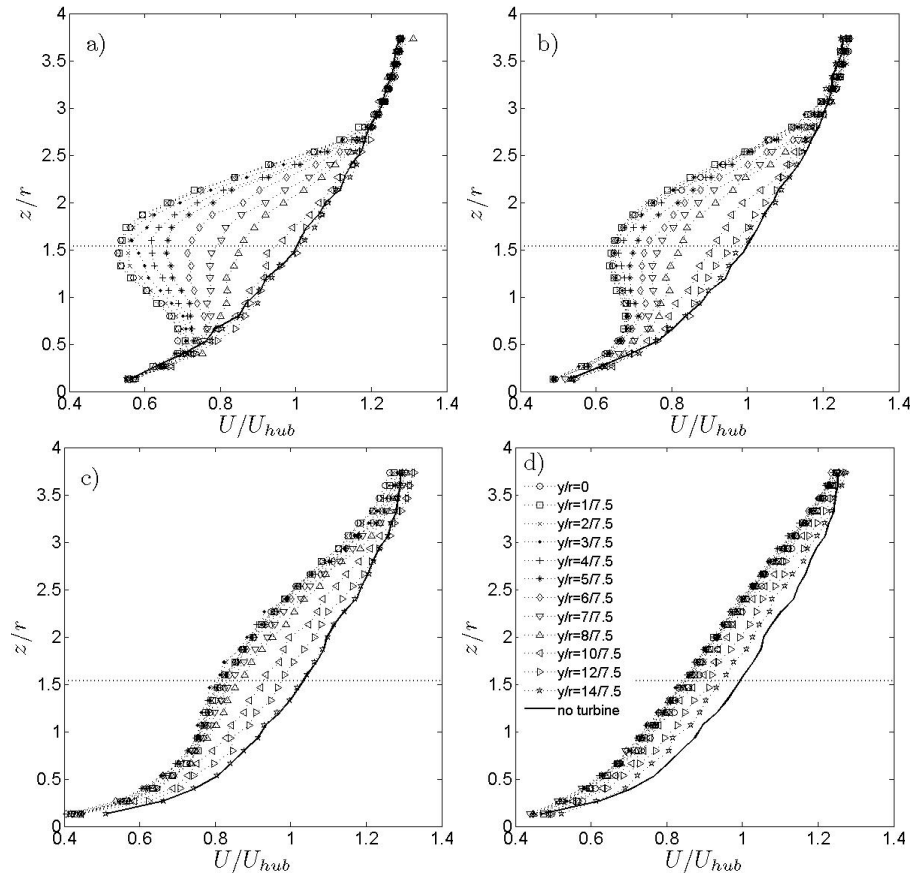


Figure 4.3: Non-dimensional cross-sectional distribution of the mean velocity at different downwind positions inside the wake over the rough surface. (a) $x/d = 3$; (b) $x/d = 5$; (c) $x/d = 10$; and (d) $x/d = 15$. The horizontal line represents the turbine axis.

The effect of the turbine is expected to lead to an enhancement of the turbulence intensity in the turbine wake, compared with the turbulence intensity of the incoming flow. As pointed out above, this can lead to increased fatigue loads in other wind turbines located downwind in a wind park. In the case of turbines located in free-stream flows, where the incoming flow is uniform, turbine wakes show an axisymmetric cross-sectional distribution of the turbulence intensity. In particular, one expects in the near wake ($x/d \leq 5$) to find a peak in the turbulence intensity around the tip of the turbine

wake, associated with the high turbulence levels produced by the helicoidal vortex that derive from turbine blade tip vortices [47]. Also in free-stream flow situations, both Ainslie [1] and Frandsen [40] associate the so-called far wake ($x/d \geq 5$) with a Gaussian distribution of the cross-sectional profiles of turbulence intensity.

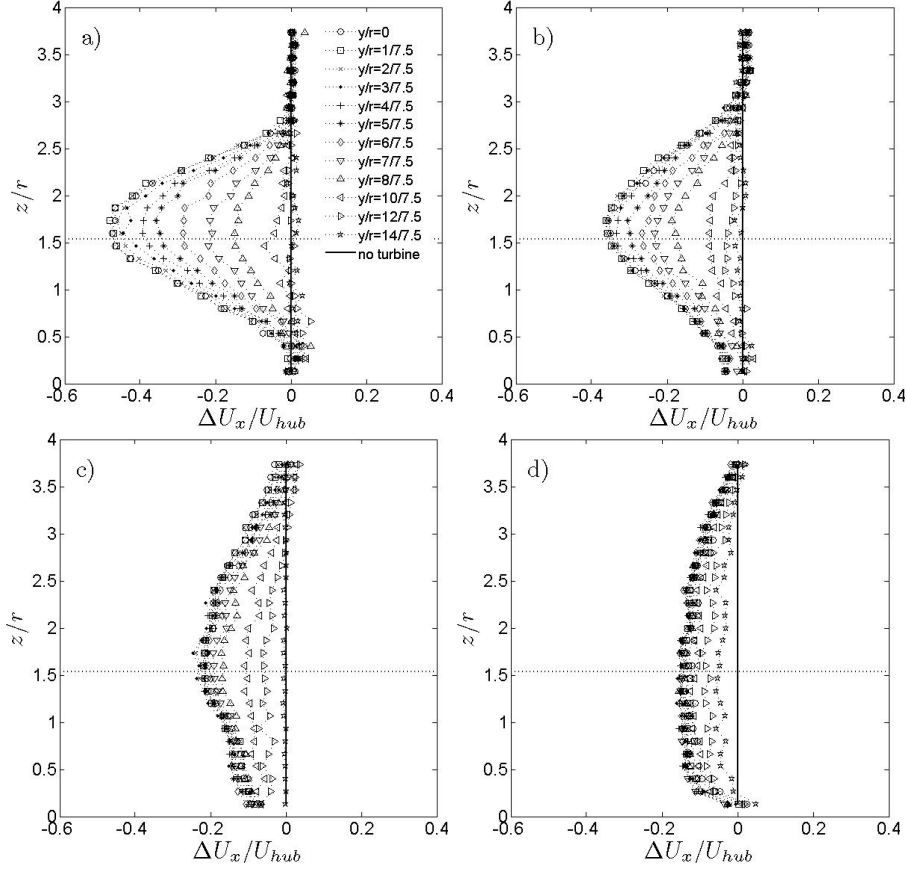


Figure 4.4: Non-dimensional cross-sectional distribution of the velocity deficit at different downwind positions inside the wake over the rough surface. (a) $x/d = 3$; (b) $x/d = 5$; (c) $x/d = 10$; and (d) $x/d = 15$. The horizontal line represents the turbine axis.

Having the wind turbine located in the boundary layer leads to a turbulence intensity distribution that is markedly non-axisymmetric and also non-Gaussian at all distances, as shown in Figure 4.5. This behaviour is associated with the non-uniformity of the

incoming flow and the presence of the surface. Near the upper edge of the wake, there is a strong enhancement of the turbulence intensity compared with the relatively low turbulence levels in the incoming flow.

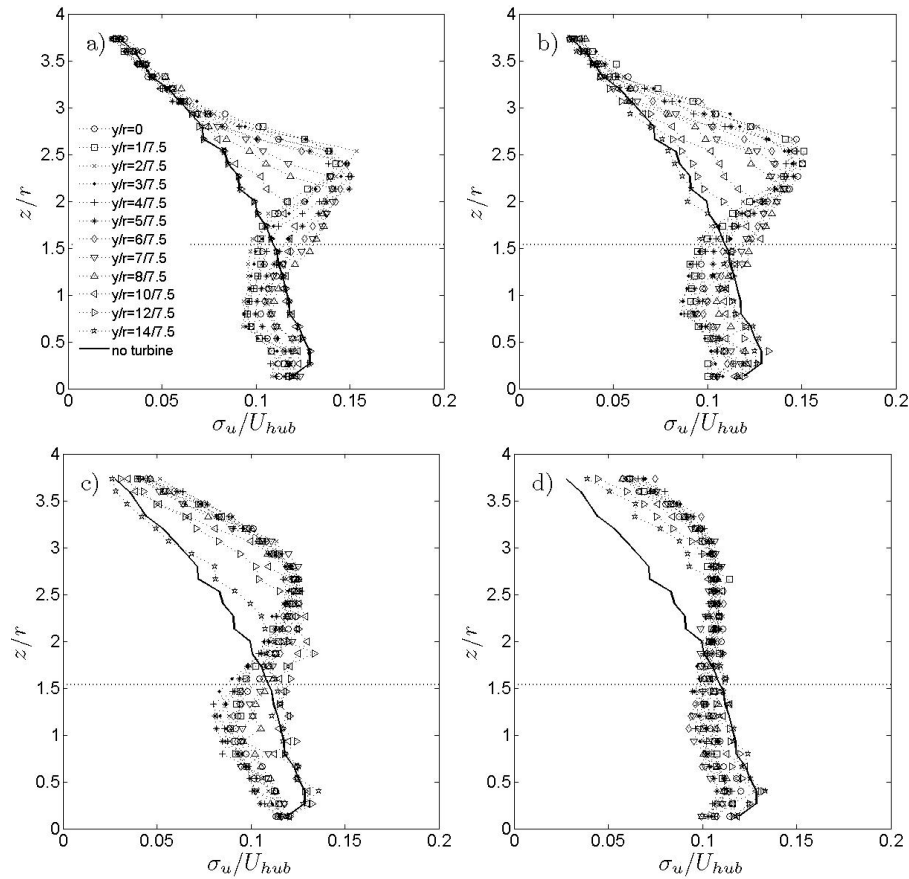


Figure 4.5: Non-dimensional cross-sectional distribution of turbulence intensity at different downwind positions inside the wake over the rough surface. (a) $x/d = 3$; (b) $x/d = 5$; (c) $x/d = 10$; and (d) $x/d = 15$. The horizontal line represents the turbine axis.

This is associated with the existence of a strong shear and the presence of helicoidal vortices at that location. However, the effect of the turbine leads to a reduction in the level of the turbulence intensity (compared to the relatively high turbulence levels

near the ground) below the hub height. This can be explained by considering that in that region the mean shear (Figure 4.3) and associated production of turbulence kinetic energy (not shown here) decrease with respect to the incoming flow.

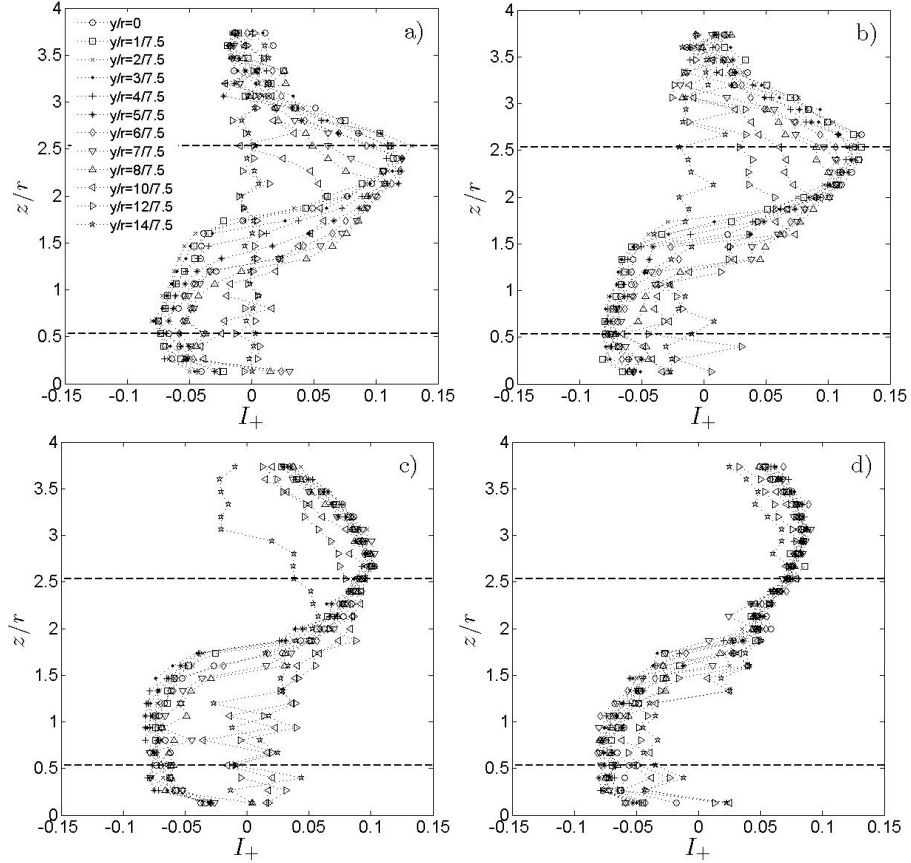


Figure 4.6: Non-dimensional cross-sectional distribution of the added turbulence intensity at different downwind positions inside the wake over the rough surface. (a) $x/d = 3$; (b) $x/d = 5$; (c) $x/d = 10$; and (d) $x/d = 15$. Horizontal lines represent the top tip and bottom tip levels.

Even though the turbulence enhancement effect decreases with distance, it remains evident even in the very far wake, at a distance $x/d = 15$, a location at which turbulence intensity shows roughly a uniform distribution through the entire wake. Here, turbulent

mixing has produced a uniform profile of turbulence intensity inside the wake.

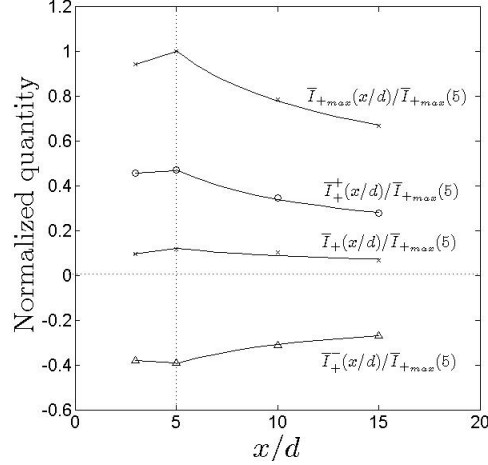


Figure 4.7: Normalized added turbulence quantities as a function of distance. Rough case.

A mean added turbulence intensity can be calculated at different downstream distances according to:

$$\bar{I}_{+} = \frac{1}{A} \int_A I_{+}(x, y, z) dA \quad (4.14)$$

where A is the cross-sectional surface of the wake and I_{+} is calculated according to Equation 4.6. The distribution of the mean added turbulence intensity is shown in Figure 4.6. Considering the non-axisymmetry of the turbulence intensity distribution shown in this figure, use of a single value to represent the wake-averaged added turbulence intensity, \bar{I}_{+} , is not sufficient to account for the spatial variability of high turbulence intensity on downwind turbine loads. In a simple first attempt to include these non-axisymmetry effects, we propose to differentiate between two markedly different contributions to \bar{I}_{+} : a positive change (increase) \bar{I}_{+}^{+} in the upper part of the wake, and a negative change (decrease) \bar{I}_{+}^{-} in the lower part of the wake, of turbulence intensity relative to the background incoming-flow turbulence intensity. As in Equation 4.14, these quantities are defined as:

$$\bar{I}_+^+ = \frac{1}{A_+} \int_{A_+} \sqrt{I_{wake}^2 - I_0^2} dA, \quad \text{for } I_{wake} > I_0, \quad (4.15)$$

$$\bar{I}_+^- = \frac{1}{A_-} \int_{A_-} \sqrt{I_0^2 - I_{wake}^2} dA, \quad \text{for } I_{wake} < I_0, \quad (4.16)$$

where A_+ and $A_- (= A - A_+)$ are the cross-sectional areas where the change of turbulence intensity is positive ($I_{wake} > I_0$) and negative ($I_{wake} < I_0$), respectively.

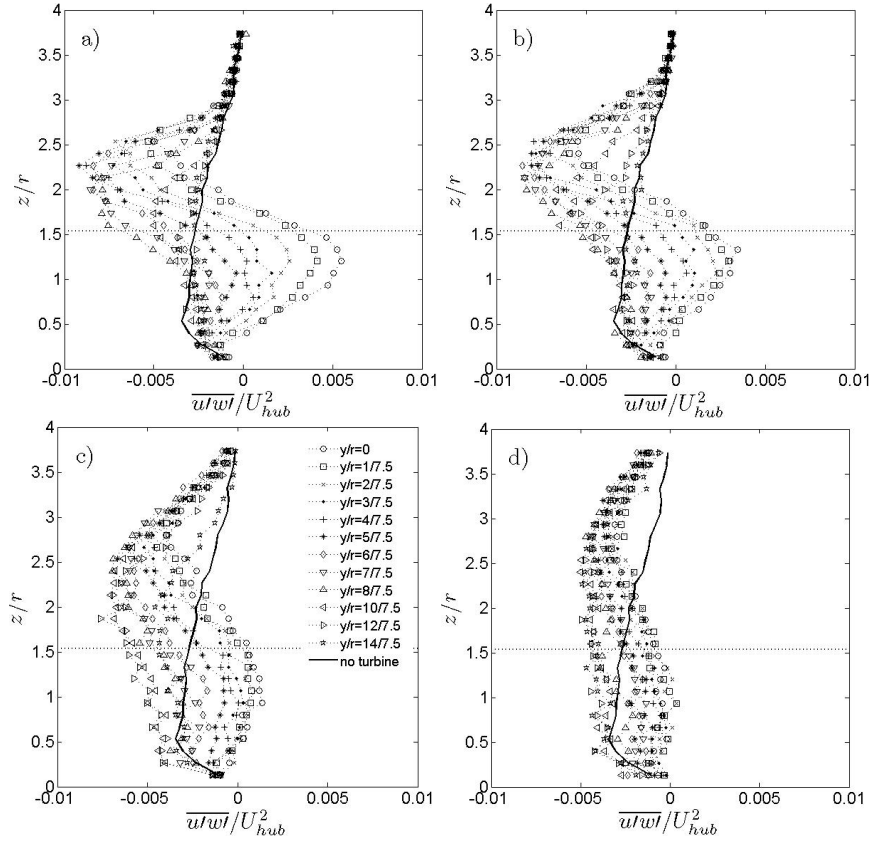
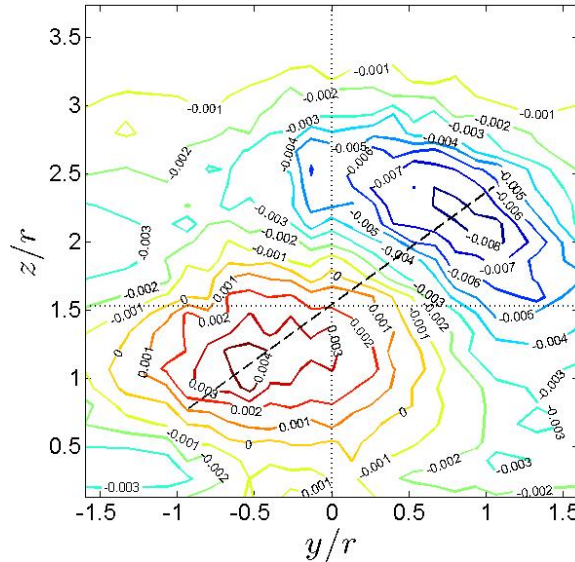


Figure 4.8: Non-dimensional cross-sectional kinematic shear stress distribution over a rough boundary layer. (a) $x/d = 3$; (b) $x/d = 5$; (c) $x/d = 10$; and (d) $x/d = 15$. The horizontal line represents the turbine axis.

Also, indicators of the turbulent intensity are its maximum value and the value

coincident with the hub level (often used as a reference).

Figure 4.7 shows the values of the average added turbulence intensity, \bar{I}_+ , its positive (\bar{I}_+^+) and negative (\bar{I}_+^-) contributions, and the maximum (I_{+max}) at different locations downwind of the turbine. The intensity is normalized with its maximum value at a distance of $x/d = 5$. By examining the rate of change of these quantities with distance, it is inferred that in the far wake region, $5 < x/d < 15$, $\bar{I}_+^+ \propto x^{-0.47}$, $\bar{I}_+^- \propto x^{-0.34}$, $\bar{I}_{+max} \propto x^{-0.36}$, and $\bar{I}_+ \propto x^{-0.46}$. In general these quantities decay as a power law of distance, with an exponent in the range $[-0.5, -0.3]$. This rate of decay is in good agreement with previously reported results (e.g., [83, 35]) for the case of the wake of a turbine located in a free-stream flow.



incoming velocity field. In the near-wake region, at distances $x/d \leq 5$, there is a region above the turbine hub with large negative stress, and a lower region with large positive stress. As the wake grows with downwind distance, the relative change in the kinematic stress becomes smaller and affects a larger cross-sectional area. Notice that, as with the case of the velocity defect and the added turbulence intensity, the change in kinematic stress with respect to the incoming flow remains not negligible even in the very far wake, at $x/d \approx 15$. In order to illustrate the lack of symmetry of the turbulent stress with respect to the $y = 0$ plane, Figure 4.9 presents the distribution of the stress in an entire cross-sectional plane at $x/d = 5$. This figure shows that, at that distance, the largest positive stress is located in the first quadrant (above the hub height and $y > 0$), while the largest negative stress is found in the third quadrant (below the hub height and $y < 0$).

The distribution of streamwise velocity skewness, presented in Figure 4.10, reveals that the effect of the turbine leads to a reduction in the magnitude of velocity skewness with respect to the incoming flow. In fact, skewness at different downwind locations inside the wake is slightly positive, which differs substantially from the negative skewness measured in the incoming flow away from the surface.

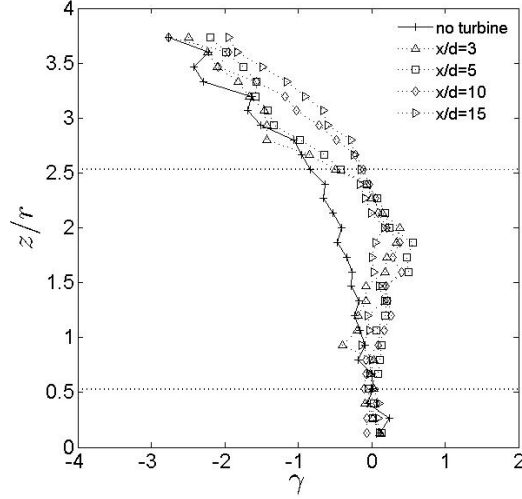


Figure 4.10: Skewness of the streamwise velocity component at $y = 0$ and different positions downwind ($x/d = 3, 5, 10, 15$) and upwind of the turbine. Rough case. Horizontal lines represent the top tip and bottom tip levels.

As pointed out by Carlin [21], skewness plays a role in power generation. In fact, mean turbine power can be written as:

$$\bar{P} = \frac{1}{2}\rho A \bar{U}^3 = \frac{1}{2}\rho A \bar{U}^3 K_e \quad (4.17)$$

where

$$K_e = \frac{1}{N \bar{U}^3} \sum_{i=1}^N U_i^3 \quad (4.18)$$

for a discrete number of wind velocity data points. By expanding \bar{U}^3 using Reynolds decomposition,

$$K_e = 1 + 3I_u^2 + \gamma I_u^3 \quad (4.19)$$

where γ is the skewness coefficient. According to Equation 4.19, the skewness of the incoming wind can reduce or increase the mean power generation, depending on the sign of the skewness coefficient. It is important to point out that the turbine removed the negative skewness of the incoming velocity field away from the surface. As a result,

velocity skewness in the wake will play a minor role (compared with velocity deficit and turbulence intensity) on the mean power from a turbine located in the wake of another turbine.

In order to better understand what range of scales contribute to the observed turbulence intensity changes induced by the wake, power spectra of the streamwise velocity are computed and shown in Figure 4.11 for different positions in the wake. It includes, for comparison, the spectra of the incoming wind velocity (Figure 4.11a). Comparison between spectra corresponding to the bottom-tip, hub-height and the top-tip levels at different downwind locations shows that the effect of the turbine on the turbulent intensities (enhancement at the top-tip level and reduction at the lower-tip level) are mostly associated with relatively large scales (frequencies lower than about 10 Hz). The inertial subrange is found to grow with downwind distance and it is characterized by a similar level of energy at any position inside the turbine wake. Note that very close to the wind turbine, at a distance $x/d = 1$, the velocity spectrum calculated at the top-tip level has a clear peak associated with the presence of tip vortices (Figure 4.11b). The peak occurs at a frequency of ≈ 60 Hz, which coincides with three times the frequency of rotation of the rotor, or the frequency of consecutive blades.

The peak is not observed at the bottom-tip level, where the turbulence levels of the incoming flow are relatively high. In the wake, at $x/d = 15$, the energy content is very similar at all scales and still substantially different from that in the incoming flow. This is consistent with the nearly uniform profile of turbulence intensity measured at that location and shown in Figure 4.5d.

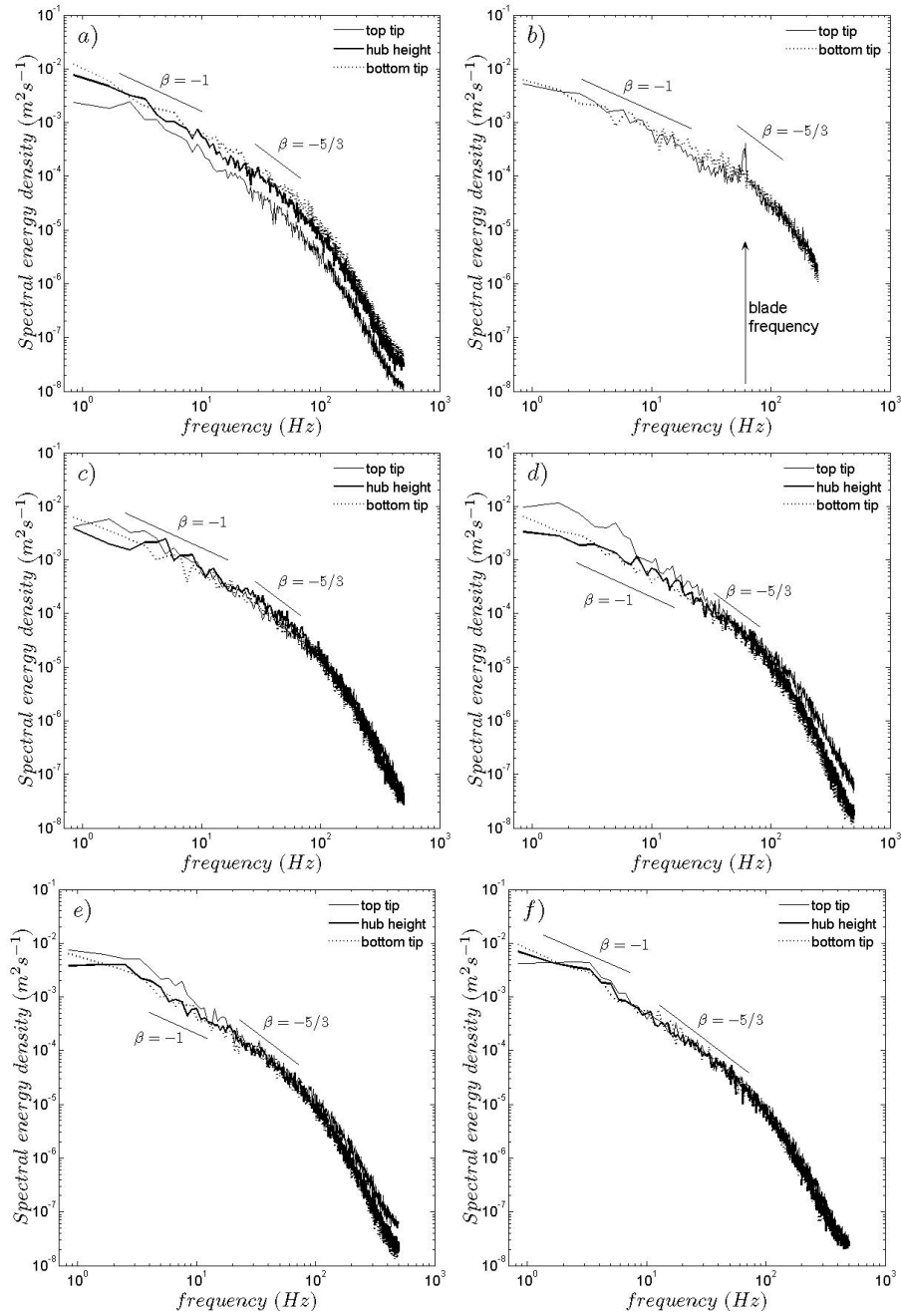


Figure 4.11: Power spectrum of the streamwise velocity at different heights (top-tip level, hub height and bottom-tip level) and different downwind positions in the center plane of the wake ($y = 0$). (a) without turbine; (b) $x/d = 1$; (c) $x/d = 3$; (d) $x/d = 5$; (e) $x/d = 10$ and (f) $x/d = 15$.

4.3.2 Wake in a smooth-wall boundary layer

In this section, turbulence measurements collected in the wake of a wind turbine located in a boundary layer over a smooth surface are presented. In particular, Figures 4.12 and 4.13 show the cross-sectional distributions of mean streamwise velocity deficit ($\Delta U_x = U(x > 0, y, z) - U(x < 0, y, z)$) and the added turbulence intensity (I_u) measured with the cross-wire anemometer at different locations downwind of the turbine ($x/d = 3, 5, 10$ and 15), similar to the rough case.

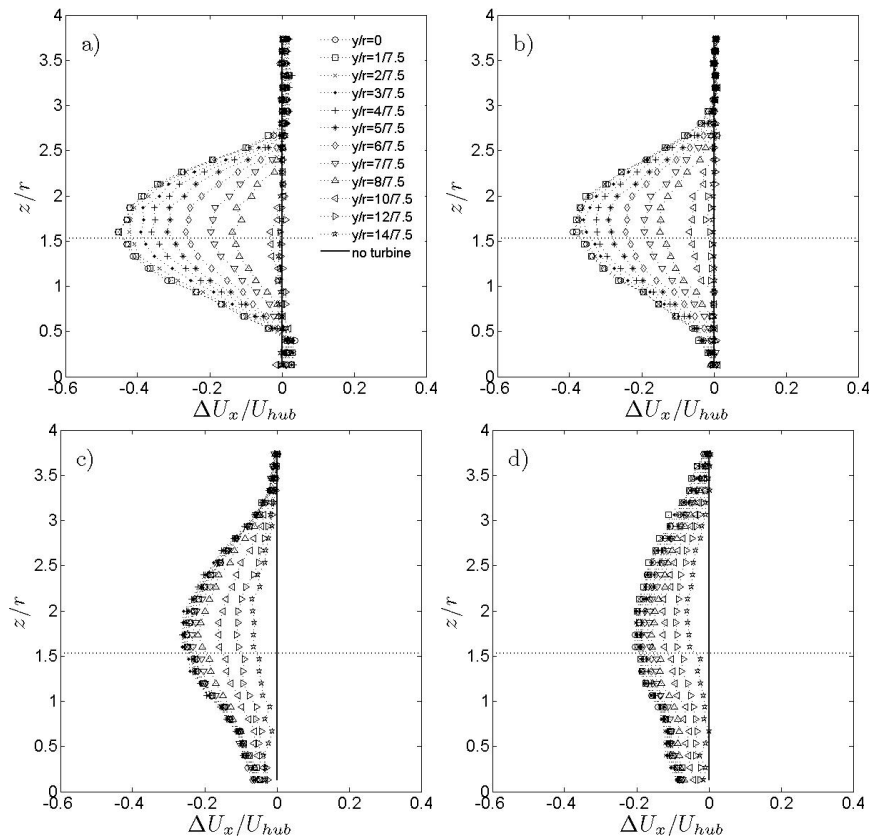


Figure 4.12: Non-dimensional cross-sectional distribution of the velocity deficit at different downwind positions inside the wake over the smooth surface. (a) $x/d = 3$; (b) $x/d = 5$; (c) $x/d = 10$; and (d) $x/d = 15$. The horizontal line represents the turbine axis.

Comparison of these figures with their counterparts for the rough case reveals an important effect of surface roughness on the degree of non-axisymmetry of the turbine wake and its evolution. The wake over the smooth surface shows a relatively smaller departure from axisymmetry compared with the rough surface case even when it has reached the surface. This can be explained considering that the incoming velocity field is more uniform compared with the rough case (see Figure 7.4). Since wakes are superimposed on the incoming velocity distribution, the more uniform the incoming flow at the turbine level, the smaller the departure from axisymmetry of the wake. In the limiting case of a uniform incoming flow (e.g., a turbine placed in a free-stream flow), the turbine wake is axisymmetric ([102, 66]).

The velocity deficit (ΔU_x), shown in Figure 4.12, reveals that the turbine wake touches the surface at a distance x/d within the range $[5, 10]$, which is longer than the rough case, where this distance is $x/d < 5$ (Figure 4.4). This observation shows clearly that the cross-sectional expansion of the wake is affected by the surface roughness. From Figure 4.4, it is possible to notice that the height of the axis of symmetry increases with distance. Overall, in the smooth surface case, the magnitude of the velocity deficit in the wake is larger than in the rough surface case. Also from Figure 4.12, it is noted that this velocity deficit decreases with downwind distance at a slower rate compared to the rough case.

Added turbulence intensity profiles in the turbine wake show important differences with respect to the rough case (Figures 4.13 and 4.6, for the smooth and rough cases, respectively). Even though in both cases the non-uniformity of the incoming flow leads to a non-axisymmetric distribution of the added turbulence intensity in the turbine wake, this non-axisymmetry is smaller over the smooth surface. This is obvious when considering the relative importance of the negative change of turbulence intensity, \bar{I}_+^- , as defined by Equation 4.16. In particular, the reduction of turbulence intensity in the lower part of the wake with respect to the incoming flow is relatively smaller over the smooth surface. In contrast to the rough case, at distances $x/d \approx 5$, \bar{I}_+^- is confined to

lower heights ($z/r \leq 1$) compared with the the rough case for which \bar{I}_+ extends up to a height of $z/r \approx 1.75$. Over the smooth surface, \bar{I}_+ grows up to $z/r \approx 1.5$ at larger distances.

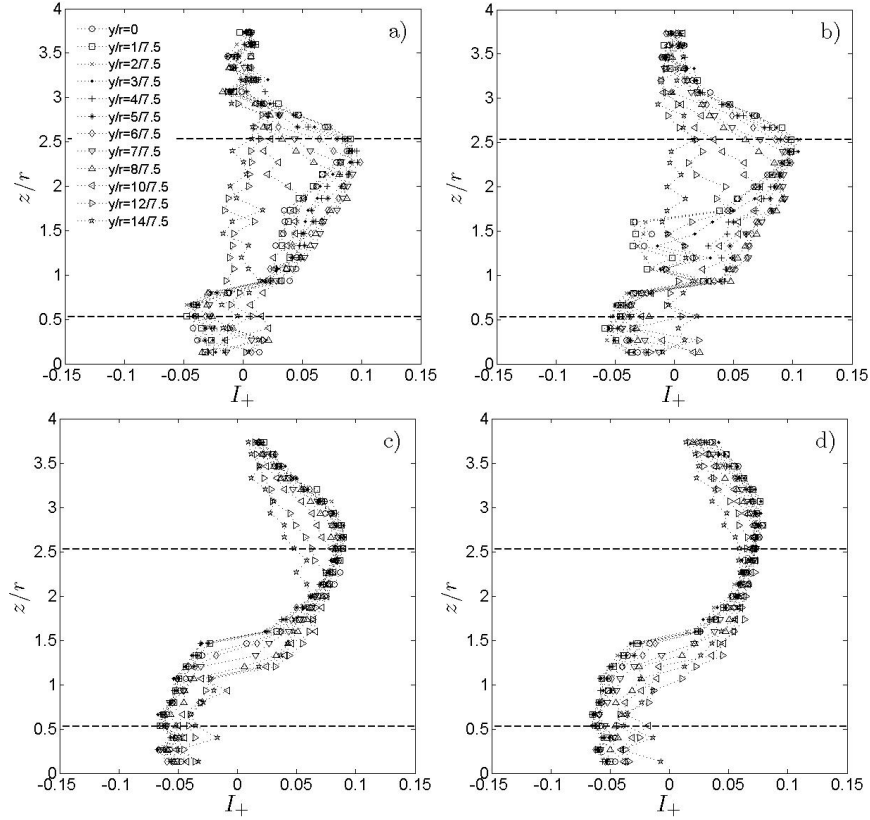


Figure 4.13: Non-dimensional cross-sectional distribution of the added turbulence intensity at different downwind positions inside the wake over the smooth surface. (a) $x/d = 3$; (b) $x/d = 5$; (c) $x/d = 10$; and (d) $x/d = 15$. Horizontal lines represent the top tip and bottom tip levels.

It was found (not shown here) that the average added turbulence intensity, \bar{I}_+ , its positive (\bar{I}_+^+) and negative (\bar{I}_+^-) contributions, and its maximum (I_{+max}) change with downwind distance as $\bar{I}_+ \propto x^{-0.7}$, $\bar{I}_+^+ \propto x^{-0.41}$, $\bar{I}_+^- \propto x^{-0.12}$ and $\bar{I}_{+max} \propto x^{-0.22}$.

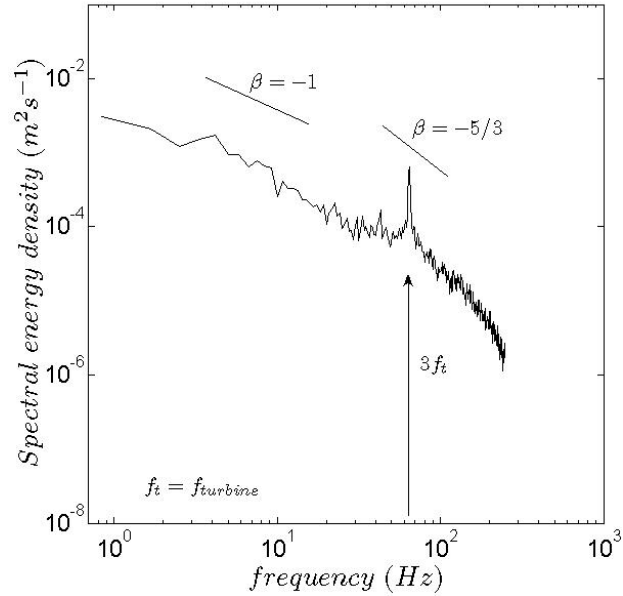


Figure 4.14: Power spectrum of streamwise velocity at the top tip and $x/d = 1$.

The qualitative distribution of the kinematic shear stress $\overline{u'w'}$ (result not shown here) is comparable with that over the rough surface (Figure 4.8). As in that case, the cross-sectional distribution of the stress is also antisymmetric, with the axis of symmetry rotated approximately 45° . However, it is important to remark that the magnitude of the kinematic stress is smaller than the one measured in the rough case, which highlights the importance of considering the incoming flow so as to understand the distribution of kinematic stresses and other turbulence quantities in turbine wakes.

Skewness and spectra of the streamwise wind velocity component calculated in the wake of the turbine over the smooth surface (not shown here) have the same qualitative behaviour as discussed in Section 3.1 for the rough case. Nevertheless, the signature of the tip vortices near the turbine ($x/d = 1$) and at the top-tip level is stronger in the smooth case due to the relatively lower background turbulence level in the incoming flow with respect to the rough case (Figure 4.14).

4.4 Summary

A wind-tunnel experiment was performed to study the effects of boundary-layer turbulence and surface roughness on the structure of the wake developed downwind of a model turbine. Hot-wire anemometry was used to obtain detailed measurements of wind velocity, turbulence intensity and kinematic stress over several cross-sections at different positions downwind of the turbine. Skewness coefficients and power spectra of the streamwise velocity were also calculated to obtain a better understanding of the turbulence inside the wake. The turbine was placed in a boundary layer developed over both rough and smooth surfaces under neutral conditions. Special emphasis was placed on quantifying the magnitude and spatial distribution of the velocity deficit and the enhancement of the turbulence intensity in the turbine wake with respect to the incoming boundary-layer flow. These quantities are important factors affecting turbine power output and fatigue loads in wind parks.

In general, the vertical inhomogeneity of the incoming boundary-layer flow, which is modulated by the surface roughness, plays an important role on the distribution of turbulence properties within the turbine wake. In contrast to the axisymmetric structure of wakes developed in free-stream (uniform) flows, the incoming flow inhomogeneity leads to a break down of axisymmetry of the turbulence statistics. It is found that the departure from axisymmetry increases with surface roughness due to the increased non-uniform distribution of velocity and turbulence levels at turbine level induced by the roughness.

As expected, the velocity deficit and the turbulence enhancement decrease with distance as the wake expands. However, these effects remain not negligible even in the very far wake, at a distance of fifteen turbine diameters downwind of the turbine location. Even though the velocity distribution is not axisymmetric, the velocity deficit ($\Delta U_x = U(x > 0, y, z) - U(x < 0, y, z)$) is nearly axisymmetric except near the surface downwind of the location where the wake touches the surface. The distance between the

turbine and that location is found to decrease with increasing surface roughness. The quasi-axisymmetric distribution of the velocity deficit has important implications for the development of models for the velocity distribution and, in particular, the possible extension of existing models for velocity deficit of wakes in free-stream flows.

The wind turbine induces a large enhancement of turbulence levels (positive change in the turbulence intensity) in the upper part of the wake. In the near-wake region, this turbulence enhancement is more pronounced near the turbine edge, which can be explained by the strong shear and the presence of helicoidal vortices (derived from tip vortices) in that region. These vortices induce turbulence levels that are relatively large compared with the background boundary-layer turbulence levels at that height, thus leading to large positive change in turbulence intensity. It was also found that turbulence intensity decreases (loss of turbulent kinetic energy with respect to the incoming flow) in the lower region of the wake due to the reduction of mean shear and production of turbulence kinetic energy with respect to the incoming flow. This effect is more notorious in the rough surface case.

In the far wake region ($x/d \geq 5$), the added turbulence intensity, its positive and negative contributions, as well as the local maximum, decrease with downwind distance following a power law with exponents in the range of $[-0.5, -0.3]$ for the rough surface case. These values are in good agreement with previously reported results for the case of turbines in free-stream flows ([83, 35]). The exponents of decay in the smooth surface case showed more variability. The non-axisymmetric distribution of the turbulent intensity is expected to have an important role in the fatigue loads acting on a turbine placed in the wake of other turbines in wind parks.

Power spectral density of the streamwise velocity was calculated in order to better understand the distribution of the added turbulence levels in the wake as a function of scale. The results indicate that in the far wake the added turbulence intensity is associated with relatively large turbulence scales in the flow. As with the turbulence intensity distribution, the increase in spectral density is also found to be largest near

the upper edge of the wake. Consistent with the turbulence intensity distribution, these differences in the energy content are maximum at $x/d \approx 5$, which corresponds to the transition zone between the near wake and far wake regions. Also consistent with the relatively ‘uniform’ added turbulence intensity distribution in the very far wake region ($x/d \approx 15$), velocity spectra show little differences for different positions within the wake in that region. The effect of the tip vortices on the turbulent kinetic energy of the flow is clearly observed at the top-tip level at $x/d = 1$. There, the power spectral density reveals a jump in the energy at a frequency coincident with the blade rotation. Due to the higher energy levels in the incoming flow near the surface, that peak is not clear at the bottom-tip level.

Future work will consider the effect of atmospheric stability on the turbulent structure and behaviour of the wake. Also, other factors affecting the characteristics of the incoming flow will be considered. These include surface inhomogeneity (e.g., roughness and temperature transitions), topography and the presence of multiple turbines in a wind farm configuration.

Chapter 5

Effects of thermal stability and incoming boundary-layer flow characteristics on wind-turbine wakes: A wind-tunnel study

Wind-tunnel experiments were carried out to study turbulence statistics in the wake of a model wind turbine placed in a boundary-layer flow under both neutral and stably stratified conditions. High-resolution velocity and temperature measurements, obtained using a customized triple wire (cross-wire and cold wire) anemometer, were used to characterize the mean velocity, turbulence intensity, turbulent fluxes, and spectra at different locations in the wake. The effect of the wake on the turbulence statistics is found to extend as far as twenty rotor diameters downwind of the turbine. The velocity deficit has a nearly axisymmetric shape, which can be approximated by a Gaussian distribution and a power-law decay with distance. This decay in the near-wake region is found to be faster in the stable case. Turbulence intensity distribution is clearly non-axisymmetric due to the non-uniform distribution of the incoming velocity in the boundary layer. In

the neutral case, the maximum turbulence intensity is located above the hub height, around the rotor tip location and at a distance of about 4 to 5.5 rotor diameters, which are common separations between wind turbines in wind farms. The enhancement of turbulence intensity is associated with strong shear and turbulent kinetic energy production in that region. In the stable case, the stronger shear in the incoming flow leads to a slightly stronger and larger region of enhanced turbulence intensity, which extends between 3 to 6 rotor diameters downwind of the turbine location. Power spectra of the streamwise and vertical velocities show a strong signature of the turbine blade tip vortices at the top tip height up to a distance of about one to two rotor diameters. This spectral signature is stronger in the vertical velocity component. At longer downwind distances, tip vortices are not evident and the von Kármán formulation agrees well with the measured velocity spectra.

5.1 Introduction

Wind turbine wakes have noticeable effects on both power generation and fatigue loads in wind energy parks. Intensive numerical and experimental efforts have been carried out to better understand these effects [102]. Wake characteristics are expected to depend on the incoming atmospheric boundary-layer (ABL) flow statistics (e.g., mean velocity distribution, turbulent stresses and turbulent fluxes). Of particular importance is the effect of velocity reduction on the mean power and turbulence intensity on the power fluctuations and fatigue loads. In particular Rosen and Sheinman [86] showed that, for practical purposes, turbulence intensity and the intensity of turbine power fluctuations are closely related. Because turbine wakes enhance the turbulence intensity, an increment of power (and voltage) fluctuations is observed in turbines placed in wind parks. These fluctuations can affect the voltage in distribution systems. In addition, the intensity of turbulence may have an important effect on the fatigue accumulations in the structure of a wind turbine.

Atmospheric stability is also expected to have a significant impact on the characteristics of the incoming ABL flow and the structure of wind turbine wakes due to the effect of positive/negative buoyancy on the production/destruction of turbulence. Based on thermal stability (buoyancy effects) and the dominant mechanisms of turbulence generation [97, 8], the ABL can be classified as neutral, convective or stable. Atmospheric stability and its role in wind energy is a subject of increasing research (e.g. [93, 80]). In fact, field experiments performed by van der Berg [100] have shown that atmospheric stability cannot be viewed as a small perturbation to a basic neutral state because important increments on wind shear and power production are observed in stable conditions relative to the neutral atmosphere. For example, a field study of Archer and Jacobson [6] suggests that U.S. wind power at 80 m altitude may be substantially greater than previously estimated because atmospheric stability effects were not taken into account. Van der Berg [100] also showed that atmospheric stability has a significant effect on sound emissions, resulting in higher noise levels with respect to neutral stratification.

Of special interest for wind energy applications is the study of the stable boundary layer (SBL), which is common over land at night. In this flow scenario, the surface is colder than the overlaying air and turbulence is generated by shear and destroyed by negative buoyancy and viscous dissipation. Characterization and prediction of SBL flow is particularly challenging due to the occurrence of complex phenomena such as low-level jets, Kelvin-Helmholz instabilities, meandering motions, partial decoupling between the upper and bottom portions of the boundary layer and increased levels of intermittency [50, 37, 61].

Wind-tunnel experiments have provided useful information about the effects of stable stratification on boundary-layer flow and a number of laboratory studies have been carried out to better understand different aspects of the SBL. For instance, early experiments (e.g., [7, 30, 74]) focused on the flow characteristics and diffusion in the SBL with different Richardson numbers. Recently, Ohya et al. [76] investigated intermittent

bursting in an SBL with a low-level jet. In spite of the different efforts to characterize the SBL, not much is known about the structure and dynamics of wind-turbine wakes in thermally stratified flows. Characterization of wind-turbine wakes under different thermal stratification conditions could provide valuable information for the optimization of wind turbine configurations in wind farms and the validation of parameterizations used in high-resolution computational fluid dynamic models (e.g., large-eddy simulation, LES).

In this study, results are presented from wind-tunnel experiments carried out using a model wind turbine placed inside a boundary layer under both neutral and stable thermal stratification conditions. The wind-tunnel experiments are presented in Section 5.3. Section 5.4 shows a comparison of the wind turbine wake characteristics, measured at different locations downwind of the turbine, for both thermal stratification regimes. Finally, a summary is given in Section 5.5.

5.2 Experimental set-up

A 3-blade wind turbine model was placed in the thermally stratified boundary-layer wind tunnel of the Saint Anthony Falls Laboratory at the University of Minnesota with the goal of studying turbulence characteristics of the wind turbine wake. The model wind turbine was placed in a boundary layer developed over a smooth surface under neutral and stable stratified thermal conditions. The boundary-layer wind tunnel has a plan length of 37.5 m with a main test-section fetch of roughly 16 m and a cross section of 1.7 m \times 1.7 m. There is a contraction with a 6.6:1 area ratio upwind of the test section along with flow conditioning/turbulence control consisting of a coarse wire mesh and honeycomb flow-straightener. The tunnel is driven by a 200 horse-power fan and is operated as a closed return loop. Turbulence intensity in the centre (free stream) of the wind tunnel is approximately 1% for a 2.5 m s⁻¹ freestream velocity. More details on the wind tunnel can be found in Carper and Porté-Agel [23].

The test-section floor consisted of heated exchangers made of aluminum plates 0.3 m long and 25.4 mm thick through which a solution of 30% ethylene glycol was circulated. In addition, a heat exchanger was used to control the temperature of the air in the wind-tunnel expansion after the fan. Electronic valves were used to automatically control (using a Labview code) the required temperatures of both the air flow and the test section floor with an accuracy of $\pm 0.2^\circ\text{C}$.

A turbulent boundary layer was developed with the help of a tripping mechanism (40 mm picket fence) located at the exit of the wind-tunnel contraction, where the test section begins. The turbulent boundary layer was allowed to grow in zero pressure gradient conditions by adjustment of the wind-tunnel ceiling. The resulting boundary layer has a well-developed surface layer with constant shear stress and a logarithmic velocity profile for the neutral stratification regime (see Chamorro and Porté-Agel [26] for more details).

The experiments were conducted with a free stream velocity of approximately 2.5 m s^{-1} . A turbulent boundary-layer depth of $\delta \approx 0.5 \text{ m}$ was obtained at the turbine location for the two stratification cases (neutral and stable). The zero pressure gradient boundary layer had a Reynolds number, based on the boundary-layer depth (δ), of $Re_\delta = U_\infty \delta / \nu \approx 0.93 \times 10^5$, and a friction velocity of $u_* = 0.11 \text{ m s}^{-1}$. The aerodynamic roughness length was found to be $z_0 = 0.05 \text{ mm}$. These parameters (u_* and z_0) were obtained by fitting a logarithmic velocity profile to the measured average velocity in the surface layer (approximately the lowest 15% of the boundary layer).

The stable stratified boundary-layer case was created by cooling the floor to 7°C and heating the wind-tunnel air flow to 60°C . Based on these conditions, the stable boundary layer had a bulk Richardson number $Ri_\delta (= g\delta\Delta T / (T_0 U_\infty^2)) \approx 0.15$, which corresponds to weak stability. Here g is the acceleration due to gravity, ΔT is the temperature difference (in K) between the free stream flow and the surface, T_0 is a reference temperature (in K) and U_∞ is the free stream velocity. Figure 7.4 shows the vertical profiles of the mean velocity, mean temperature, turbulence intensity, kinematic shear

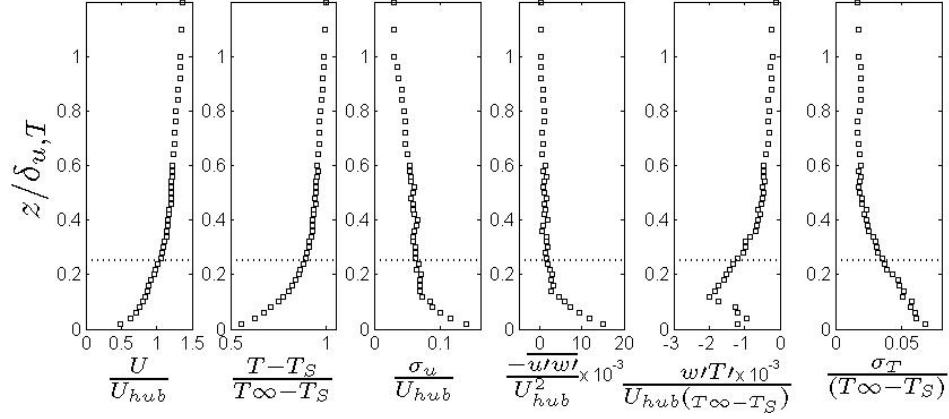


Figure 5.1: Background characteristics of the stable boundary layer: normalized mean velocity, mean temperature, turbulence intensity, kinematic shear stress and kinematic heat flux. The horizontal lines represent the turbine axis. Height is normalized with the turbine radius r .

stress and kinematic heat flux measured in the boundary layer with stable stratification.

Mean wind velocity in the tunnel free stream was measured using Pitot static tubes (mainly for calibration purposes) and a customized 3-wire anemometer. The sensor (a combination of an x-type hot-wire and a single cold-wire) was used to obtain high resolution and simultaneous measurements of 2-velocity components (streamwise and vertical) and temperature. The probe is made of $5.0 \mu\text{m}$ tungsten wires (used as hot wires for velocity measurements) and a $2.5 \mu\text{m}$ wire (used as cold wire for temperature measurements) which are connected to an A.A. Lab Systems AN-1003 10-channel CTA/CCA system (for details see Vukoslavcevic and Wallace [105]). During the calibration and measurements the temperature fluctuations were kept within a $\pm 0.2^\circ\text{C}$ range to avoid bias errors due to thermal drift of the voltage signal.

Calibration of the sensor was performed at the beginning of each experimental run. The 3-wire anemometer was calibrated in the free-stream region, against a Pitot-static probe (for mean velocity) and a thermocouple (for mean temperature), considering seven sensor inclination angles, seven wind velocities at each position. The process was

repeated for four different mean free stream temperatures. A combination of cubic-spline table calibration method were then used to determine the two instantaneous velocity components and temperature. For more details on the calibration procedure, see Bruun [18].

The model wind turbine consists of a three-blade GWS/EP-6030x3 rotor attached to a small DC generator. The turbine angular velocity can be adjusted by changing the resistance of the generator. During the experiments, the tip speed ratio was approximately $\lambda=2\pi r\Omega/[60U_{hub}] \approx 4$, where Ω is the angular velocity of the turbine in r.p.m. and $U_{hub} \approx 2.1 \text{ m s}^{-1}$ is the mean velocity at the hub height. A similar turbine was used by Chamorro and Porté-Agel [26] to study roughness effects on the turbulent properties of the wake under neutral conditions.

The tip speed ratio was adjusted to match that of field-scale turbines (usually between 3.5 and 6). As shown in Figure 5.2, the bottom tip of the turbine was set to a height of 0.67 times the turbine radius, which is similar to that found in large-scale turbines ($\geq 2 \text{ MW}$). The turbine rotor was roughly within the lowest third of the turbulent boundary layer. Despite the scaling issues associated with the difference in Reynolds number between the wind-tunnel flow and the atmospheric boundary-layer flow, our measurements provide detailed key information about the qualitative behaviour of turbine wakes in turbulent boundary-layer flows. It is also important to note that the high-resolution spatial and temporal measurements presented here can be used to systematically test the performance of numerical models (e.g., LES with different subgrid-scale models and wind turbine forces parameterizations) in the simulation of wind turbine wakes in turbulent boundary-layer flows. Okulov and Sorensen [77] have shown also that, although it is not possible to match the Reynolds number of real wind turbines, it is possible reproduce the basic characteristics of the wakes (e.g., wake rotation, tip vortices and helicoidal vortices).

As shown in Figure 5.2, the 3-wire anemometer was placed at different positions downwind of the turbine ($x/d = 2, 3, \dots, 10, 12, \dots, 20$; where d is the turbine diameter).

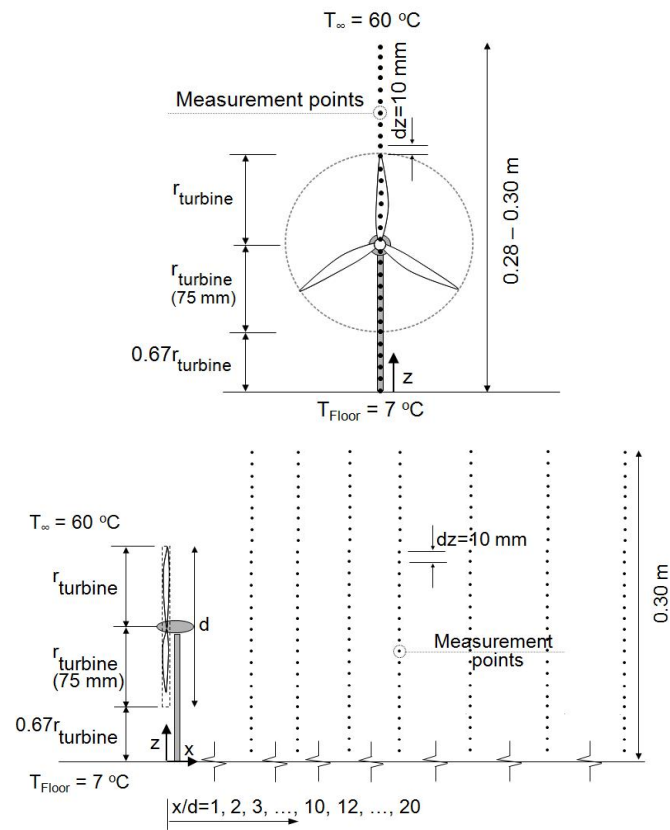


Figure 5.2: Schematic of the wind turbine (front and side views), coordinate system and measurement locations (top and middle), and photograph of the test section with the wind turbine (bottom).

At each location, measurements were taken at zero span ($y = 0$) for elevations ranging from $z = 10$ mm to $z = 300$ mm every $\Delta z = 10$ mm. In addition, a cross-sectional characterization of the wake was obtained at $x/d = 5$. There, measurements were taken in a plane that spans from $z = 0$ to 0.3 m in the vertical direction and from $y/r = -1.60$ to 1.33 in the spanwise direction. On that plane, measurements were taken over a grid of points separated by $\Delta y = \Delta z = 15$ mm. The sensor voltage signatures (of two velocity components and temperature) were sampled at rates of 0.5 and 1 kHz for a measurement period ranging from 30 to 120 s.

5.3 Wake properties

In this section we present flow statistics at different locations downwind of the turbine ($x/d = 2, 3, \dots, 10, 12, \dots, 20$) at zero span (see Figure 5.2) for the two thermal stratification cases (neutral and stable). A cross-sectional characterization of the turbine wake at $x/d = 5$ is also included. Particular emphasis is placed on the distribution of the non-dimensional distribution of the normalized mean velocity, U/U_{hub} (where U_{hub} is the mean velocity at the turbine hub height), turbulence intensity, $I_u = \sigma_u/U_{hub}$, and kinematic shear stress, $\overline{u'w'}/U_{hub}^2$, for the two stratification cases. Figure 5.3 shows the distribution of the normalized mean velocity, U/U_{hub} , on a vertical plane at zero span ($(x, z)|_{y=0}$) for the two stratification cases. In both cases, the momentum loss is evident even at a distance of 20 rotor diameters downwind of the turbine. This figure also reveals clear differences in the mean velocity distribution inside the turbine wake between both thermal stratification cases. In particular, the velocity deficit in the near-wake region appears to be larger in the case of neutral stratification. These differences are associated with the non-uniform velocity distribution of the incoming boundary layer flow, which is affected by thermal stratification. This is also the reason for the non-axisymmetric distribution of the velocity inside the wake, as illustrated in the mean velocity profiles shown Figure 5.4a for the neutral case.

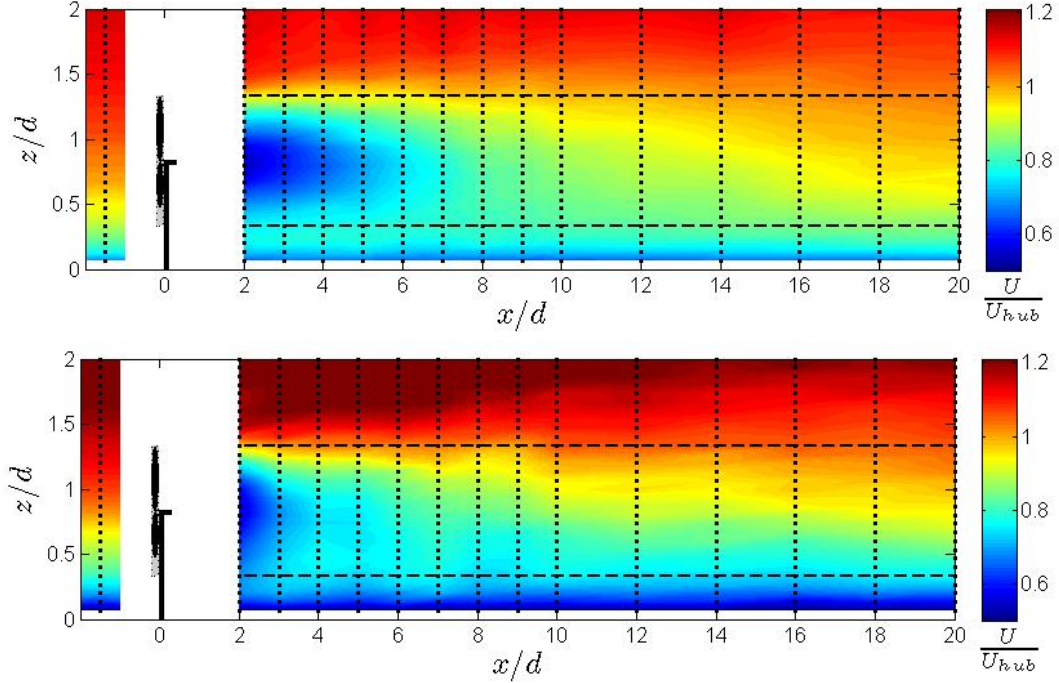


Figure 5.3: Non-dimensional distribution of mean velocity downwind of the turbine at zero span in the neutral (top) and in the stable stratified (bottom) boundary layer. Horizontal-dashed lines represent the turbine bottom and top tip heights and dots indicate measurement locations.

As pointed by Chamorro and Porté-Agel [26], the velocity deficit ($\Delta U_x = U(x > 0, y, z) - U(x < 0, y, z)$), shown in Figure 5.4b, has a nearly axisymmetric shape. Note that in a fully developed boundary layer the incoming flow does not depend on stream-wise and spanwise positions x and y , and therefore $U(x < 0, y, z)$ can be written as simply $U_o(z)$. The overall velocity deficit distribution $\Delta U_x (= U - U_o)$ in a plane perpendicular to the turbine axis (at different downwind locations x in the wake) can be roughly approximated by a Gaussian distribution (Figure 5.4b). This property allows us in principle to extend simple wake velocity formulations, developed for nearly homogeneous inflow conditions and based on similarity arguments (e.g. [41]), to more complex

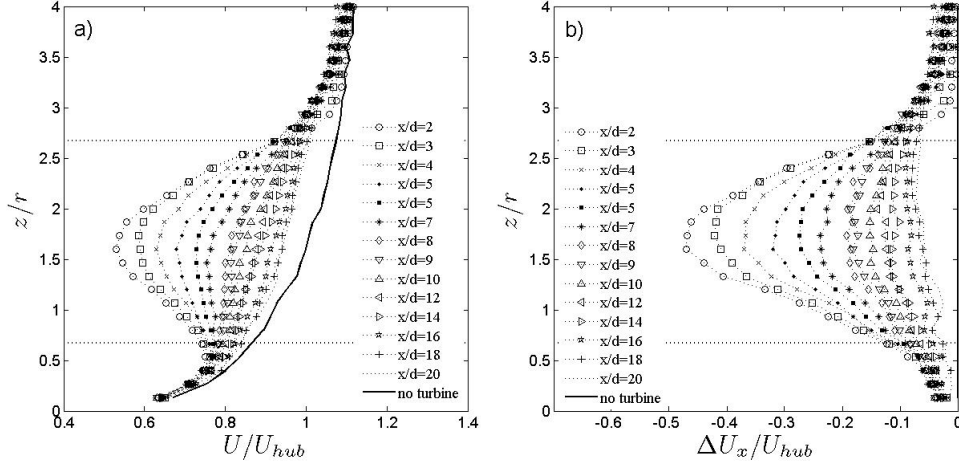


Figure 5.4: Non-dimensional distribution of mean velocity (left plot) and velocity deficit (right plot) downwind of the turbine at zero span. Turbine in the neutral boundary layer. Horizontal-dotted lines represent the turbine bottom and top tip heights.

boundary-layer cases by modeling the velocity deficit in the wake as

$$\Delta U_x(x, r) = \Delta U_{hub}(x) f(r/R), \quad (5.1)$$

where $\Delta U_{hub}(x)$ is the maximum velocity deficit in the wake (approximately at the hub height), r is the distance from the center of the wake and R is a characteristic width of the wake at distance x downwind of the rotor. Equation 6.1 suggests that the velocity deficit at the center of the wake $\Delta U_{hub}(x)$ is key for the characterization of the overall wake. Because it modulates the magnitude of the velocity deficit throughout the wake, its adequate prediction is essential. Different expressions have been proposed for estimating mean velocity at hub height, U_{hub} , or its deficit, ΔU_{hub} . Some of those simple approaches are based on field data fitting (e.g., [12]). Others consider a top-hat wake shape, i.e. uniform velocity distribution inside the wake, (e.g. [52]).

The formulation proposed by Barthelmie et al. [12] is based on fitting field measurements in the wake at the hub height. It states:

$$\frac{\Delta U_{hub}(x)}{U_\infty} = a \left(\frac{x}{d}\right)^b \quad (5.2)$$

where U_∞ is the freestream wind velocity and coefficients (a, b) with values of $(1.03, -0.97)$ or $(1.07, -1.11)$ are equally plausible.

A well-known model for wake velocity with a top-hat shape is the Risoe WAsP model ([52, 55]). This model, based on a linear expansion of the wake, states:

$$U_{wake} = U_\infty \left[1 - (1 - \sqrt{1 - C_T}) \left(\frac{d}{d + 2k_{wake}x} \right)^2 \right], \quad (5.3)$$

where C_T is the thrust coefficient, $k_{wake} = A/\ln(h_{hub}/z_0)$ is a wake decay constant, $A \approx 0.5$, z_0 is the surface roughness and x is the distance from the turbine.

Figure 5.5 shows the change of normalized mean velocity, at turbine hub height, as a function of normalized downwind distance for the two stratification cases. There, a comparison with the models given in Eqs. 5.2 and 5.3 is included. That figure reveals a non-negligible departure between the model proposed by Barthelmie et al. [12] and the measurements at distances $x/d < 12$. Beyond that location the differences are small. The overall comparison of the measurements with the model suggests that the structure of the mean velocity deficit cannot be adequately represented using a power-law decay with exponent ≈ -1 . Actually, as indicated by Schlichting [90], a velocity deficit $\Delta U_x \propto x^{-1}$ holds for a wake developed in a laminar flow (or where diffusion is controlled by a constant ambient turbulent diffusivity).

On the other hand, the Risoe WAsP model (Equation 5.3) clearly underestimates the velocity deficit at all distances. This is expected since, as mentioned above, the model assumes a uniform velocity distribution in the wake, which leads to the observed underestimation at the center of the wake (where the maximum velocity deficit is found). In general, the velocity deficit decays relatively fast up to a distance of roughly $x/d = 10$. Beyond that location, the velocity recovery is markedly slower. From an engineering perspective this

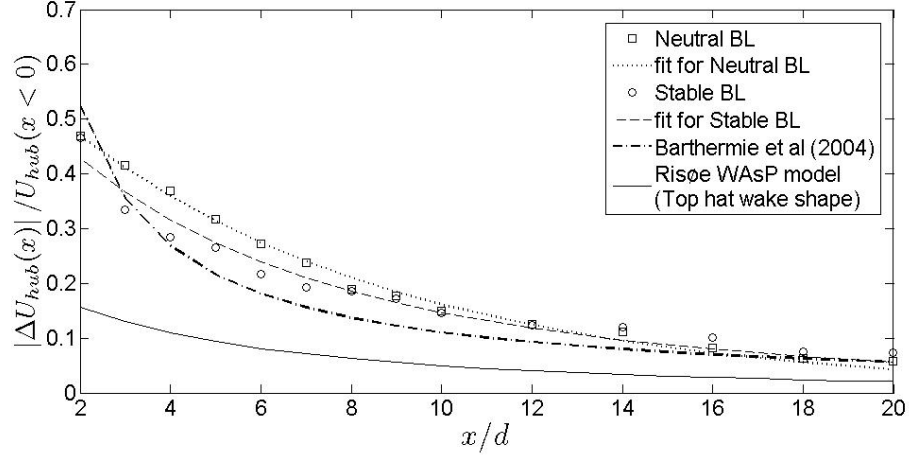


Figure 5.5: Normalized velocity deficit at hub height for the two stratification cases and its comparison with simple models.

implies that the incremental power (ΔP) gained by moving a second turbine, placed in the wake of another turbine, an incremental downwind displacement (Δx) is much larger at $x/d \leq 10$. In particular, it affects the ratio power/area, which is one of the parameters that has to be maximized in wind farm design.

Figure 5.5 also shows that, at distances $x/d < 10$, the velocity recovery appears to be faster in the stable boundary-layer case. Beyond that location, the velocity recovery appears to be similar in both stratification cases. These results agree with field measurements of Magnusson and Shedman [60] showing that, for $Ri > 0.25$, there is a tendency for the velocity deficit to decrease, which would indicate more effective mixing in the wake.

The overall velocity recovery throughout the wake is strongly related to radial transport. In order to better understand this complex relation, we consider the continuity equation in cylindrical coordinates:

$$\frac{1}{r} \frac{\partial}{\partial r} (rU_r) + \frac{1}{r} \frac{\partial}{\partial \theta} (U_\theta) + \frac{\partial U_x}{\partial x} = 0, \quad (5.4)$$

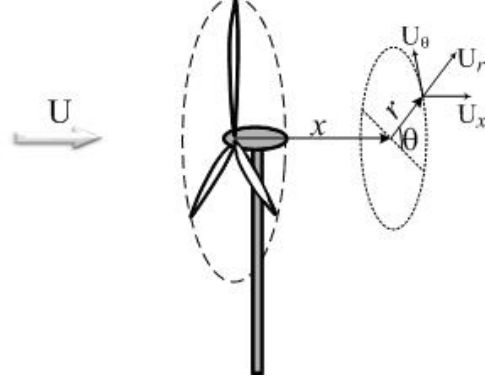


Figure 5.6: Schematic of the cylindrical coordinate system and velocity components.

where a schematic of the positioning of the cylindrical coordinate system is shown in Figure 5.6. The second term in Equation 5.4 is presumably much smaller than

the others due to an expected low dependence of the tangential velocity on angle and therefore, for a first-order analysis, it can be neglected. From Figure 5.4 one notes that the streamwise velocity gradient is clearly positive between (roughly) bottom and top tip heights and negative above the turbine top tip. For the region where $\partial U_x / \partial x > 0$, necessarily:

$$\frac{\partial}{\partial r} (rU_r) < 0 \Leftrightarrow -U_r/r > \partial U_r / \partial r. \quad (5.5)$$

The left part of Equation 5.5 implies that, for $r > 0$, U_r is negative and the right part implies a convex shape of U_r with normal distance r . Similarly, above the top tip $\partial U_r / \partial r < 0$ and $-U_r/r < \partial U_r / \partial r$, suggesting a concave shape of U_r (with U_r approaching zero as r increases). The intersecting point around the top tip height, where the streamwise velocity gradient is nearly zero, is an inflexion point for the radial velocity component. The behaviour of U_r with the positive and decreasing streamwise velocity gradient $\partial U_x / \partial x$ modulates the radial transport through the wake downwind of the turbine. From this it is inferred that, at the very far wake where $\partial U_x / \partial x \approx 0$, the radial transport is low.

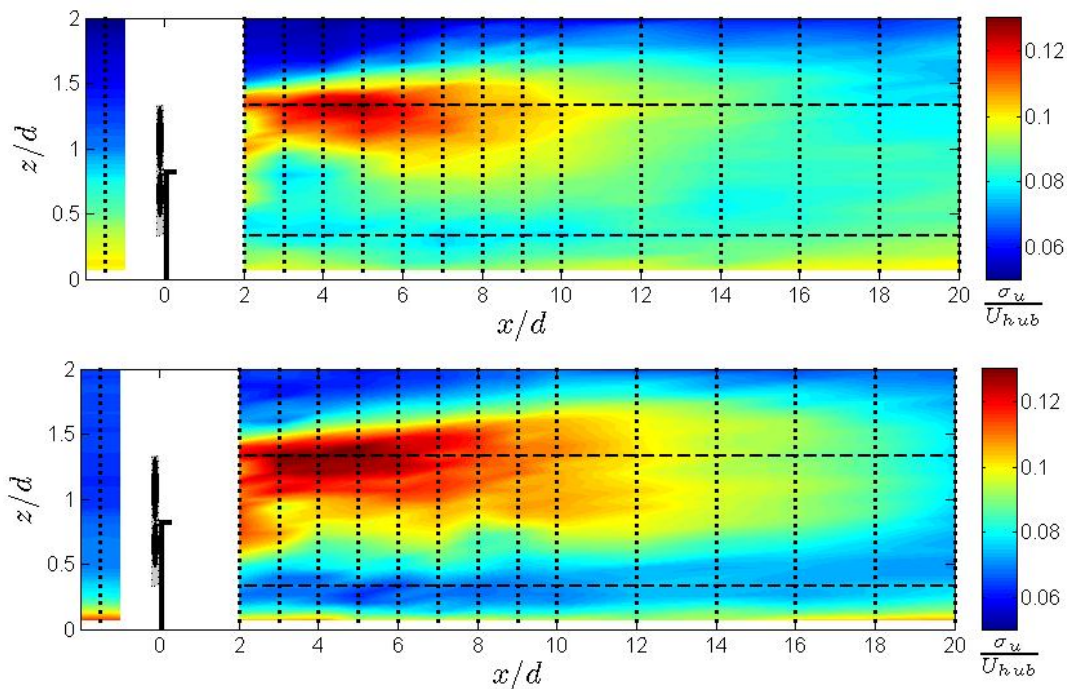


Figure 5.7: Turbulence intensity distribution downwind of the turbine at zero span in the neutral (top) and in the stable stratified (bottom) boundary layer. Horizontal-dashed lines represent the turbine bottom and top tip heights and dots indicate measurement locations.

In the so-called very far wake region ($x/d \geq 10$) the streamwise velocity gradient is markedly smaller, leading to a small radial velocity and a reduced wake growth. Mixing of the wake with the surrounding flow is responsible for the reduced streamwise velocity gradient.

Figure 5.7 shows the turbulence intensity (σ_u/U_{hub}) on a vertical plane at zero span ($(x, z)|_{y=0}$) for both thermal stratification conditions. A strong enhancement of turbulence intensity is found in the wake around the top-tip height. The enhancement of turbulence intensity is associated with strong shear and turbulence kinetic energy production in that region. Due to boundary-layer effects (relatively higher incoming turbulence intensity and shear), negligible effects are observed near the bottom tip

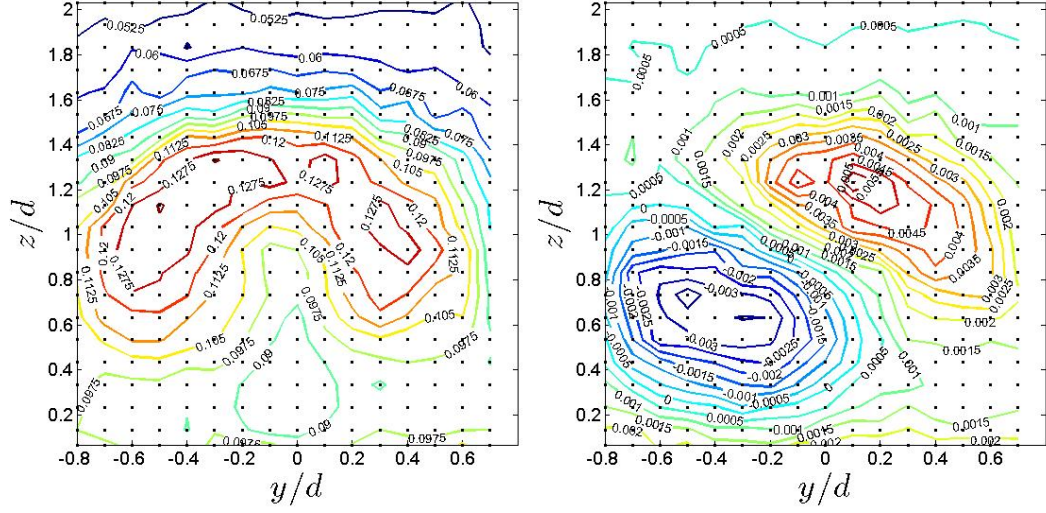


Figure 5.8: Contours of turbulence intensity, σ_u/U_{hub} , (left) and non-dimensional kinematic shear stress, $-\overline{u'w'}/U_{hub}^2$, (right) distributions in the neutral boundary layer at $x/d = 5$. Dots indicate measurement locations.

height, where the mean shear is smaller [26]. In addition to the boundary-layer effects, negative buoyancy acting in the stable case precludes for an enhancement of turbulence intensity in the lower part of the wake.

The region of higher turbulence intensity (above the hub level and near the turbine tip height) extends up to approximately $x/d \approx 8$. Its peak is located between distances of roughly 4 to 5.5 turbine diameters for the neutral case and between 3 to 6 turbine diameters in the stable situation. In addition, the maximum turbulence intensity appears to be larger in the stable case, consistent with the stronger mean shear (and turbulent kinetic energy production) at top tip level on the stable case. This potentially implies stronger turbulent loads and power fluctuations in wind turbines placed inside the wake of another turbine. In fact, an inter-turbine separation of 5 turbine diameters is common practice in wind energy parks.

Figure 5.7 shows also that, in the neutral case, the turbulence intensity profile is

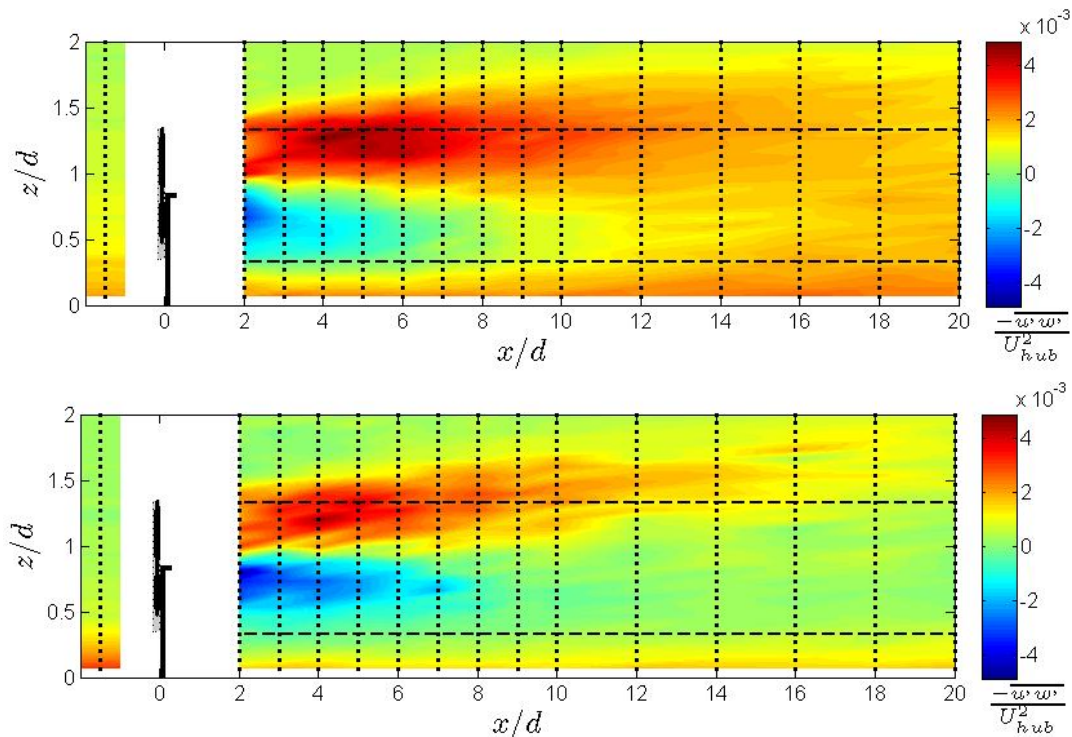


Figure 5.9: Non-dimensional distribution of kinematic shear stress downwind of the turbine at zero span in the neutral (top) and in the stable stratified (bottom) boundary layer. Horizontal-dashed lines represent the turbine bottom and top tip heights and dots indicate measurement locations.

roughly uniform in the very far wake region ($x/d > 10$). The uniformity remains even at a distance of $x/d = 20$, implying that not only is the mean velocity not fully recovered at that location, but also the level of turbulence fluctuations. In the stable case, turbulence intensity does not reach a homogeneous profile at any location and, below the bottom tip height, appears to be consistently smaller than at higher locations.

The non-axisymmetric character of the turbulence intensity distribution is illustrated in the cross-sectional plane at $x/d = 5$ shown in Figure 5.8. There, an enhancement is observed above the hub height, with maximum values around the turbine tip. Some departure from z -axis symmetry (at zero span) is also observed due to the rotation of the

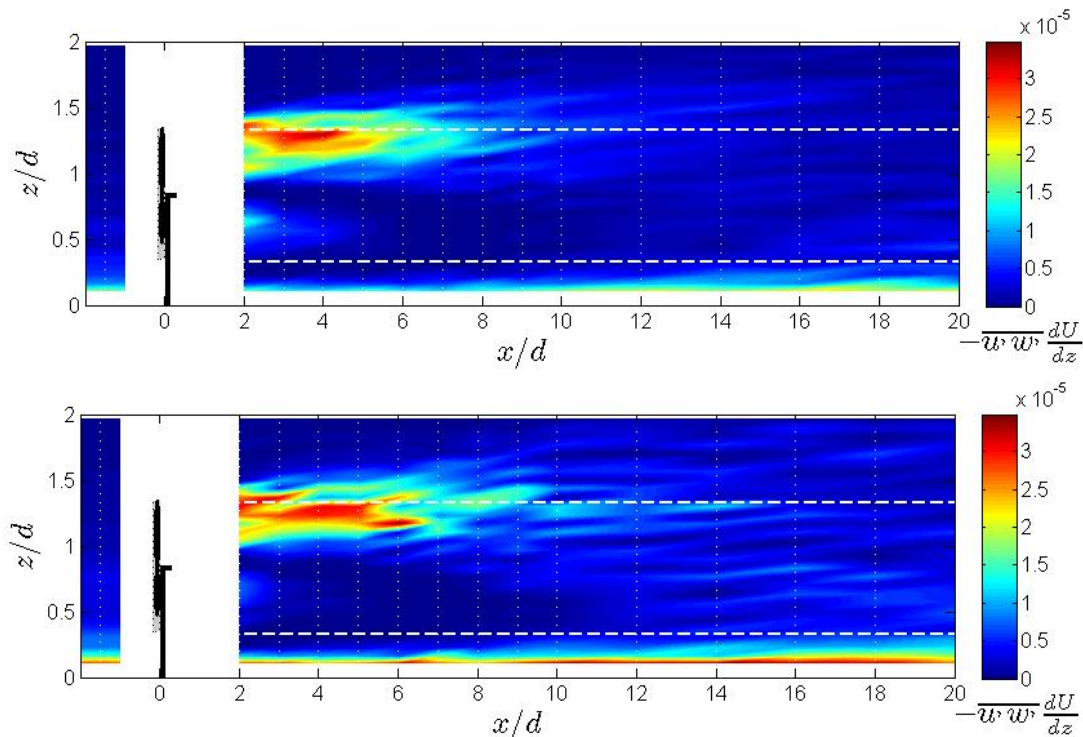


Figure 5.10: Turbulent energy production ($-\overline{u'w'}dU/dz$ component) at different positions downwind of the turbine (at zero span) in the neutral boundary layer (top) and in the stable boundary layer (bottom). Horizontal-dashed lines represent the turbine axes.

wake. The slight departure from symmetry (z -axis) is characterized by a small offset from its zero span axis, which implies a difference in turbulence intensity magnitude on the two sides of the z -axis of the turbine, specifically $I_u(-y_0/d, z_0/d) > I_u(y_0/d, z_0/d)$ where (y_0, z_0) is a location in the wake below the top tip height.

Figure 5.9 shows the distribution of the normalized turbulent shear stress on a vertical plane at zero span ($(x, z)|_{y=0}$) for both thermal stratification conditions. The mixing effect of the wake produces a large positive turbulent stress (downward momentum flux) above the hub height and a negative turbulent stress (upward momentum flux) below the hub height. The positive flux is larger in magnitude and extends to longer downwind

distances due to the relatively larger shear found at the top tip level (compared with the bottom tip level) as shown in Figure 5.4. From Figure 5.9, some differences are also found in the near-wake distribution of the turbulent shear stress between the two stratification conditions. Specifically, in the stable case the magnitude of the positive shear stress is smaller and that of the negative shear stress is larger, compared with the neutral case. In the far wake region ($x/d > 10$), the turbine wake is dominated by roughly negligible shear, in contrast with the neutral case, which shows positive values throughout the vertical profile in that region. It is also important to point out that, as shown in Figure 5.8, the spanwise distribution of the turbulent stress has a strong departure from z -axis symmetry (at zero span) due to the rotation of the wake. As reported by Chamorro and Porté-Agel [26], the maximum values (positive and negative) of the stress are not located on the vertical plane at zero span $(x, z)|_{y=0}$, but on the rotated axis of symmetry and at a radial distance similar to the turbine tip position (radius of the turbine).

In order to further understand the effect of the turbine on the level of turbulence in its wake, Figure 5.10 shows the spatial distribution of the turbulence energy production ($-\overline{u'w'}\partial U/\partial z$ component). Turbulence production is largest in the upper half of the wake (above the hub height) and extends up to a distance of roughly $x/d \approx 8$. The maximum energy production level coincides approximately with the turbine top tip height and it extends between about 3 to 5 rotor diameters. This is consistent with the maximum enhancement of the turbulence intensity reported in Figure 5.7. Similarly, the low energy production level at the bottom tip heights leads to the relatively small turbulence intensity enhancement in that region.

The power spectral density of the streamwise and vertical velocity components, shown in Figure 5.11 at $x/d = 1$ and zero span, reveals the strong signature of the helicoidal tip vortices shed by the turbine blades (peak of the spectrum at a frequency coincident with three times the frequency of the turbine). It is important to note that the tip vortices leave a stronger signature in the vertical velocity spectrum, compared

with the streamwise velocity spectrum.

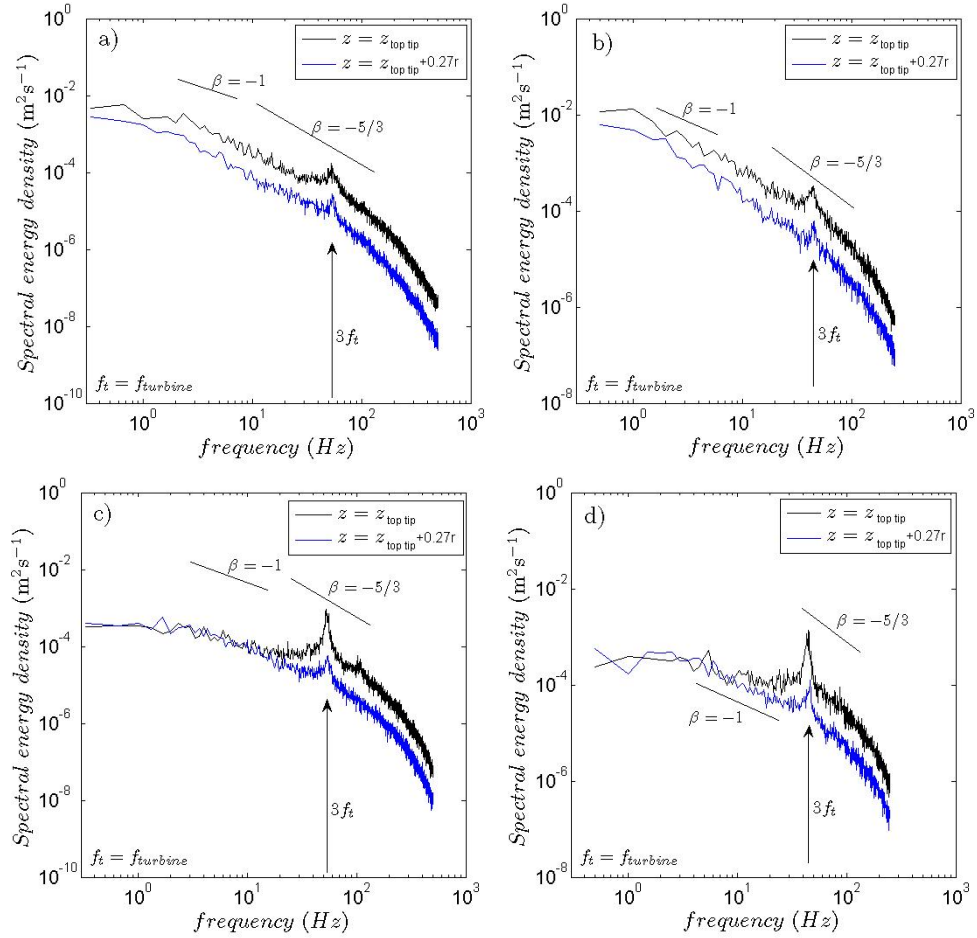


Figure 5.11: Power spectrum of velocity (streamwise and vertical components) at $x/d=1$ in the neutral and stable boundary layers. (a) Streamwise velocity spectrum in the neutral boundary layer; (b) Streamwise velocity spectrum in the stable boundary layer; (c) vertical velocity spectrum in the neutral boundary layer and (d) vertical velocity spectrum in the stable boundary layer

At $x/d = 1$ the effect of the tip vortices on the spectrum is observed up to a height of $0.27r$ (where r is the turbine radius) above the turbine top tip. The frequency associated

with these tip vortices falls within the inertial subrange (spectral slope $\beta = -5/3$). As pointed out by Chamorro and Porté-Agel [26], the relatively high turbulence levels of the incoming flow precludes a noticeable effect of the tip vortices at the bottom tip height (result not shown here).

Next, the applicability of the von Kármán spectrum [104] to represent the structure of the turbulence in the wake is tested using velocity measurements collected at a height coincident with the turbine top tip. The von Kármán spectral density formulation for the streamwise velocity component, $S_u(f)$, and for the vertical velocity component, $S_w(f)$, are given by:

$$\frac{fS_u(f)}{\sigma_u^2} = \frac{4n_u}{(1 + 70.8n_u^2)^{5/6}}, \quad (5.6)$$

$$\frac{fS_w(f)}{\sigma_w^2} = \frac{4n_w(1 + 755.2n_w^2)}{(1 + 283.2n_w^2)^{11/6}}, \quad (5.7)$$

where f is the frequency, σ_u^2 and σ_w^2 are the variances of the streamwise and vertical velocity components, $n_i = fL_i/\bar{U}_i$, and L_i and \bar{U}_i are the i^{th} components of the integral length scale of turbulence (which can be obtained from the autocorrelation function) and mean velocity, respectively.

Figure 5.12 shows the comparison between measured and modelled power spectra of the streamwise and vertical velocity components, respectively, at $x/d = 1$ and 5 behind the turbine, and also in the absence of the turbine. Morfiadakis et al. [71], using field measurements, found that the von Kármán spectrum is suitable for free stream conditions (no turbine), but intense topography and wake effects were not adequately modelled by this formulation.

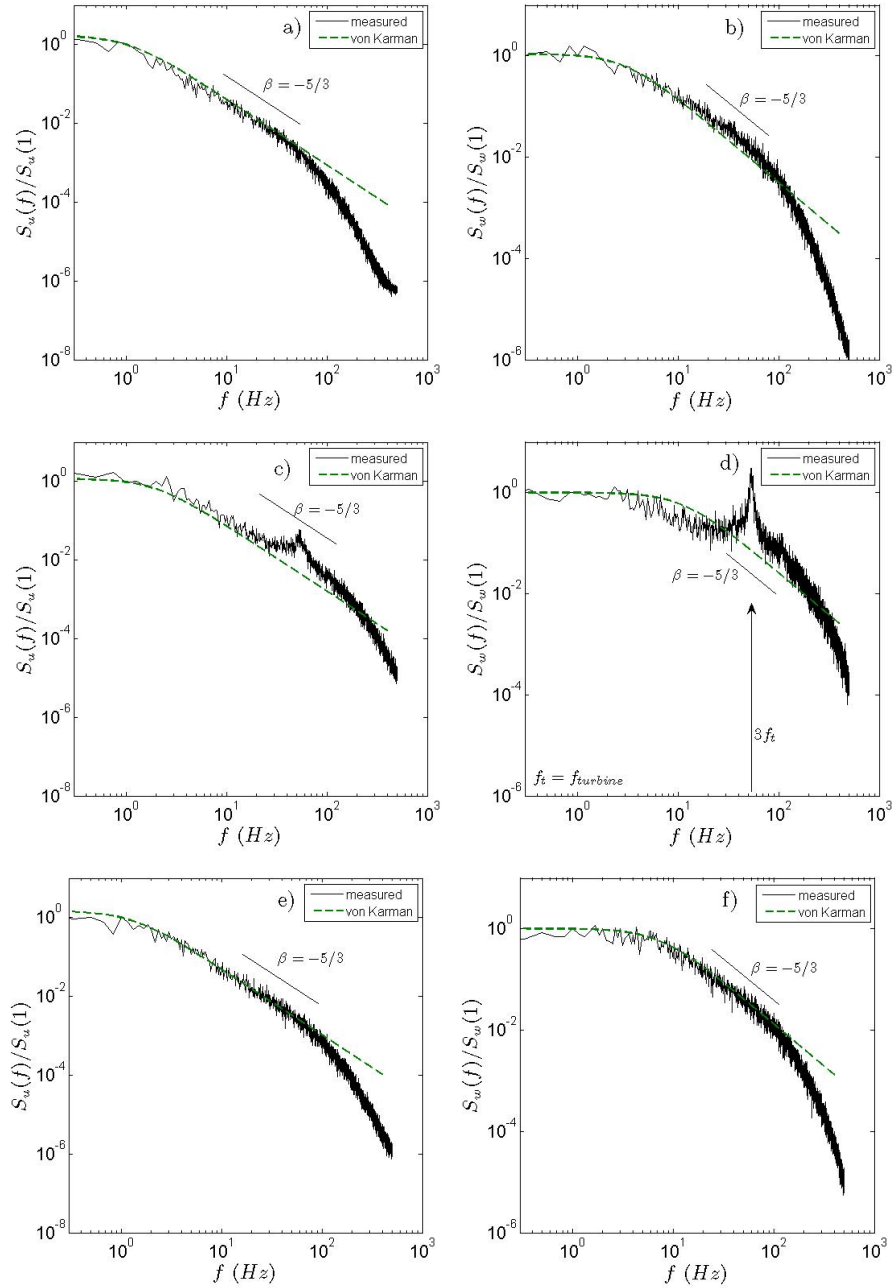


Figure 5.12: Measured and modelled power spectrum of the streamwise (u) and vertical (w) velocity components in the neutral boundary layer at the turbine top tip height. (a) u -component, incoming flow; (b) w -component, incoming flow; (c) $x/d = 1$, u -component; (d) $x/d = 1$, w -component; (e) $x/d = 5$, u -component and (f) $x/d = 5$, w -component.

Our results show that the von Kármán spectrum is able to represent the structure of the turbulence behind the wake in a boundary layer developed over a smooth flat surface (i.e., no significant topographic effects) in the regions where tip vortices have no strong effect on the flow. In fact Figure 5.12 shows good agreement between both spectra (measured and modelled) except at $x/d = 1$, where tip vortices have an intense effect on the structure of the turbulence in a narrow range of frequencies around the blade rotation frequency.

Kinematic heat flux and mean temperature distributions, in the stable boundary-layer case, are affected by the rotating and turbulent nature of the wake. As shown in Figure 5.13, the kinematic-heat flux distribution ($\overline{w'\theta'}$) is strongly affected by the wake in the near-wake region ($x/d < 5$). In that region, the turbulent heat flux is relatively small. In contrast, the wake has a relatively minor effect on the distribution of the kinematic heat flux in the far-wake region.

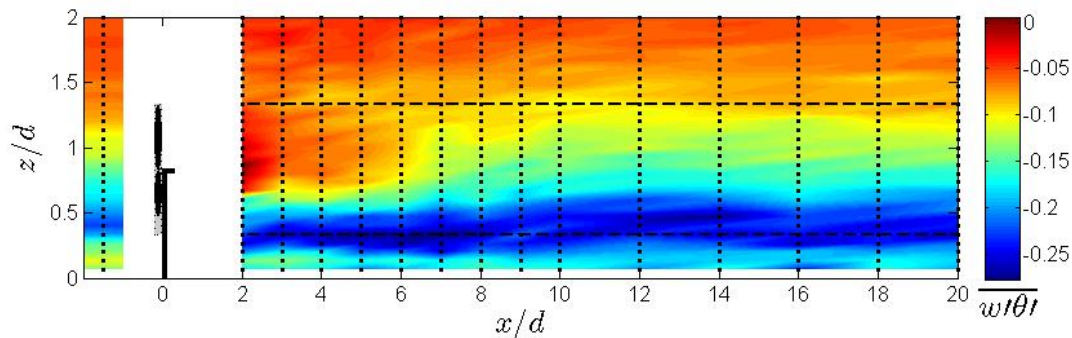


Figure 5.13: Non-dimensional distribution of turbulent heat flux at different locations downwind of the turbine (at zero span) in the stable boundary layer. Horizontal dashed lines represent the turbine bottom and top tip heights and dots indicate measurement locations.

Figure 5.14 shows the mean temperature distribution between the bottom and top tip heights at different distances downwind of the turbine. An increment of temperature

above the hub height is evident between distances of 2 and 8 turbine diameters. At longer distances this effect is negligible, i.e. there is no relevant change in the vertical distribution of temperature with distance. Around the bottom tip height, an increase in temperature is observed at the same distances, which is consistent with the relatively large magnitude of the negative vertical turbulent heat flux in that region.

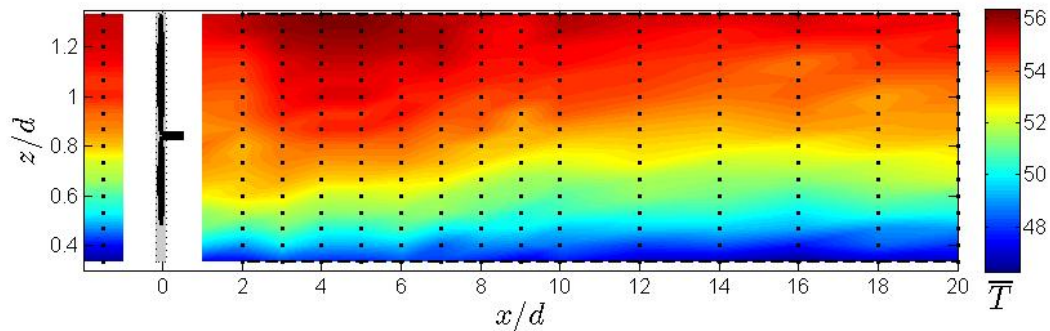


Figure 5.14: Mean temperature distribution ($^{\circ}C$) at different locations downwind of the turbine (at zero span) in the stable boundary layer. Horizontal dashed lines represent the turbine bottom and top tip heights and dots indicate measurement locations.

Wake instability, associated with meandering, can be detected in the low frequency components of the measured velocity in both thermal stratification cases. The characteristic frequency of this large-scale meandering motion is found to be lower in stable stratification by roughly 18% with respect to that found in the neutral case. Figure 5.15 shows the radial (vertical) low frequency velocity spectrum, at the turbine hub-height and $x/d = 1$, for the two thermal stratification cases (there, a Butterworth low-pass filter with a cut-off frequency of 15 Hz was applied). From that Figure, the predominant frequencies associated with the meandering motion are $f_m \approx 6.7$ Hz and $f_m = 5.5$ Hz for the neutral and stable boundary-layer cases respectively, with characteristic secondary motions measured up to a distance of $x/d \approx 4$ (results not shown here). In general, these motions are affected by the turbine thrust coefficient (C_T) and tip speed

ratio (λ) as shown by Medici and Alfredsson [67], who detected them (at frequencies around 10 Hz) in wind-tunnel experiments at $x/d = 1$ behind a miniature turbine in a boundary-layer flow.

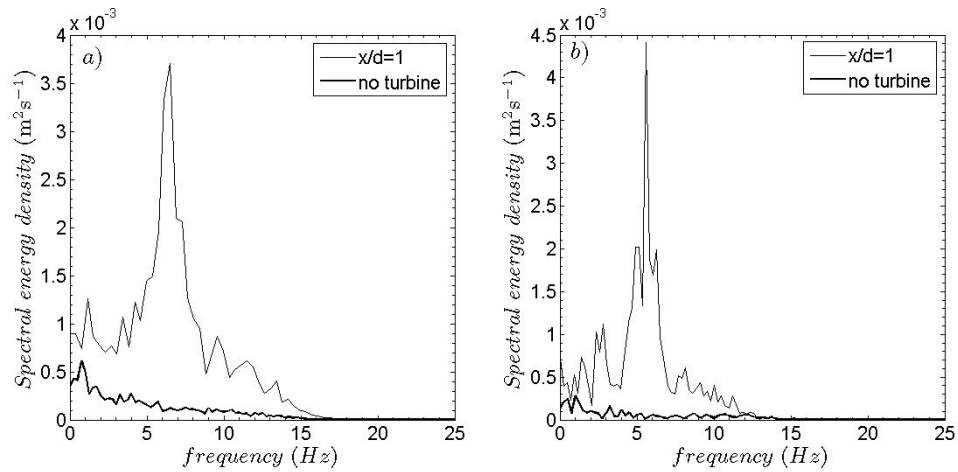


Figure 5.15: Power spectrum of the low frequency components of the radial velocity at the turbine hub height and $x/d = 1$: (a) neutral boundary layer; (b) stable boundary layer.

5.4 Summary

Wind-tunnel experiments were carried out to study turbulent statistics in the wake of a model wind turbine placed in a boundary layer flow under both thermally neutral and stably stratified conditions. A customized 3-wire anemometry (cross-wire and cold wire) was used to obtain high resolution and simultaneous measurements of temperature and two velocity components (streamwise and vertical) at different locations behind the wind turbine. Flow statistics (mean velocity, turbulence intensity, kinematic shear stress) were calculated in the two thermal stratification scenarios for comparison and spatial characterization ($x - z$ plane at zero span). The kinematic heat flux and mean

temperature distributions were also calculated in the stable case.

Results show a clear effect of the turbine wake on the turbulence statistics as far as twenty rotor diameters downwind of the turbine. The velocity deficit is found to have a nearly axisymmetric shape, which can be approximated by a Gaussian distribution in the directions perpendicular to the turbine axis. The maximum deficit is located at the hub height and follows a power-law decay with distance from the turbine. The rate of decay is found to be higher in the stable stratified case. This simple behaviour of the velocity deficit could be used to develop (or extend existing) simple wake velocity formulations, based on similarity arguments and conservation of momentum, to account for the distortion of the mean velocity profile in the wake of wind turbines placed in boundary-layer flows.

Due to the non-uniform distributions of the incoming mean velocity and velocity fluctuations, the turbulence intensity does not show axisymmetric behaviour, and is found to be stronger above the hub height and around the turbine tip. The enhancement of turbulence intensity is associated with strong shear and turbulence kinetic energy production above the hub height. Due to boundary-layer effects (relative higher incoming turbulence intensity and shear), negligible effects are observed near the bottom tip. In addition to the boundary-layer effects, negative buoyancy acting on the stable case precludes an enhancement of turbulence intensity in the lower part of the wake. Maximum turbulence intensity in the neutral case is found to be located at a distance of about 4 to 5.5 rotor diameters, which are common separations between wind turbines in wind farms. In the stable case, the stronger shear in the incoming flow produces a slightly greater turbulence intensity above the hub height, which extends between 3 to 6 rotor diameters downwind of the turbine location.

Power spectra of streamwise and vertical velocity components show strong influence of the tip vortices on the flow at the top tip height at $x/d = 1$, with stronger effects in the vertical velocity component. Our analysis also shows the suitability of the von Kármán power spectrum formulation to represent the structure of the turbulence in

regions of the wake where tip vortices have no important effects. In the stable case, the power spectrum of temperature fluctuations does not show a clear effect of the tip vortices.

Evidence of wake meandering is detected in the low-frequency range of the velocity power spectrum for the two stratification cases. The characteristic frequency of this large-scale motion is found to be lower in the stable case by roughly 18% with respect to that found in the neutral case. Specifically, predominant peaks at $f_m \approx 6.7$ and $f_m \approx 5.5$ Hz are found in the neutral and stable scenarios, respectively. This meandering is evident up to a distance of $x/d = 4$.

Chapter 6

Flow structure around a variable size wind farm. A wind tunnel study

Wind-tunnel experiments were carried out to better understand boundary layer effects on the flow pattern inside and above a variable size model wind farm under thermally neutral conditions. X-type hotwire anemometry was used to characterize the turbulence structure at different locations around a 10 by 3 array of model wind turbines aligned with the mean flow considering two different layouts (inter-turbine separation of 5 and 7 rotor diameters in the direction of the mean flow by 4 rotor diameters in its span). Results suggest that the turbulent flow can be characterized in two broad regions. The first, located below the turbine top tip height, has a direct effect on the performance of the turbine. The mean flow statistics appear to reach equilibrium as close as the third to fourth row of wind turbines independent of the layout, but turbulence statistics showed dependence with the wind farm configuration. In the second region, located right above the first region, flow adjusts slowly. There, two layers were found: an internal boundary layer where flow is affected by the wind turbine array and an equilibrium layer, where

flow statistics are adjusted. An adjusted logarithmic velocity distribution was found in the second region starting from the sixth row of wind turbines. Upwind of this location the velocity profile transitions from its incoming condition. In the fully adjusted log region the effective surface roughness length, induced by the wind farm, was found to be higher than that predicted by some existing models. Momentum recovery and turbulence intensity were found to be affected by the wind farm layout. Power spectra show that the signature of the tip vortices, in both streamwise and vertical velocity components, is highly affected by both the relative location in the wind farm and the wind farm layout.

6.1 Introduction

Enormous efforts are being carried out to reduce our global dependence on fossil fuels due to their harmful effects on the environment and their non-renewable character. In that context, wind power is one of the most attractive alternatives of renewable and clean sources of energy due to its vast potential and availability ([46]). Although a number of wind farms are currently in operation, there are fundamental issues that need to be addressed in order to satisfy the increasing demand for larger, more reliable, and more efficient wind farm configurations. For instance, velocity deficit and turbulence levels in the wake of wind turbines are aspects of special relevance in the process of determining the optimum wind farm layout. Because the turbulent flow inside a wind farm is characterized (among other factors) by the co-existence and superposition of multiple wakes, power losses due to wake effects can reach easily 10-20% of the total power ([11]). Turbulence intensity, another common aspect of interest, is associated directly with fatigue accumulations in a turbine ([86]) and, as pointed out by Binh et al. [13], also plays a direct role on the forces and bending moment acting on a wind turbine. In spite of its importance, there is no well-validated model for the prediction of the spatial distribution of turbulence intensity inside wind farms ([20]). Intensive research,

both numerically and experimentally, has been carried out to better understand these aspects ([102]).

Another subject of special concern is the potential effect of large wind farms on local meteorology. Numerical experiments performed by Roy et al. [88] suggest that turbulence generated by wind turbines can enhance vertical mixing of momentum, heat, and scalars, leading to a warming and drying of the surface air and reduced surface sensible heat flux. Its influence becomes regional as the size of wind farms increases ([94]). In addition, experiments performed under stable stratification by Chamorro et al. [29] showed that significant reduction of mean surface heat flux is induced by a large wind farm.

A detailed characterization of the turbulent flow in a wind farm is a challenging task. The coexistence of multiple and superimposed wakes, the effects of boundary layer, local topology, turbulence levels, and thermal stratification, among other factors, inhibit the understanding of that particular turbulent flow. Theoretical studies have focused on the characterization of the flow inside a wind farm. Most of those studies consider the flow far away from the boundary effects, so that flow properties can be considered adjusted (e.g., [39]). Other approaches focus on the potential large-scale effects imposed by a large wind farm by considering the overall wind farm as an added surface roughness (e.g., [56]).

Overall, the great complexity of the flow in a wind farm limits our ability to correctly predict the performance and structural stability of the individual turbines. Although numerical simulations are a promising way to address this problem, their limitations (e.g., parameterization uncertainties, resolution) suggest we complement their use by seeking additional/alternative approaches. Field and wind tunnel experiments play a key role in obtaining answers to wind power phenomena. In particular, wind tunnel experiments offer valuable insights about the turbulence structure in a wind farm under controlled conditions. Early experiments of Milborrow [68] focused on the average efficiency of an array of wind turbines. Recently, Corten and Schaak [34] investigated

average velocity profiles above a large wind farm. They found that classical wind farm models often overestimate the efficiency of large wind farms by assuming that the wind turbine wakes do not build-up after a few rows down the farm.

In spite of the various efforts to characterize the turbulent flow behaviour around a wind farm, we do not clearly understand the flow properties inside and above it, how the flow adjusts as it progresses inside the wind farm, nor how the transport process could be affected. Certainly, the understanding of these phenomena would help in the optimization of wind farm layout, and also in the development of more accurate parameterizations in large scale models.

In this study, we attempt to contribute to the understanding of the turbulence structure of the flow inside and above a large wind farm. Results are presented from wind-tunnel experiments carried out using a 10 by 3 array of aligned model wind turbines under two different spatial configurations. The wind-tunnel experiments are presented in Section 6.3, Section 6.4 shows the flow characterization inside and above the wind farm, and a summary is given in Section 6.5.

6.2 Experimental set-up

A 10 by 3 array of model wind turbines, aligned with the mean flow, was placed in the thermally stratified boundary-layer wind tunnel of the Saint Anthony Falls Laboratory at the University of Minnesota with the goal of studying turbulence characteristics of the flow inside and above the wind array. The model wind farm was placed in a boundary layer developed over a smooth surface under neutrally-stratified conditions. The boundary-layer wind tunnel has a plan length of 37.5 m with a main test section fetch of roughly 16 m and a cross section of 1.7 m \times 1.7 m. There is a contraction with a 6.6:1 area ratio upwind of the test section along with flow conditioning/turbulence control consisting of a coarse wire mesh and honeycomb flow-straightener. The tunnel is driven by a 200 horse-power fan and is operated as a closed return loop. Turbulence

intensity in the centre (free stream) of the wind tunnel is approximately 1% for a 2.5 ms^{-1} freestream velocity. More details on the wind tunnel can be found in Carper and Porté-Agel [23].

Neutral conditions in the wind tunnel are sustained by controlling both the air and floor temperatures. The floor of the test section consists of heated exchangers made of aluminum plates 0.3 m long and 25.4 mm thick through which a solution of 30% ethylene glycol was circulated. In addition, a heat exchanger was used to control the temperature of the air in the wind tunnel expansion after the fan. Electronic valves were used to automatically control (using a Labview code) the required temperatures of both the air flow and the test section floor with an accuracy of $\pm 0.2^\circ\text{C}$.

A turbulent boundary layer was developed with the help of a tripping mechanism (40 mm picket fence) located at the exit of the wind tunnel contraction, where the test section begins. It was allowed to grow in zero pressure gradient conditions by adjustment of the wind tunnel ceiling. The resulting boundary layer has a well-developed surface layer with constant shear stress and a logarithmic velocity profile for the neutral stratification regime. See Chamorro and Porté-Agel [26] for more details.

The experiments were conducted with a free-stream velocity of approximately 3.0 m s^{-1} . A turbulent boundary layer depth of $\delta \approx 0.5 \text{ m}$ was obtained at the turbine location. The zero pressure gradient boundary layer had a Reynolds number, based on the boundary layer height (δ), of $Re_\delta = U_\infty \delta / \nu \approx 1.12 \times 10^5$, and friction velocity of $u_* = 0.13 \text{ m s}^{-1}$. The aerodynamic surface roughness length was found to be $z_0 = 0.05 \text{ mm}$. These parameters (u_* and z_0) were obtained by fitting a logarithmic velocity profile to the measured average velocity in the surface layer (approximately lowest 15% of the boundary layer).

Mean wind velocity in the tunnel free stream was measured using Pitot static tubes (mainly for calibration purposes) and a cross-wire anemometer. The sensor was used to obtain high resolution and simultaneous measurements of two velocity components (streamwise and vertical). The probe is made of $5.0 \mu\text{m}$ tungsten wires which are

connected to an A.A. Lab Systems AN-1003 10-channel CTA/CCA system. During the calibration and measurements the temperature fluctuations were kept within a $\pm 0.2^\circ\text{C}$ range to avoid bias errors due to thermal drift of the voltage signal. The sensor voltage signatures were sampled at rates of 1 kHz for a measurement period ranging from 60 to 120 s.

Calibration of the cross-wire anemometer was performed at the beginning of each experimental run. Also a post-experiment calibration was carried out to check the validity of the calibration throughout the experiment. The anemometer was calibrated in the free-stream region against a Pitot-static probe, considering seven sensor inclination angles and seven wind velocities at each position. A cubic-spline table calibration method was then used to determine the two instantaneous velocity components from the two instantaneous voltage signatures. For more details on the calibration procedure, see Bruun [18].

The flow around the 10 by 3 wind turbine array was studied under two different layouts. The distance between consecutive wind turbines was set to five and seven rotor diameters ($S_x = \Delta x/d = 5$ and 7 , where d is the turbine diameter) in the direction of the flow by four rotor diameters in the spanwise direction ($S_y = 4$). Each model wind turbine consists of a three-blade GWS/EP-6030x3 rotor attached to a small DC generator. The turbine angular velocity can be adjusted by changing the resistance of the generator. During the experiments, the tip speed ratio ($\lambda = 2\pi r\Omega/[60U_{hub}]$, where Ω is the angular velocity of the turbine in r.p.m. and $U_{hub} \approx 2.1 \text{ m s}^{-1}$ is the mean velocity at the hub height) was set to approximately 4 for the first row of wind turbines. A similar turbine was used by Chamorro and Porté-Agel [26] to study roughness effects on the turbulent properties of the wake under neutral conditions and by Chamorro and Porté-Agel [27] to study thermal stratification effects on the flow structure in the wake of a wind turbine.

The tip speed ratio was adjusted to match that of field-scale turbines (usually between 3.5 and 6). As shown in Fig. 6.1, the bottom tip of the turbine was set to a

height of 0.67 times the turbine radius, which is similar to that found in large-scale turbines (≥ 2 MW). The turbine rotor was roughly within the lowest third of the turbulent boundary layer. Despite the scaling issues associated with the difference in Reynolds number between the wind-tunnel flow and the atmospheric boundary-layer flow, our measurements provide detailed key information about the behaviour of turbine wakes in turbulent boundary-layer flows. It is also important to note that the high-resolution spatial and temporal measurements presented here can be used to systematically test the performance of numerical models (e.g., LES with different subgrid-scale models and wind turbine forces parameterizations) in the simulation of wind turbine wakes in turbulent boundary-layer flows. Okulov and Sorensen [77] have also showed that, although it is not possible to match the Reynolds number of real wind turbines, it is possible to reproduce the basic characteristics of the wakes (e.g., wake rotation, tip vortices, and helicoidal vortices).

As shown in Fig. 6.1, the cross-wire anemometer was placed at different positions inside the wind farm ($x_i/d = 1, 2, \dots, 5, (6, 7)$; where x_i is the relative downwind distance from the i^{th} turbine, for $i = 1, 2, 3, \dots, 7$ and 10). At each location, measurements were taken at zero span ($y = 0$) for elevations ranging from $z = 10$ mm ($= 0.05H$ being H the turbine height) to $z = 300$ mm ($= 2H$) every $\Delta z = 10$ mm ($= 0.05H$) between $z = [0, 1.5]H$ and $\Delta z = 20$ mm ($= 0.1H$) between $z = [1.5, 2]H$.

6.3 Flow characterization

In this section we present mean flow statistics at different locations inside and above the model wind farm at zero span (see Fig. 6.1) for the two layouts ($S_x = 5$ and 7 with $S_y = 4$) detailed in the previous section. Emphasis is placed on the distribution of normalized mean velocity, U/U_{hub} (where U_{hub} is the mean velocity at the turbine hub height), turbulence intensity, $I_u = \sigma_u/U_{hub}$, kinematic shear stress, $-\overline{u'w'}/U_{hub}^2$ and other properties such as turbulence energy production, $-\overline{u'w'}\partial U/\partial z$ component, and

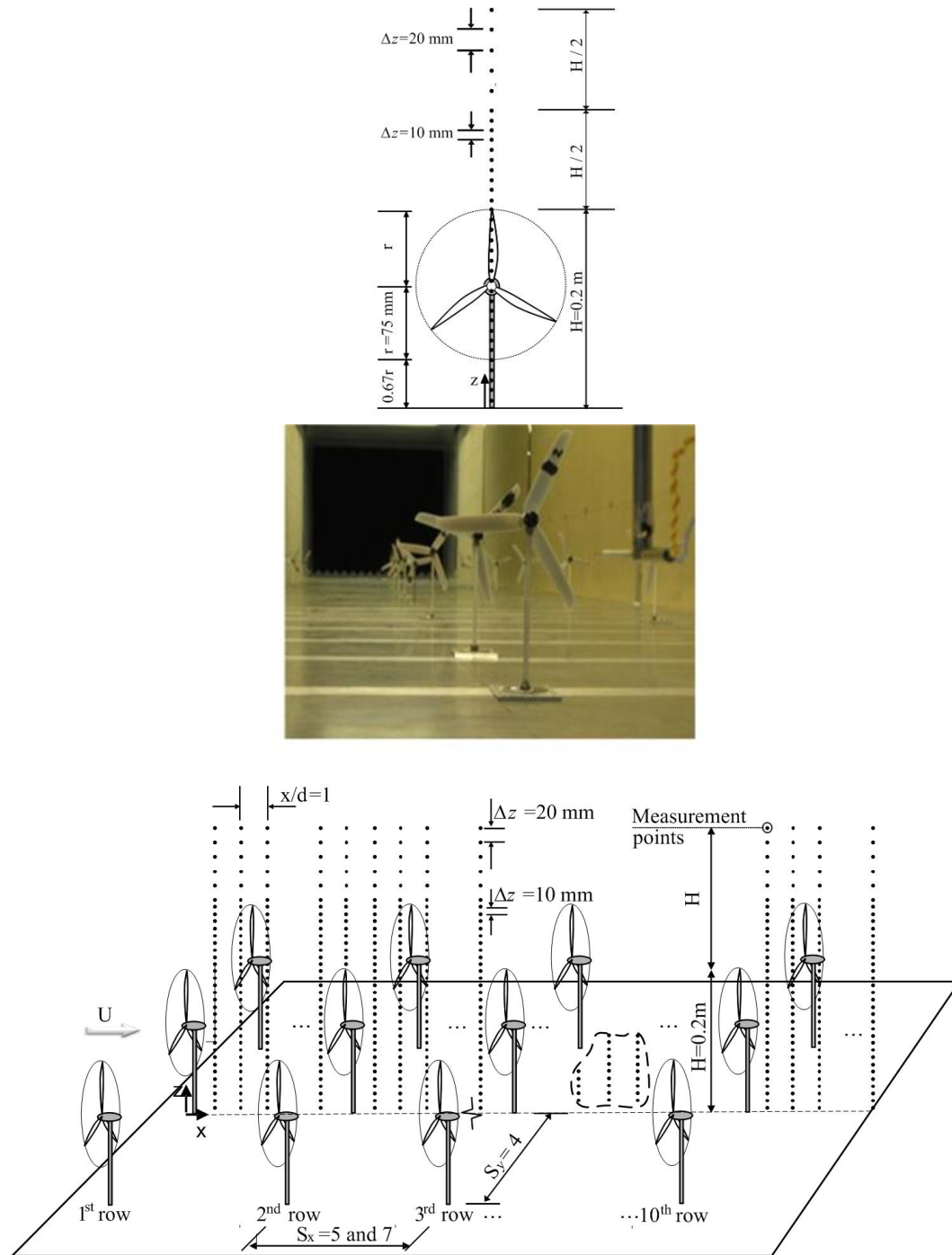


Figure 6.1: Schematic of the 10 by 3 wind turbine array. Turbine dimensions and measurement locations (top and bottom), and photograph of the test section with the turbines (middle).

velocity spectra.

6.3.1 Mean velocity distribution

Mean velocity distribution around the wind farm for the case $S_x = 5$ and $S_y = 4$ is depicted in Fig. 6.2. Based on the downwind distance required to reach nearly adjusted statistics, our results suggest that mean velocity can be characterized in two broad regions. The first region is located below the wind farm top tip height, and has a direct effect on the performance of the wind turbines. In that region, the mean flow appears to reach equilibrium as close as the third to fourth wind turbine row. The second region is located right above the first region and flow adjustment is slower.

The fast velocity adjustment observed below the turbine's top tip (hereon region I) is responsible for the relatively quick adjustment of the wind-turbine angular velocities as close as the third row of turbines in the wind farm, (see Fig. 6.2). Indeed, minor changes of angular velocity are observed after the third-fourth row of wind turbines for each of the two layouts considered ($S_x = 5$ and 7). The differences observed in the distribution of angular velocity in the two cases (roughly 8%) suggest that the total power of the wind farm is very sensitive to the geometrical layout.

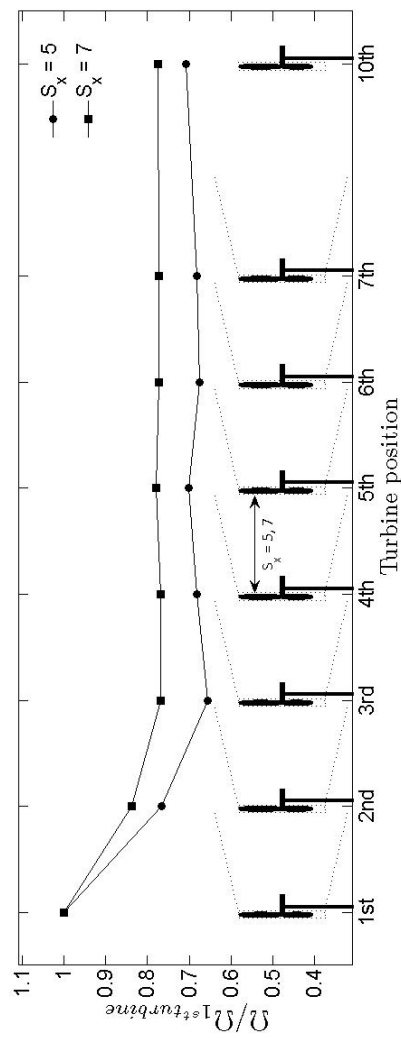
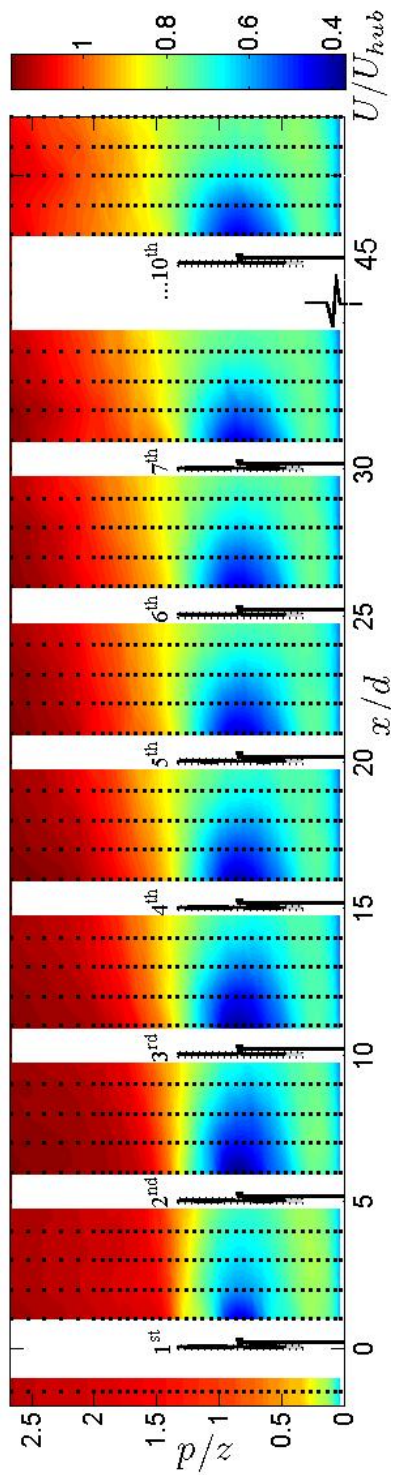


Figure 6.2: Non-dimensional distribution of mean velocity around the wind farm with $S_x = 5$ (top) and normalized angular velocity distribution of the different wind turbines with $S_x = 5$ and $S_x = 7$ (bottom). Dots indicate measurement locations.

Selected vertical velocity profiles at $x/d = 2$ behind the third, fourth and the fifth row of wind turbines, shown in Fig. 6.3, reveal the fast adjustment of the mean velocity below the top tip height. In contrast, above the top tip (hereon region II) velocity profiles appear to be far from equilibrium, evidencing different mechanisms of mixing and transport of the mean flow between the two regions.

The non-axisymmetric shape of the velocity profile observed in region I, induced by the boundary layer (see Fig. 6.3a, complicates its parameterization. As pointed out by Chamorro and Porté-Agel [27], the mean velocity deficit ($\Delta U_x = U - U_{incoming}$) in the wake of a single wind turbine placed in a boundary layer flow is approximately axisymmetric. Due to the interaction of the multiple (superimposed) wakes and the boundary condition imposed by the surface, which limits the wake expansion, velocity deficit (ΔU_x) is not strictly symmetric below the bottom tip and above the top tip heights. Between those heights, mean flow shows a reasonable symmetric shape.

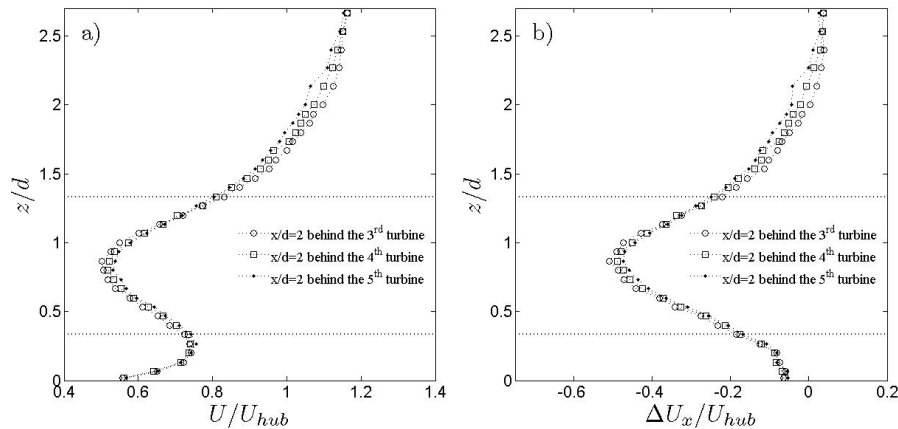


Figure 6.3: Normalized streamwise velocity component distribution (left) and its deficit (right) in the wind farm.

Although different approaches have been proposed to estimate the mean velocity inside a wind farm, they unfortunately do not fully consider the boundary layer effects.

Similar to the velocity deficit formulation downwind of a single wind turbine, suggested by Chamorro and Porté-Agel [27], the velocity deficit in an aligned wind farm can be described by

$$\Delta U_x(x, r)|_i = \Delta U_{hub}(x)|_i f(r/R), \quad (6.1)$$

where $\Delta U_x(x, r)|_i$ is the velocity deficit in the wake of the i^{th} row of wind turbines, $\Delta U_{hub}(x)|_i$ is its counterpart at the hub height, r is the distance from the center of the wake and R is the characteristic width of the wake at distance x downwind of the rotor. Because mean velocity adjusts relatively fast (see Fig. 6.2), Eqn. 6.1 becomes quickly independent of the relative position i in the farm.

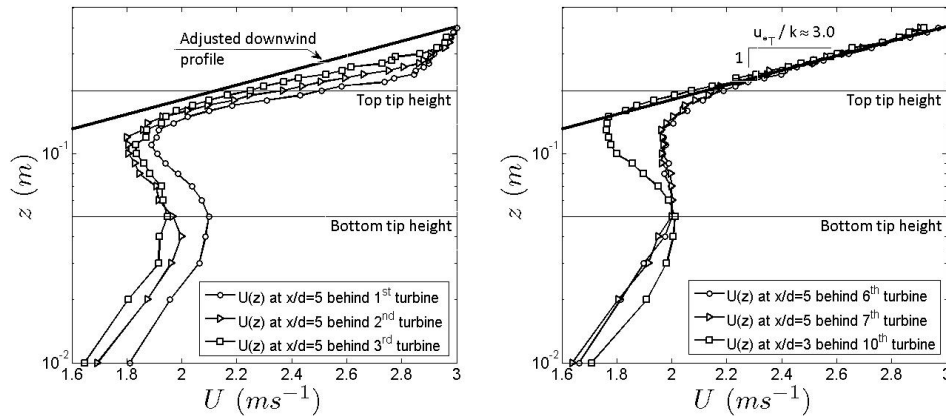


Figure 6.4: Non-adjusted (left) and adjusted (right) mean velocity profiles above the top tip in the wind farm at different locations ($S_x = 5$). Horizontal lines represent the turbine bottom and tip heights.

Figure 6.4 shows clearly that mean velocity above the top tip height (region II) adjusts far inside the wind farm. Velocity appears to reach equilibrium starting from the sixth row of wind turbines, and upwind of this location, flow is clearly transitioning. Relative location where the flow reaches equilibrium is of special importance. For

instance, large-scale models require the specification of the additional surface roughness induced by a wind farm. That parameter should be obtained under equilibrium conditions, where similarity theory can be considered. In general, a departure of the log-law velocity distribution is expected downwind of a surface roughness transition. Indeed, both mean velocity and surface shear stress adjust slowly downwind of a transition ([25]; [28]).

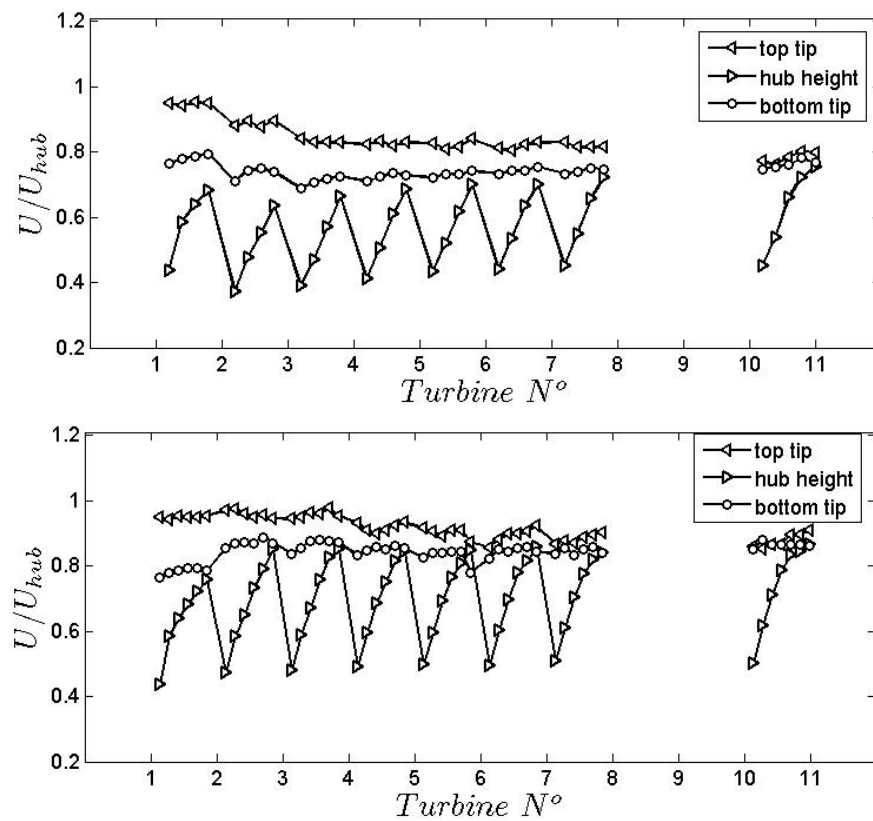


Figure 6.5: Normalized streamwise velocity component distribution in the wind farm. $S_x = 5$ (top) and $S_x = 7$ (bottom).

Because the transitioning zone appears to be significant in the wind farm (6-7 rotor diameters), its characterization appears to be relevant in the understanding of the

transport processes between the two regions and the interaction between the wind farm and the boundary layer which, at the end, modulates the power available in the wind turbines.

A representative characterization of the mean flow at the bottom tip, hub, and top tip heights in region I through out the wind farm is given in Fig. 6.5. From that figure it is clear that momentum recovery between the wind turbines is insufficient, especially in the case of $S_x = 5$. Velocity at the bottom and at the top tip heights shows much less variation. Mean flow appears to be more uniform directly upstream of each turbine in the case $S_x = 7$. Again, this effect remarks the importance of wind farm layout in the overall wind farm performance.

6.3.2 Turbulence intensity distribution

In general, turbulence intensity in the wake of a wind turbine, I_{wake} , comes from two main sources: the background turbulence, I_0 , and the wake added turbulence, I_+ . They are related in the following way:

$$I_{wake}^2 = I_0^2 + I_+^2 \quad (6.2)$$

Several empirical expressions have been proposed to estimate the added turbulence intensity I_+ (e.g., [83]; [48]; [35]). Recently, Chamorro and Porté-Agel [26] showed that the use of a single value to represent the wake-averaged added turbulence intensity is not sufficient due to its high spatial variability. In a simple attempt to include the non-axisymmetric effects, [26] propose to differentiate between a positive change (increase) I_+^+ , which occurs at the upper part of the wake, and a negative change (decrease) I_+^- in the lower part of the wake.

For a wind farm configuration where multiple turbine wakes coexist, Frandsen and Thøgersen [42] proposed a model that considers the wind farm layout. It is based on the geostrophic drag law and takes into account the additional ‘surface roughness’ generated by the turbines:

$$I_+ = \frac{1}{2} \left(I_0 + \sqrt{I_0^2 + I_{++}^2} \right), \quad (6.3)$$

where

$$I_{++} = \frac{0.36}{1 + 0.2\sqrt{s_1 s}/C_T}. \quad (6.4)$$

Here C_T is the thrust coefficient, s_1 and s are the inter-turbine spacings (normalized by the rotor diameter) within a row and between rows, respectively. The Frandsen and Thogersen [42] model applies above the hub height, and has become the European standard.

An alternative model, proposed by Wessel and Lange [106], assumes that the overall turbulence intensity at a particular location in the wind farm is given by:

$$I(x) = I_0 + \sqrt{\sum_{i=1}^N I_{+i}^2(x)}, \quad (6.5)$$

where N is the number of upwind turbines from the location of interest (x) and I_{+i} is the added turbulence intensity contribution of the i^{th} turbine at location x .

Although these models determine a unique representative value for the turbulence intensity in the wind farm, they show fundamental differences. The first approach assumes that turbulence levels do not change with the number of turbines in the wind farm, while the second approach assumes a monotonic increase with the downwind distance in the wind farm. The structural differences given by these approaches point out that, to date, there is no consensus model for the prediction of turbulence intensity inside wind farms ([20]).

Our results (Fig. 6.6) show that turbulence intensity significantly increases in the first three-four rows of wind turbines and, after the fifth row, it appears to reach a plateau, which differs from the Wessel and Lange [106] model (monotonically positive growth).

Significant differences on the spatial distribution of the turbulence intensity are observed behind a single wind turbine and far inside the wind farm. For instance, from

Fig. 6.6 an enhancement of roughly 50 % of turbulence intensity is observed between these two situations. Also, an increase of the turbulence levels at the bottom tip height is clearly observed inside the wind farm.

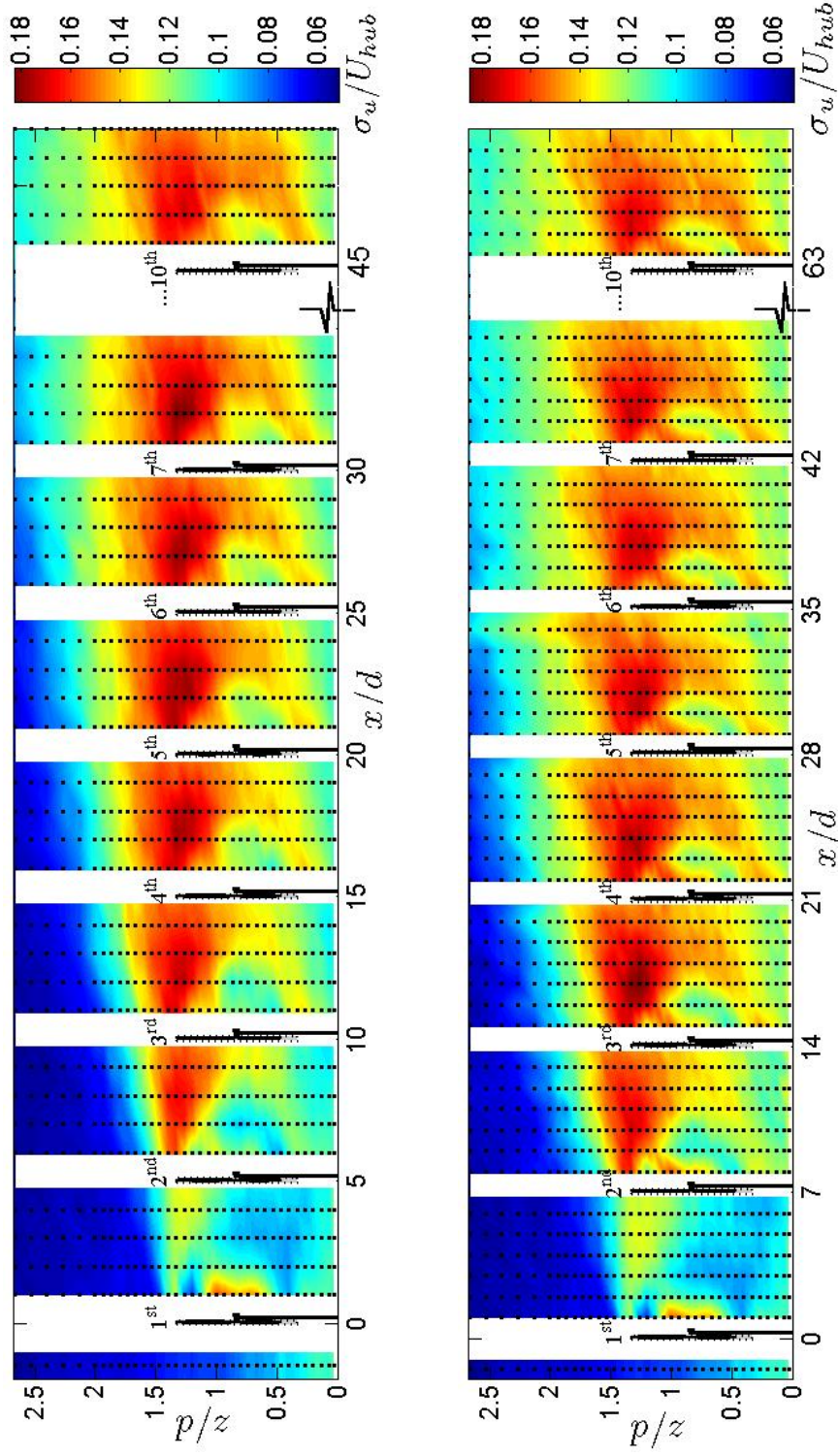


Figure 6.6: Turbulence intensity distribution around the wind farm. $S_x = 5$ (top) and $S_x = 7$ (bottom). Dots indicate measurement locations.

Figure 6.6 also shows that after the second row of wind turbines, the peak of turbulence intensity is consistently located near the top tip height at roughly three rotor diameters downwind of each turbine ($x/d \approx 3$). This peak is closer than that observed in a single wind turbine. Wind tunnel experiments performed by Chamorro and Porté-Agel [27] have shown that maximum values of turbulence intensity in the wake of a single wind turbine are located at a distance of 4 to 5.5 rotor diameters under neutral stratification.

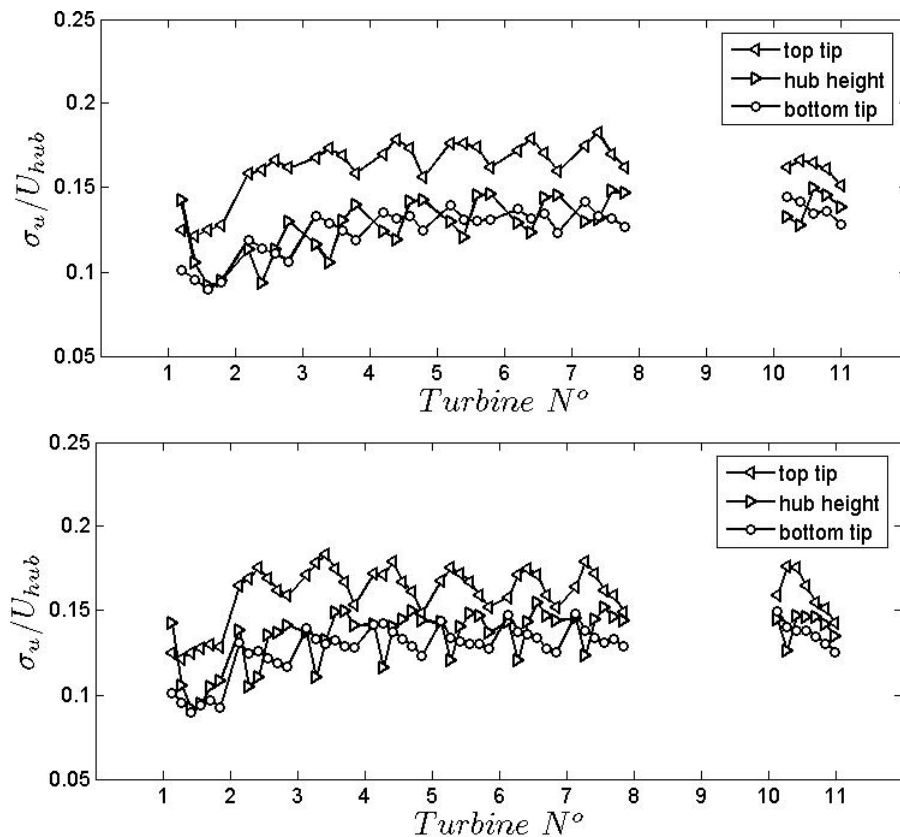


Figure 6.7: Turbulence intensity distribution in the wind farm at bottom, hub and top tip heights. $S_x = 5$ (top) and $S_x = 7$ (bottom).

The comparison of the two layouts ($S_x = 5$ and 7) reveals that the distribution of

turbulence intensity in the vicinity of each wind turbine depends also on the separation between turbines (S_x). Figure 6.7 shows the turbulence intensity at the bottom tip, hub, and top tip heights. It is clearly observed that in both cases local maximum of turbulence intensity is located around top tip with a peak at a relative distance of $x_i/d \approx 3$.

The gradual adjustment of the mean velocity observed in region II (see Fig. 6.2) is evident in the case of the turbulence intensity distribution depicted in Fig. 6.6. There, turbulence intensity gradually transitions to higher levels with downwind distance forming a clear layer with enhanced turbulence. This is expected since the wake expansion, above the top tip level, and the superposition of multiples wakes produces higher velocity fluctuations.

In order to appreciate the relative location of this layer, turbulence intensity is plotted in Fig. 6.8 at several heights (1.25H; 1.5H and 2H, where H is the turbine height) for the two layouts. From that figure, two distinct layers can be distinguished. One layer, an *internal boundary layer*, is modulated by the interaction between the wind farm and the incoming boundary layer flow. Within the other layer, an *equilibrium layer*, flow statistics are adjusted to the new conditions imposed by the wind turbines. A schematic of these layers is depicted in Fig. 6.9.

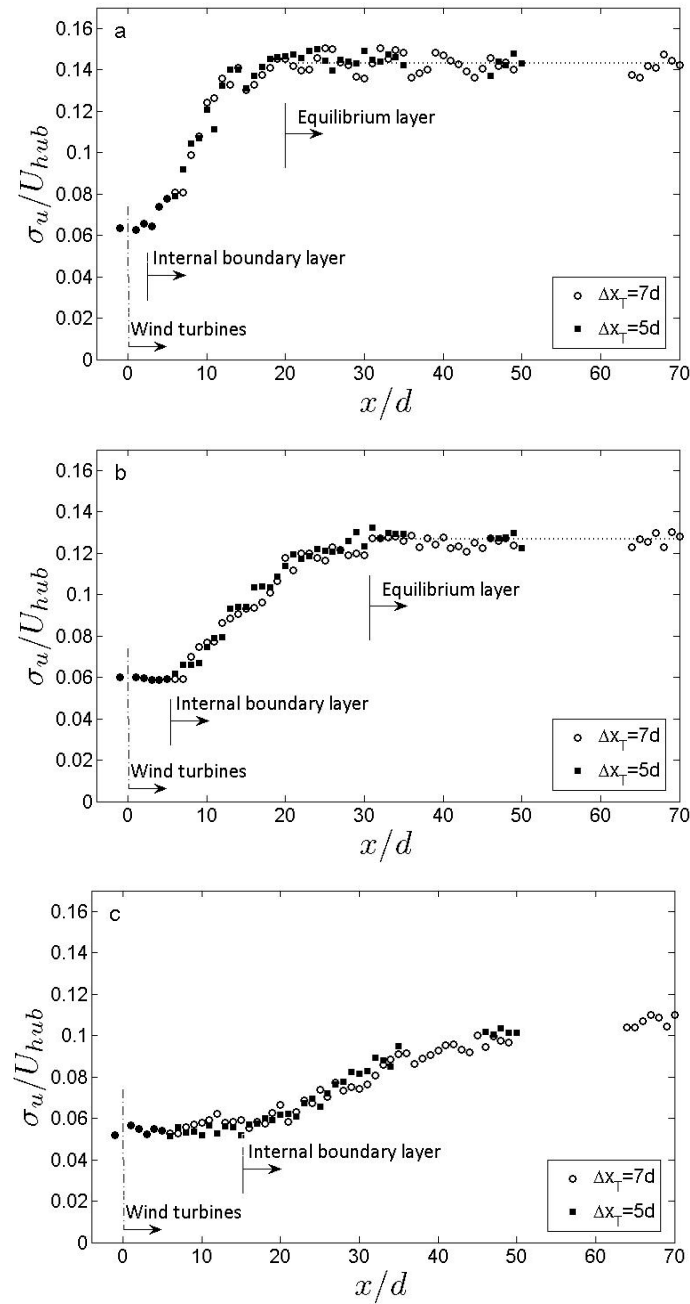


Figure 6.8: Turbulence intensity distribution at different heights above the wind farm. (a) $z = 1.25H$; (b) $z = 1.5H$; (c) $z = 2H$. H = turbine height.

These characteristic layers are always present in the atmospheric boundary layer after a surface roughness transition. Because velocity and turbulent fluxes are highly modified after a surface transition, accurate parameterizations are of special relevance in large scale models. Like the case of surface roughness transition, the clear existence of these two layers above a wind farm call for treatment as a roughness transition on a large scale perspective.

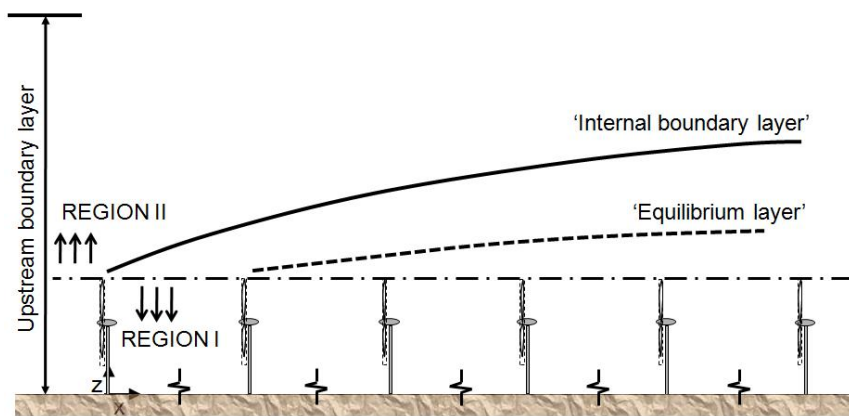


Figure 6.9: Conceptual description of the different regions and layers in a wind farm.

6.3.3 Other flow statistics

Spatial distribution of normalized kinematic shear stress, $-\overline{u'w'}/U_{hub}^2$, is shown in Fig. 6.10 for the case $S_x = 5$. An important enhancement of the turbulent stresses is observed up to roughly the fourth row of wind turbines. The enhancement of turbulent stresses is higher with respect to the case of a single turbine scenario (as observed between the first and second wind turbine). Similar to the case of the mean velocity and turbulence intensity, both an internal and equilibrium layer are observed in region II.

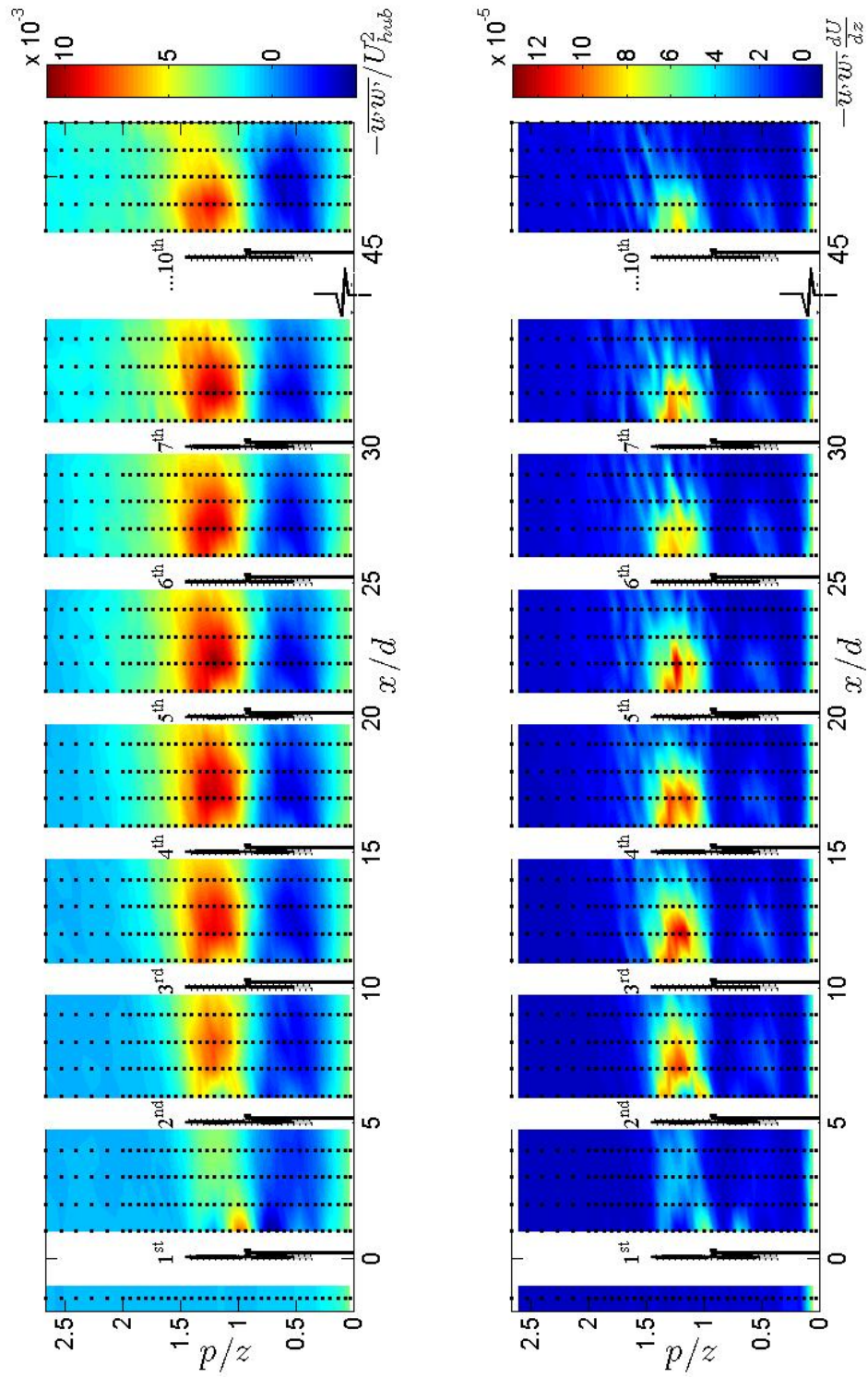


Figure 6.10: Non-dimensional distributions of kinematic shear stress (top) and turbulent kinetic energy production (bottom) inside and above a 10-turbines wind farm ($S_x = 5$).

Similar to the case of turbulence intensity (Fig. 6.8), Figure 6.11 shows the adjustment of kinematic shear stress in region II with distance at different heights. Both an internal boundary layer and an equilibrium layer are clearly observed.

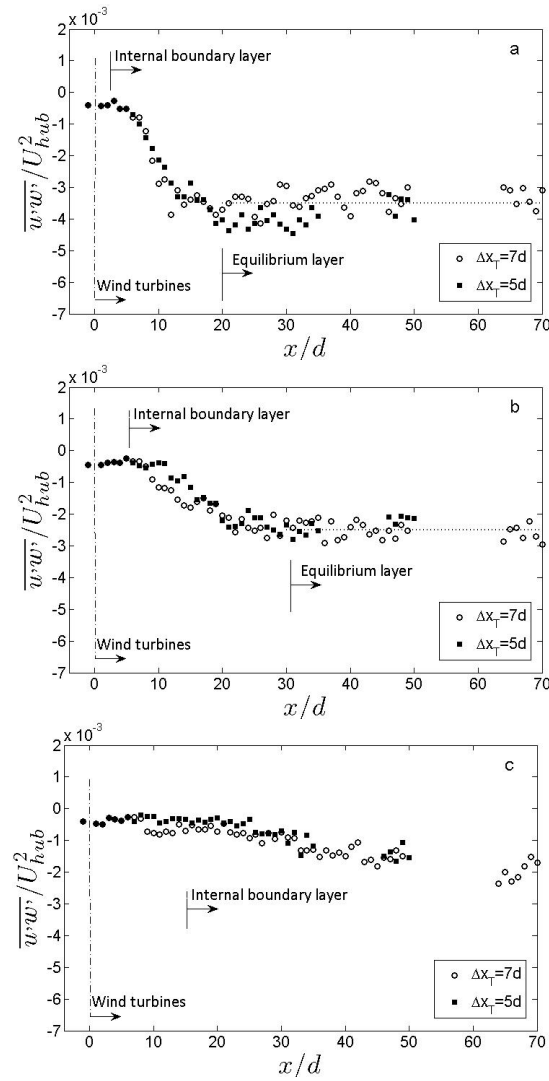


Figure 6.11: Non-dimensional distribution of kinematic shear stress at different heights above the wind farm. (a) $z = 1.25H$; (b) $z = 1.5H$; (c) $z = 2H$. H = turbine height.

Their specific locations, at a given height, agree with that observed in the turbulence

intensity. As expected, high levels of kinematic shear stress are observed closer to the wind turbine.

Areas of greater turbulence energy production ($-\overline{u'w'}\partial U/\partial z$ component) through the wind farm, shown in Fig. 6.10, are consistent with the enhanced levels of turbulence intensity observed above the hub height. Its maximum values are located between 1 – 3 rotor diameters downwind of each turbine.

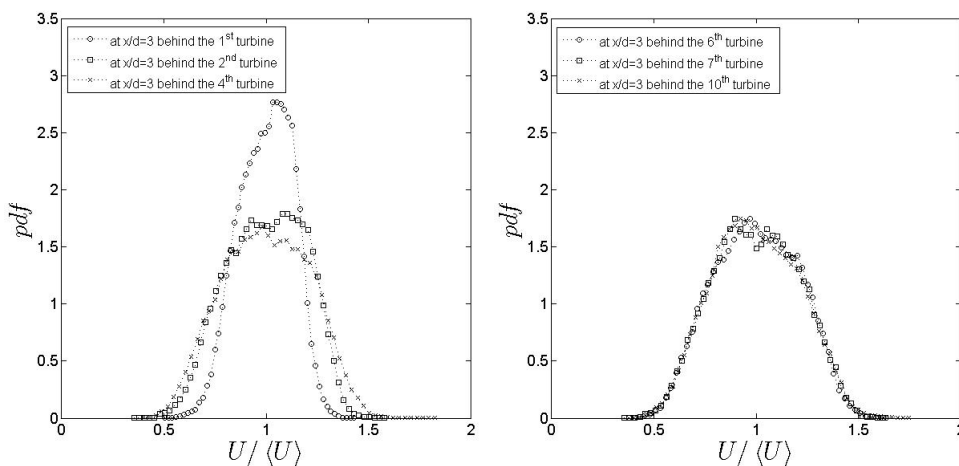


Figure 6.12: P.d.f. of streamwise velocity component at top tip height inside the wind farm ($S_x = 5$).

It is important to notice that the highest levels of turbulent energy production and turbulence intensity do not coincide with the location of the different wind turbines (which normally are 5 to 7 rotor diameters apart). Also, an enhancement of the turbulence energy production is observed also at the bottom tip height in the different wind turbines.

In general, turbulence characteristics at the turbine top tip height are of special relevance. It gives insights about the interaction between regions I and II. In particular, from the *pdf* of the streamwise velocity component at a relative distance $x_i/d = 3$ (Fig. 6.12) it is possible to see adjustment of the flow. It is noted that in the first four wind

turbines the velocity distribution is clearly not adjusted.

Power spectra of the streamwise and vertical velocity components reveal important effects of the flow turbulence on the turbine tip vortices (see Fig. 6.13). In particular, it is observed that behind the first wind turbine, where the background turbulence is relatively low, tip vortices induce a strong signature on the spectrum at a frequency coincident with that of the consecutive blades. Velocity spectrum of the vertical velocity component shows stronger effects of the tip vortices on the structure of the turbulence (see also [25]).

Far inside the wind farm, at a relative distance of $x_{10}/d = 1$ (i.e., behind the 10th wind turbine), it is possible to notice that due to the relatively high levels of velocity fluctuations inside the wind farm (case $S_x = 5$) tip vortices have negligible effects on the streamwise velocity component and minimum effects on the vertical velocity component. Nevertheless, the slightly lower turbulence levels around the turbines in the case of $S_x = 7$ produce non-negligible effects of the tip vortices on the power spectrum in both velocity components.

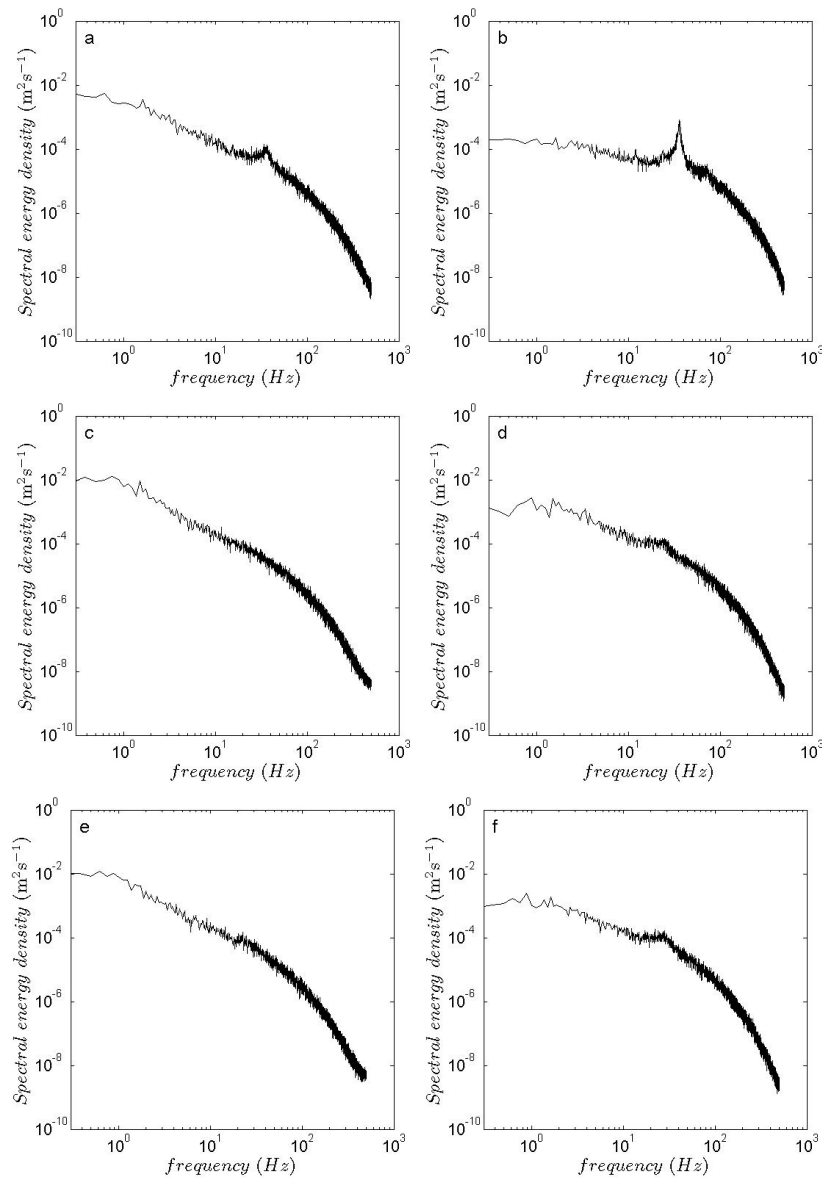


Figure 6.13: Power spectrum of the streamwise (u) and vertical (w) velocity components at top tip height inside the wind farm. (a) u -component at $x/d = 1$ behind the 1st turbine ($S_x = 5$); (b) w -component at $x/d = 1$ behind the 1st turbine; (c) u -component at $x/d = 1$ behind the 10th turbine ($S_x = 5$); (d) w -component at $x/d = 1$ behind the 10th turbine ($S_x = 5$); (e) u -component at $x/d = 1$ behind the 10th turbine ($S_x = 7$); (f) w -component at $x/d = 1$ behind the 10th turbine ($S_x = 7$).

6.3.4 On the wind farm roughness

The idea of representing a large wind farm as an added surface roughness to study local meteorology effects in large scale models has gained attention in the last decade (e.g.: [51]; [88]). From this perspective, and as a first approximation to the problem, wind turbines in a wind farm can be treated as localized roughness elements.

An early formulation to estimate the aerodynamic roughness length induced by evenly spaced obstacles of similar height and shape was proposed by Lettau [58]. It formulation states:

$$z_{0 \text{ obstacles}} = 0.5h^* \frac{s}{S}, \quad (6.6)$$

where h^* is the average vertical extent (or effective obstacle height), s is the area of the obstacle measured in the vertical crosswind-lateral plane and S is the horizontal area per obstacle.

The application of this formulation to the case of a large wind farm requires adjustments of the different terms. The characteristics constant (0.5) represents the average drag coefficient of a characteristic individual obstacle. From the actuator disc momentum theory (see [20]), that constant is $4a(1 - a)$ where a is the induction factor. The obstacle (wind turbine) area is $s = \pi d^2/4$ and $S = S_x S_y d^2$. Then, Lettau's formula for estimating the wind farm roughness can be written as:

$$z_{0T} = a(1 - a)h^* \frac{\pi}{S_x S_y}, \quad (6.7)$$

It is important to notice the coherent behaviour of Eq. 6.7. For instance, if the turbines are not in operation (i.e., no motion) their effect on the total roughness should be negligible, which is consistent with Eq. 6.7 by setting $a = 0$ (no motion) but not with the original formulation.

A combined roughness of the ground and a wind farm was proposed by Frandsen [40]. In that model

$$z_{00} = h \exp \left(- \frac{\kappa}{\sqrt{c_T + [\kappa / \ln (h/z_0)]^2}} \right) \quad (6.8)$$

where z_{00} is the surface roughness of the area of the wind turbine cluster, h is the turbine hub height, and $c_T = \pi C_T / (8s_x s_y)$, where C_T is the thrust coefficient.

In this experiment, the characteristic surface roughness of the model wind farm was obtained from the adjusted logarithmic region, i.e., starting from the sixth row of wind turbines. A schematic of the calculation is shown in Fig. 6.14. There a value of $z_0 = 3.6 \times 10^{-2}$ m was found for the case $S_x = 5$, which is roughly four times higher than that predicted by Eqns 6.7 and 6.8. The departure between the measured and predicted value of the wind farm's roughness highlights the intrinsic difficulties of its parameterization. In addition to this, wind farm layout is expected to affect the wind farm roughness.

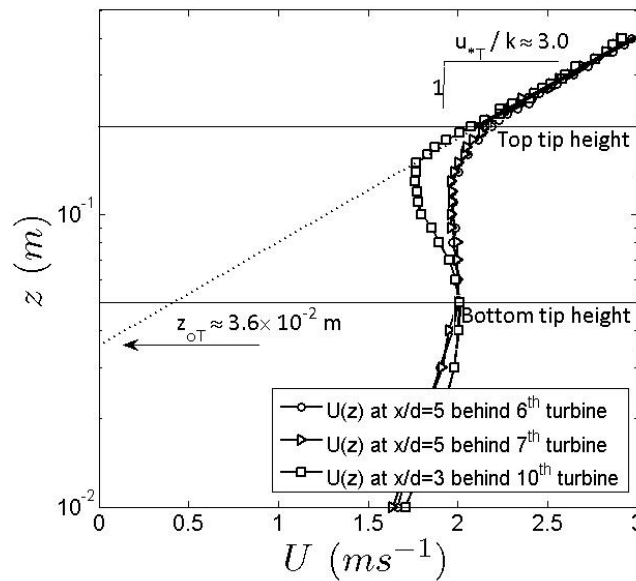


Figure 6.14: Aerodynamic roughness length of the wind farm array for the case $S_x = 5$.

6.4 Summary

Wind tunnel experiments were performed to study the flow characteristics inside and above a model wind farm composed of 10 by 3 miniature wind turbines placed in a boundary layer flow. Two layouts of aligned wind turbines were considered in this study. They consisted of inter-turbine separations of 5 and 7 rotor diameters in the streamwise direction by 4 rotor diameters in the spanwise direction. Cross-wire anemometry was used to obtain high resolution measurements of two velocity components (streamwise and vertical), turbulence intensity, and kinematic shear stress at different locations around the wind farm. Velocity spectra, turbulent energy production, and *pdf* were also calculated at various locations to better understand the spatial properties of the turbulent flow.

Overall results suggest that the turbulent flow can be characterized by two broad regions. The first is located below top tip height of the wind turbines. It has direct effect on the performance of the turbines. Turbulence statistics appear to reach equilibrium as close as the third to fourth row of wind turbines. In the second region, located directly above the first, flow statistics adjust slowly. In this region, two distinctive layers were found: an internal boundary layer and an equilibrium layer. In the former, both incoming flow and the wind turbines modulate the turbulence characteristic of the flow, while in the latter, flow statistics are conditioned mainly by the turbine dynamics. The distinctive characteristic of these two layers allows, from a large-scale perspective, the treatment of large wind farms as a special case of surface roughness transition. In that characterization, the determination of the representative roughness length and friction velocity associated with the wind farm is required. The determination of these parameters is not trivial. Indeed, the standard approach for their estimation is through the use of the log-law but its applicability is strictly valid under homogeneous conditions. Our results showed that a well-defined logarithmic velocity profile is reached only after the sixth-seventh row of wind turbines. Upwind of this location and similar to the

case of a surface roughness transition, flow transitions and the determination of those parameters is more complicated. In this experiment, a representative surface roughness length, obtained in the fully adjusted log region, was found to be greater than predicted by standard formulations.

Similar to the situation in the wake of a single wind turbine in a boundary layer flow (see Chamorro and Porté-Agel [26]), mean velocity distribution inside the farm did not follow a symmetric behaviour, but the mean velocity deficit ($\Delta U_x = U - U_{incoming}$) had a roughly symmetric structure between the bottom and top tip heights. This property allows, in principle, to generalize parameterizations of mean velocity inside a wind farm by accounting for the boundary layer effects on the mean flow.

Turbulence intensity in region I of the wind farm showed a non-symmetric structure. Like the case of a single wind turbine (Chamorro and Porté-Agel [27]), the boundary layer is responsible of this effect. A strong enhancement of the turbulence levels around the top tip levels was observed with respect to the turbulence generated behind a single wind turbine. The enhancement of the turbulence intensity appears to reach its highest levels behind the fourth turbine. This is a distinctive property since some formulations assume a monotonically positive behaviour of the turbulence levels with downwind distance in the farm. The peak of the velocity fluctuations are localized between 1 to 3 rotor diameters behind each turbine.

Power spectra of the streamwise and vertical velocity components showed a signature of the tip vortices on the turbulence structure in the wind farm for inter-turbine separation of seven rotor diameters ($S_x = 7$). On the other hand, the higher levels of turbulence present in the case of $S_x = 5$ precluded a noticeable signature of the tip vortices on the spectrum. This is consistent with the stronger signature of the turbine tip vortices observed behind the first wind turbine, for both velocity components, where the background turbulence is relatively low. In general, velocity spectrum of the vertical velocity component showed stronger effects of the tip vortices on the structure of the turbulence with respect to the streamwise velocity counterpart.

Chapter 7

Wind-turbine wake effects on the surface heat flux in a stable boundary layer

Wind tunnel experiments were performed to study the effect of wind turbine wakes on the surface heat flux distribution in a stably stratified boundary layer developed over a smooth surface. The stable boundary layer had a Reynolds number, based on the friction velocity, of $Re_\tau \approx 3.7 \times 10^4$ and a bulk Richardson number of $Ri_\delta = 0.17$. An array of heat flux sensors, mounted on the wind tunnel floor in a single spanwise row, were used to measure the average surface heat flux. The analysis looked at 3 cases: one with a single turbine, another with a simple array of 4 turbines placed in a single streamwise row, spaced 7 rotor diameter apart, and a case considering a 12 by 3 array of wind turbines aligned to the main direction of the flow, spaced 5 and 4 rotor diameters in the streamwise and spanwise directions, respectively.

Large changes in the local surface heat flux were found in all cases respect to the situation without turbine(s). In the single turbine scenario, local surface heat flux was increased by roughly 10% around the base of the wind turbine and reduced by

about 5% at 12 rotor diameters downwind of the wind turbine. Similar increases and reductions of surface heat flux were observed in the simple 4-turbine array case. In spite of these variations, the spatially averaged surface heat flux around the turbine(s) can be considered remains nearly unchanged. In contrast to the previous cases, the 12 by 3 wind turbine array showed a relevant reduction of 11% of the spatially-averaged mean surface heat flux in a representative area of the wind farm.

It is argued that the reduction of the flow velocity should imply a reduction of the heat flux, while the rotation of the wake should contribute to incrementing the heat flux due to mixing. These two effects lead to a low change in the overall surface heat flux in the first two cases. In addition to this, the interaction of the multiple wakes and the limited lateral transport imposed in the 12 by 3 array of turbines are responsible for the important reduction of surface heat flux measured in this case.

7.1 Introduction

Surface heat flux, among other factors, can modify the state of the boundary layer [97]. It plays an important role in the complex turbulent interactions present in the surface layer, modulating the mean and fluctuating characteristics of the flow (e.g. temperature, velocity, turbulent stresses and fluxes). A clear understanding of the driving forces and mechanisms that modulate the energy transfer between surface and the flow in the surface layer is of great importance in the development of improved subgrid-scale parameterizations for high resolution numerical models such large-eddy simulations (LES).

Of particular interest are the potential effects on the surface heat flux induced by wind turbine wake(s). As known, the wake of a wind turbine is a complex structure characterized by rotational motion induced by the turbine blades. Its longitudinal and radial pressure gradients, momentum reduction and enhancement of turbulence levels could alter the heat transfer in the surface around a turbine, especially if the wake

develops inside a boundary layer, where a non-axisymmetric behaviour is expected [26]. This phenomenon is particularly relevant in the context of wind farm parameterizations for large-scale numerical models. Usually, in these type of models the whole wind farm is treated as a region with enhanced roughness, the so called wind farm roughness [56, 10]. In addition to the importance of knowing the spatially averaged surface heat flux around a wind turbine (farm) scenario, the knowledge of the surface heat flux distribution is useful because it can help on the understanding of the interaction between the turbulent wake and surface.

In this paper, miniature wind turbines were placed in a wind tunnel under thermally stable conditions. Mean surface heat flux was measured around a single wind turbine, around a simple 4-turbine array placed in a streamwise row and around the center turbine of the 11th row of a 12 by 3 array of aligned wind turbines. The wind tunnel experimental set-up is described in section 7.2. In section 7.3, surface heat flux measurements are presented and discussed. Finally, a summary is given in section 7.4.

7.2 Experimental setup

The Saint Anthony Falls boundary layer wind tunnel has a plan length of 37.5 m, with a main test section fetch of 16 m and a cross section of 1.7 m \times 1.7 m. There is a contraction with a 6.6:1 area ratio upwind of the test section along with flow conditioning and turbulence control consisting of a coarse wire mesh and honeycomb flow-strengtheners. The tunnel is operated as a closed-return loop. Turbulence intensity in the free stream of the wind tunnel is approximately 0.25% for a 10 m s⁻¹ freestream velocity. More details on the wind tunnel can be found in Carper and Porté-Agel [23]. Nine meters of the test section floor are constructed of flat plate aluminium heat exchangers (0.3 m length and 25.4 mm thick through which a chilled solution of 30% ethylene glycol, 70% water solution is circulated) that can be thermally controlled from 5°C to 60°C \pm 0.1°C. A heat exchanger mounted in the expansion after the fan

can control the free-stream air from 10°C to $60^{\circ}\text{C} \pm 0.2^{\circ}\text{C}$. Electronic valves monitored by an automatic controller allow the temperature conditions to reach precise values for both air flow and surface temperatures.

A turbulent boundary layer was developed with the help of a tripping mechanism (40 mm picket fence) located at the exit of the wind tunnel contraction, where the test section begins. The turbulent boundary layer was allowed to grow in zero pressure gradient conditions by adjustment of the wind tunnel ceiling.

To characterize the turbulent flow, a customized 3-wire sensor (a combination of a x-type hotwire and a single cold-wire) was used to obtain high resolution measurement of 2-velocity components and temperature. The x-wire data was corrected point-by-point for temperature fluctuations with data collected simultaneously with the cold wire. Calibration of the 3-wire sensor was performed at the beginning of each experimental run in a calibration unit, against a Pitot-static probe (for mean velocity) and a thermocouple (for mean temperature), considering seven sensor inclination angles, seven wind velocities at each position and four different mean free stream temperatures.

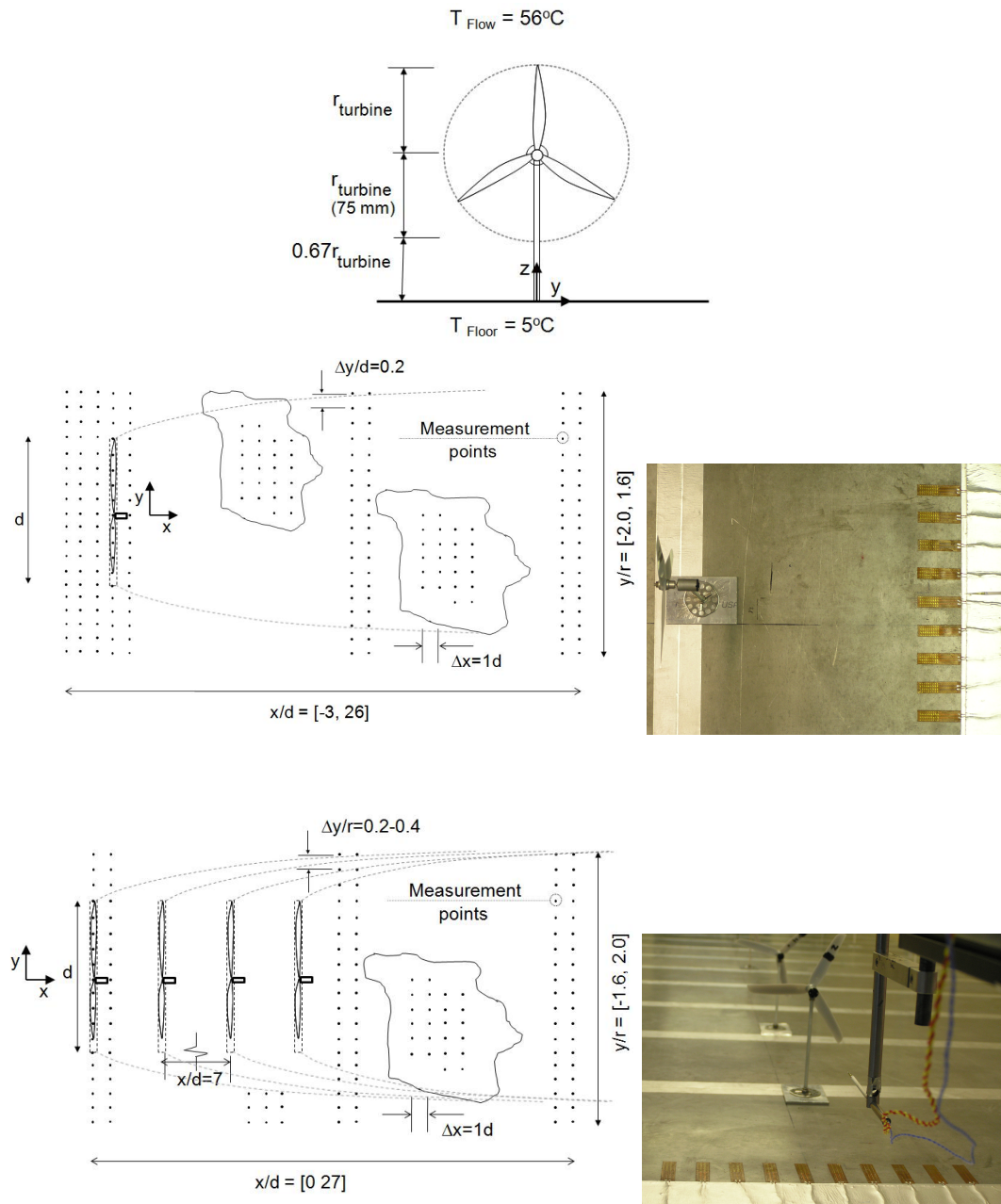


Figure 7.1: Experimental set-up for the single wind turbine and the 4-aligned wind turbine array cases. Wind turbine dimensions (top), measurement locations and photograph of the single wind turbine (middle) and its counterpart for the 4-turbine case (bottom).

A combination of cubic-spline table calibration method was then used to determine the two instantaneous velocity components and temperature. For more details on the calibration procedure, see Bruun [18]. The probe is made of $2.5 \mu\text{m}$ (see [105]) tungsten wires that are connected to an A.A. Lab Systems AN-1003 10-channel CTA system. During the calibration and measurements, the temperature fluctuations were kept within a $\pm 0.2^\circ\text{C}$ range to avoid bias errors due to thermal drift of the voltage signal.

Surface heat flux was measured using two types of sensors. RdF-Micro-Foil heat flux sensors (Model 27160) were considered for the single and 4-turbine cases. Each of these sensors has an effective area of $11.8 \times 25.4 \text{ mm}^2$ and a thickness of 0.1 mm. It consists of a polyimide membrane in which a thermocouple array is embedded. Heat passing through the sensor produces a slight temperature difference across the membrane that is translated to a voltage output by the thermocouple array. The voltage signal is proportional to the heat flux. Because the sensor is extremely thin, the temperature drop across the sensor is very small, thus having a minimal effect on the surface heat flux at the measurement area. Ten heat flux sensors were mounted on one of the flat plate heat exchangers in a single array perpendicular to the main direction of the flow, with 3 cm spacing. In order to obtain detailed measurements in both spanwise and streamwise directions, the model wind turbine(s) were moved in those directions resulting in measurement of surface heat flux at different locations relative to the turbine model(s). In the single turbine scenario, data was collected at $x/d = -3, -2, -1, 0, 1, \dots, 8, 10, 12, \dots, 22$ and 26, in the streamwise direction and $y/d = [-2.0, 1.6]$ in $0.2y/d$ increment in the spanwise direction. In the case of the simple 4-turbine array, the same spanwise sensor disposition was used but measurements were taken at relative distances of $x/d = 1, 2, 3, 4, 5$ behind every turbine in the main direction of the flow. (see Figure 7.1). The case of a 12 by 3 wind turbine array considered 19 sensors (RdF-Micro-Foil number 27133-3, effective area of $7 \times 10 \text{ mm}^2$) placed perpendicularly to the direction of the flow in 1 cm separation. Measurements were performed around the center turbine of the 11th row. The representative area of the turbine was defined from -2.5 to 2.5 rotor diameters

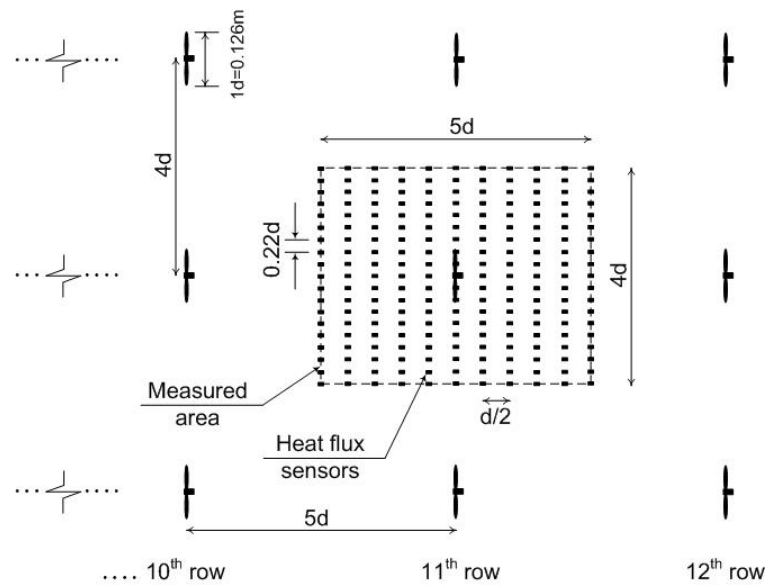
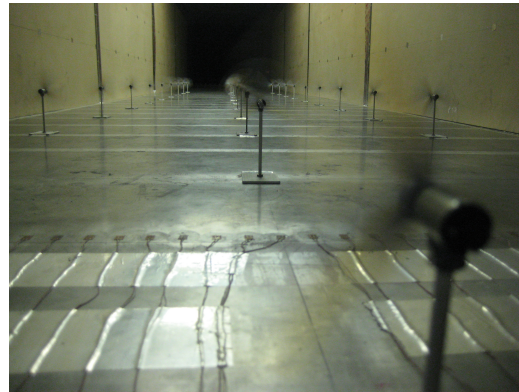


Figure 7.2: Experimental set-up for the 12 by 3 wind turbine array. Photograph of the model wind farm (top) and measurement locations (bottom).

in the streamwise direction, and -2 to 2 rotor diameters in the spanwise direction (see Figure 7.2).

The model wind turbine consists of a three-blade GWS/EP-6030x3 rotor attached to a small DC generator. The turbine angular velocity can be adjusted by changing the resistance of the generator. During the experiments, the tip speed ratio (blade tip velocity versus the wind velocity at hub height) of the first wind turbine was approximately $\lambda = 2\pi r\Omega/[60U_{hub}] = 4.0$. Ω is the angular velocity of the turbine measured in rpm and U_{hub} is the mean velocity at the hub height. Similar wind turbines were used by Chamorro and Porté-Agel [26] to study boundary layer effects on the turbulence structure of wind-turbine wakes. Figure 7.3 shows the relative angular velocity of the different turbines respect to the first one. Similar turbines but slightly smaller (84% size) were used in the wind farm scenario.

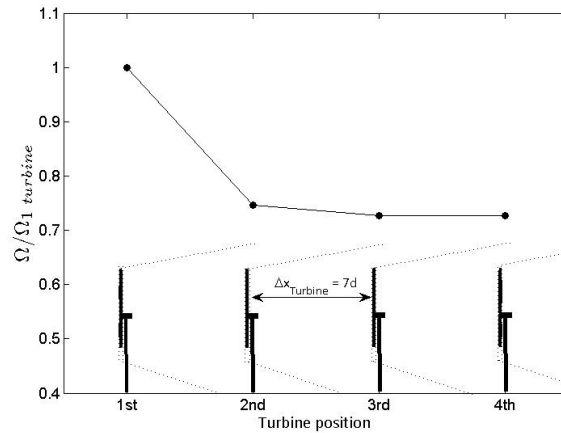


Figure 7.3: Angular velocity of the different turbines for the simple 4-turbine array normalized with respect to the first turbine.

The experiments were conducted with a free stream velocity of 2.25 m s^{-1} for the single turbine case, 2.65 m s^{-1} for the 4-turbine array and 3.2 m s^{-1} for the 12 by 3 wind turbine array. A turbulent boundary layer depth of $\delta \approx 0.5\text{ m}$ was obtained

at the turbine location(s) and the stratification in the boundary layer was created by cooling the floor at a temperature of 5°C and heating the wind tunnel air flow at 56°C . Based on this configuration the stable boundary layer had a Bulk Richardson number Ri_{δ} ($= g\delta\Delta\Theta/(\Theta_0U_{\infty}^2)$) of 0.17, 0.12 and 0.09 for the single turbine, 4-turbine and 12 by 3 array, respectively. A Reynolds number, based on the friction velocity, of $Re_{\nu} \approx 3.7 \times 10^4$, and a friction velocity of $u_* = 0.116 \text{ ms}^{-1}$ (for 2.25 m s^{-1}). The aerodynamic roughness length was found to be $z_0 = 0.05 \text{ mm}$. Figure 7.4 shows the vertical profiles of the mean velocity, turbulent heat flux and kinematic shear stress measured in the stable boundary layer.

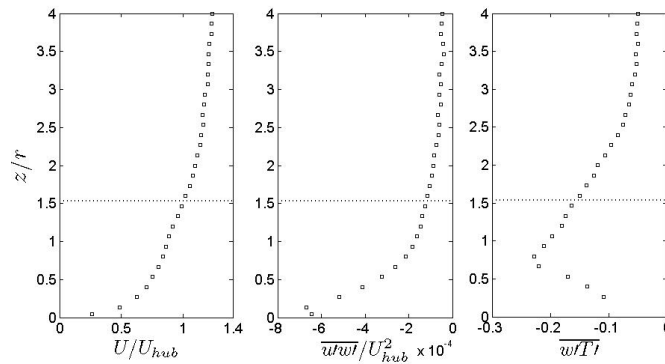


Figure 7.4: Background characteristics of the incoming turbulent boundary layer: normalized mean velocity (left), kinematic shear stress (middle) and turbulent heat flux (right). The horizontal lines represent the turbine axis. Height is normalized with the turbine radius r .

7.3 Spatial distribution of Surface heat flux

7.3.1 Case of single turbine and simple 4-turbine array

A complete explanation of the variations of the convective heat flux observed in this experiment is beyond the scope of this paper. However, the mechanism of convective

heat flux from a smooth flat plate in a turbulent boundary layer can be explained as follows.

The convective heat transfer starts at the surface of the flat plate where heat flows by conduction through the very thin viscous sublayer. The driving force for the conductive heat flux through this thin layer of air is the temperature gradient at the surface of the wall. Temperature of the freestream air, and turbulent mixing above the viscous sublayer are responsible for the temperature gradient.

A detailed characterization of the surface heat flux (Q) around a single wind turbine, normalized with respect to the surface heat flux without a turbine (Q_0), is shown in Figure 7.5. From that figure, it is clear that the wind turbine has an effect on the surface heat flux. Around the turbine base, in the region contained roughly between $x/d \in [-1, 3]$ and $y/d \in [-1, 1]$, the non-dimensional surface heat flux Q/Q_0 is enhanced, reaching a maximum value of approximately $Q/Q_0|_{max} \approx 1.13$ (as shown clearly in Figure 7.6). We argue that the air approaching the turbine, deflected by the turbine 'disc', is the cause of such an enhancement. Because of this, warmer air higher in the boundary layer is forced beneath the turbine disc with an increased velocity. The higher temperature air tends to increase the temperature gradient at the cooler floor as would the higher velocity air by means of an increase in the turbulent mixing directly above the floor.

Outside this region, surface heat flux is slightly reduced with respect to the no-turbine situation. It is observed that the surface heat flux reaches a minimum of $Q/Q_0 = 0.95$ at a distance of $x/d \approx 12$. Due to the complex interaction of the wake with the surface, several competing effects co-exists. For instance the velocity deficit, which does not exist in the no-turbine situation, tends to decrease the heat flux. However, a tendency for an increase also is present due to an enhancement of both turbulent intensity and temperature near the surface due to mixing caused by the rotating flow of the wake, which carries hotter air down to the surface. These two opposing effects, in the end, lead to a reduction of surface heat flux at locations starting from the point where

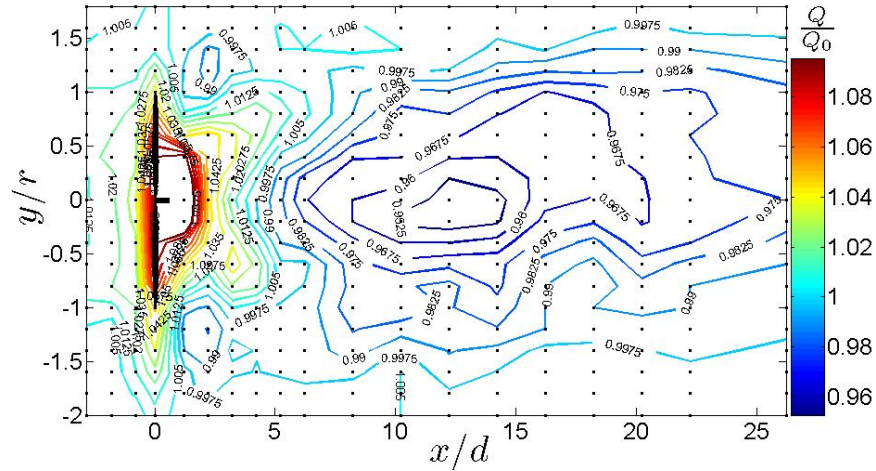


Figure 7.5: Spatial distribution of non-dimensional surface heat flux around a wind turbine placed in a stably stratified boundary layer over a smooth surface.

the wake touches the surface ($x/\delta \geq 5$). Figure 7.7 shows these concepts graphically.

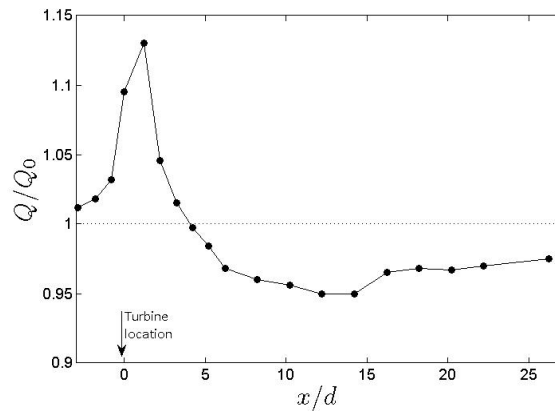


Figure 7.6: Non-dimensional surface heat flux distribution around a single wind turbine at zero span ($y = 0$).

Within the conceptual characterization of the different mechanisms acting on the surface heat transfer process, the contribution (positive or negative) of surface heat flux

due to a change in flow velocity (ΔQ_v) and the contribution induced by the rotating wake in the temperature mixing (ΔQ_Ω) is also included. As depicted in that figure, close to the turbine (in the near wake region) the flow velocity increases, implying that the non-dimensional surface heat flux $Q(x)/Q_0 = 1 + \Delta Q_v/Q_0 > 1$. At locations where the turbine wake interacts with the surface (roughly in the far wake region), the non-dimensional surface heat flux may be determined by $Q(x)/Q_0 = 1 + \Delta Q_v/Q_0 + \Delta Q_\Omega/Q_0$. As indicated before, the two contributions, $\Delta Q_v/Q_0$ and $\Delta Q_\Omega/Q_0$, have different sign but the velocity-based term is dominant (as inferred from Figure 7.5). It is important to notice that surface heat flux was affected even at a distance of $x/d = 26$ in the downwind direction, but the net effect of the wind turbine on the overall mean surface heat flux was nearly unchanged (compared to the base case) over the disturbed area defined in Figure 7.5.

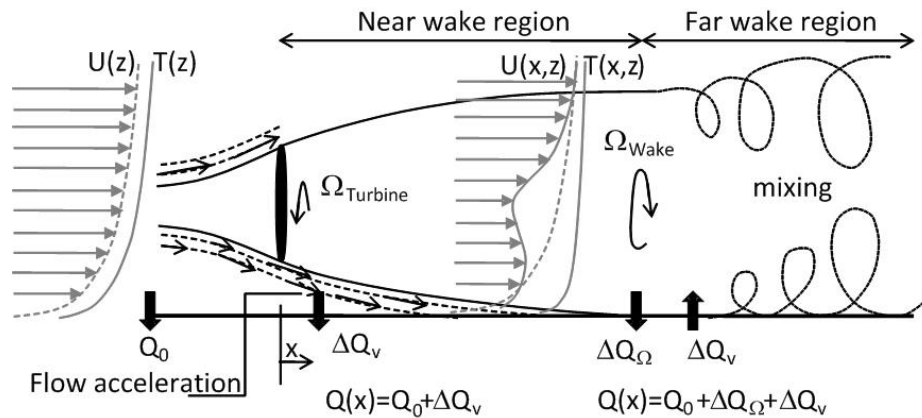


Figure 7.7: Conceptual schematic of a wind turbine wake with the different mechanisms affecting surface heat flux distribution.

Under the same conditions given for the case of a single turbine (surface roughness and stratification), Figure 7.8 shows the non-dimensional surface heat flux distribution around the simple array of four aligned wind turbines spaced seven turbine diameters from each other. From that figure, it is clear that surface heat flux is dependent on the

relative location in the wind turbine array, i.e., it transitions to a particular equilibrium. Between the first and second wind turbines surface heat flux distribution has nearly the same structure as the single turbine case. Nevertheless, after the second turbine, a reduction of the surface heat flux is observed between subsequent turbines (locations of $x_i/d \in [1.5, 4]$, where x_i is measured from the i^{th} turbine). This reduction appears to stabilize after the third turbine, as indicated in the particular case of Figure 7.9, which shows the non-dimensional surface heat flux distribution at the center line ($y = 0$).

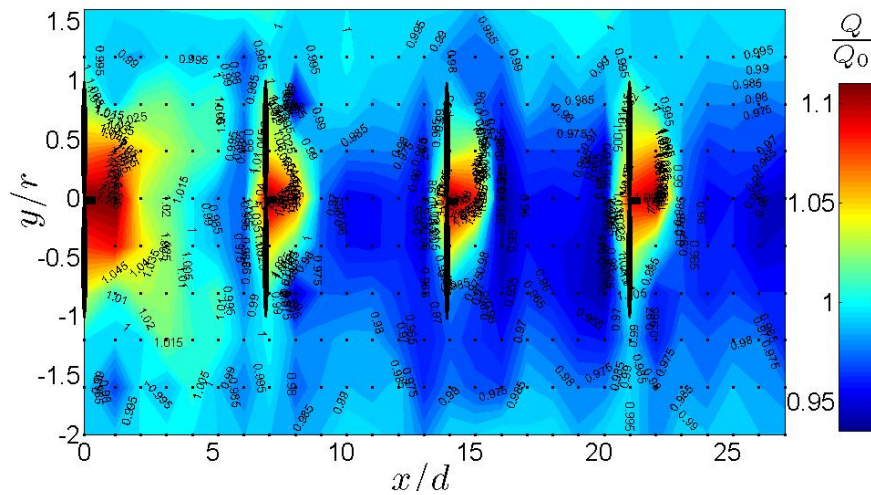


Figure 7.8: Spatial distribution of non-dimensional surface heat flux around a simple array of four aligned wind turbines placed in a stably stratified boundary layer over a smooth surface.

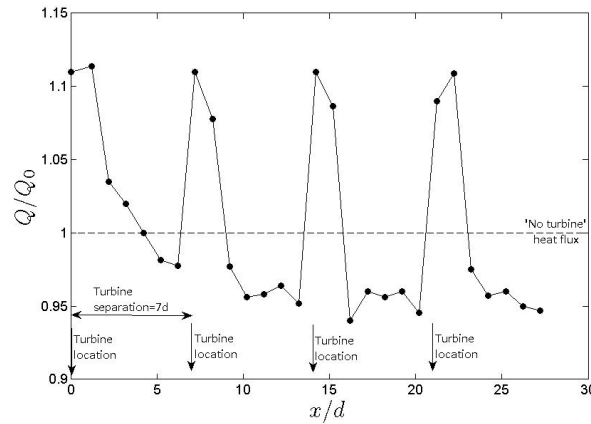


Figure 7.9: Non-dimensional surface heat flux distribution around the 4-turbine array at zero span ($y=0$).

Like in the single turbine scenario, an increase in surface heat flux around each turbine is observed but, in this case, the increment is confined in a smaller area. This is expected since consecutive wind turbines are affected by one or multiple wakes. Similar to the single turbine case, the spatially averaged surface heat flux (of Fig. 7.8) under this configuration is reduced by (only) approximately 1%.

7.3.2 Case of 12 by 3 wind turbine array

Although the spatially averaged surface heat flux for the previous cases (single and 1-d array of 4-wind turbines) was found to be nearly unchanged, an important reduction is hypothesized for the case of a large wind farm. In this case, lateral transport is negligible and only vertical transport is expected to play a major role, which would lead to a non-negligible reduction of the surface heat flux.

Surface heat flux measurements around a wind turbine placed in the 11th row of the wind farm (see Figure 7.2) show that this quantity is highly affected by the presence of the wind farm. The complex interaction of multiple turbine wakes with the surface and the reduction of the lateral transport are responsible, in this case, for the overall

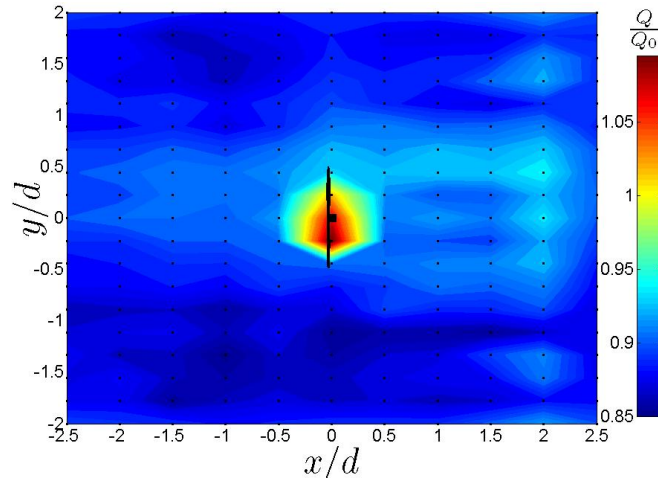


Figure 7.10: Non-dimensional surface heat flux distribution of a single turbine in the wind farm.

surface heat flux change. Figure 7.10 shows a two dimensional representation of the normalized surface heat flux within the unit area of the selected wind turbine. The spatial average was found to be $1/A \int Q/Q_0 dA = 0.89$, i.e., a net reduction of 11%. Similar to the other two cases, an enhancement of surface heat flux around the base of the wind turbine is also observed, although this is lower than the other cases (approx. 7%). A local enhancement of velocity with warmer air should induce this effect.

7.3.3 Summary

A wind tunnel experiment was performed to study the potential effects of wind turbine wake(s) on the surface heat flux in thermally stable conditions. Three cases were studied: one with a single wind turbine, another with a 1-d array of 4 turbines placed in a single streamwise row, spaced 7 rotor diameters apart, and a case of 12 by 3 aligned wind turbines spaced 5 and 4 rotor diameters in its streamwise and spanwise directions, respectively. A series of surface heat flux sensors, placed perpendicular to the main direction of the floor, were used to obtain the spatial distribution of surface heat flux

around the turbine(s).

Results showed that wind turbine wakes effectively alter the surface heat flux. In the single turbine case, an increment of roughly 10% was found around the base of the turbine. In contrast, a reduction was observed starting a distance of $x/d \geq 5$, location where the wake touches the surface. This reduction persisted even at distances of $x/d = 26$, reaching a minimum of approximately 5% at a distance of $x/d = 12$. It is argued that flow deflected by the turbine 'disc' is responsible for the enhancement of the surface heat flux around the base of the turbine. Warmer air, higher in the boundary layer, is forced beneath the turbine increasing the temperature gradient. At locations where turbine wake touches the surface, reduced flow velocity and wake rotation (mixing) are two factors that affect the heat flux at the surface.

In the simple 4-turbine array configuration, a similar increment of surface heat flux was found close to the turbines, although it was confined to a smaller area. Measurements show that surface heat flux distribution reached roughly an equilibrium after the third wind turbine.

Even though in the single and the 4-turbine cases the surface heat flux distribution was affected, with departures ranging between -5% and $+10\%$, its spatial average can be considered unchanged (negligible in the single turbine case and roughly 1% in the 4-turbine array when considered the area given in the representative set-up).

A different situation was observed in the 12 by 3 wind turbine array. Mean surface heat flux was found to be reduced by approximately 11%. It is argued that the interaction between the surface and the superimposed turbine wakes, in addition to the limited lateral transport, are responsible for that reduction.

Additional work is required to better understand these processes. Large wind farms with different layout and different thermal stability will be studied to compliment the result obtained here.

Bibliography

- [1] J. Ainslie. Calculating the flowfield in the wake of wind turbines. *J Wind Eng Ind Aerodyn*, 27:213–224, 1988.
- [2] J. D. Albertson and M. B. Parlange. Surfaces length scales and shear stress: implications for land-atmosphere interactions over complex terrain. *Water Resources Res.*, 35:2121–2132, 1999.
- [3] P. Albertson, A. V. Johansson, J. H. Haritonidis, and H. Eckelmann. The fluctuating wall-shear stress and the velocity field in the viscous sublayer. *Phys. Fluids*, 31:1026–1033, 1988.
- [4] P. H. Alfredsson, J. A. V., J. H. Haritonidis, and H. Eckelmann. The fluctuating wall-shear stress and the velocity field in the viscous sublayer. *Phys. Fluids*, 31:1026–1033, 1988.
- [5] R. A. Antonia and R. E. Luxton. The response of a turbulent boundary layer to a step change in surface roughness. *J. Fluid Mech.*, 53:737–757, 1972.
- [6] C. Archer and M. Jacobson. Spatial and temporal distributions of u.s. winds and wind power at 80 m derived from measurements. *J. Geophys. Res.*, 108:1–20, 2003.
- [7] S. Arya. Structure of stable stratified turbulent boundary layer. 00:000–000, 1968.
- [8] S. Arya. Introduction to micrometeorology. *Academic Press*, page 420, 2001.

- [9] R. Avissar and T. Schmidt. An evaluation of the scale at which ground-surface heat flux patchiness affects the convective boundary layer using large-eddy simulations. *J. Atmos. Sci.*, 55:2666–2689, 1998.
- [10] P. S. Baidya, R. and R. Walko. Can large wind farms affect local meteorology? *J. Geophys. Res.*, 109:No. D19 D19101, 2004.
- [11] R. Barthelmie, K. Hansen, T. Frandsen, O. Rathmann, J. Schepers, W. Schlez, J. Phillips, K. Rados, A. Zervos, E. Politis, and P. Chaviaropoulos. Modelling and measuring flow and wind turbine wakes in large wind farms offshore. *Wind Energy*, 12:431–444, 2009.
- [12] R. Barthelmie, G. Larsen, S. Pryor, H. Jorgensen, H. Bergstrom, W. Schlez, K. Rados, B. Lange, P. Volund, S. Neckelmann, S. Mogensen, G. Schepers, T. Hegberg, L. Folkerts, and M. Magnusson. Endow (efficient development of offshore wind farms): Modelling wake and boundary layer interactions. *Wind Energy*, 7:225–245, 2004.
- [13] L. Binh, T. Ishihara, P. Van Phuc, and Y. Fujino. A peak factor for non-gaussian response analysis of wind turbine tower. *J Wind Eng Ind Aerodyn*, 96:2217–2227, 2008.
- [14] E. Bou-Zeid, C. Meneveau, and M. Parlange. Large-eddy simulation of neutral atmospheric boundary layer flow over heterogeneous surfaces: Blending height and effective surface roughness. *Water Resources Res.*, 40:1–18, 2004.
- [15] E. Bou-Zeid, C. Meneveau, and M. Parlange. A scale-dependent lagrangian dynamic model for large eddy simulation of complex turbulent flows. *Phys. Fluids*, 17, 2005. 025105.

- [16] E. F. Bradley. A micrometeorological study of the velocity profiles and surface drag in the region modified by a change in surface roughness. *Q. J. R. Meteorol. Soc.*, 94:361–379, 1968.
- [17] G. L. Brown and A. S. Thomas. Large structure in a turbulent boundary layer. *Phys. Fluids*, 20:243–252, 1977.
- [18] H. H. Bruun. Hotwire anemometry, principles and signal analysis. 1995. *Oxford Univ. Press*, U.K. 507 pp.
- [19] T. Burton, D. Sharpe, N. Jenkins, and E. Bossanyi, editors. *Wind energy handbook*. John Wiley and Sons, Ltd, Chichester, 1st edition, 1995.
- [20] T. Burton, D. Sharpe, N. Jenkins, and E. Bossanyi, editors. *Wind energy handbook*. John Wiley and Sons, Ltd, Chichester, 1st edition, 1995.
- [21] P. Carlin. A suggested modification to a common expression for the energy content of a wind data sample. *Wind Energy*, 8:477–480, 2005.
- [22] M. Carper and F. Porté-Agel. The role of coherent structures in subfilter-scale dissipation of turbulence measured in the atmospheric surface layer. *J. of Turbul.*, 5(40), 2004. DOI:10.1088/1468-5248/5/1/040.
- [23] M. Carper and F. Porte-Agel. Subfilter-scale fluxes over a surface roughness transition. part i: Measured fluxes and energy transfer rates. *Boundary-Layer Meteorol.*, 126:157–179, 2008.
- [24] I. P. Castro, H. Cheng, and R. Reynolds. Turbulence over urban-type roughness: Deductions from wind-tunnel measurements. *Boundary-Layer Meteorol.*, 118:109–131, 2006.
- [25] L. P. Chamorro and F. Porté-Agel. Velocity and surface shear stress distributions behind a rough-to-smooth surface transition: a simple new model. *Boundary-Layer Meteorol.*, 130:29–41, 2009.

- [26] L. P. Chamorro and F. Porté-Agel. A wind-tunnel investigation of wind-turbine wakes: boundary-layer turbulence effects. *Boundary-Layer Meteorol.*, 132:129–149, 2009.
- [27] L. P. Chamorro and F. Porté-Agel. Effects of thermal stability and incoming boundary-layer flow characteristics on wind-turbine wakes: A wind-tunnel study. *Boundary-Layer Meteorol.*, 136:515–533, 2010.
- [28] L. P. Chamorro and F. Porté-Agel. Wind-tunnel study of surface boundary conditions for large-eddy simulation of turbulent flow past a rough-to-smooth surface transition. *J. of Turbul.*, 10(1):1–17, 2010.
- [29] L. P. Chamorro, J. Tucker, and F. Porté-Agel. Wind turbine wake effects on the surface heat flux in stable boundary layer. *Renewable Energy*, To be submitted:., 2010.
- [30] F. Chaudhry and R. Meroney. A laboratory study of diffusion in stably stratified flow. *Atmos. Environ.*, 7:443–454, 1973.
- [31] H. Cheng and I. P. Castro. Near-wall flow development after a step change in surface roughness. *Boundary-Layer Meteorol.*, 105:411–432, 2002.
- [32] Y. T. Chew, B. C. Khoo, and L. G. L. An investigation of wall effects on hotwire measurements using a bent sublayer probe. *Meas. Sci. Tech.*, 9:67–85, 1998.
- [33] M. Claussen. Area-averaging of surface fluxes in a neutrally stratified, horizontally inhomogeneous atmospheric boundary layer. *Atmos. Environ.*, 24A(6):1349–1360, 1990.
- [34] G. Corten and P. Schaak. Velocity profiles measured above a scaled wind farm. 2004. European wind energy conference, London, U.K.
- [35] A. Crespo and J. Hernandez. Turbulence characteristics in wind turbine wakes. *J Wind Eng Ind Aerodyn*, 61:71–85, 1996.

- [36] A. Crespo, J. Hernandez, and S. Frandsen. Survey of modelling methods for wind turbine wakes and wind farms. *Wind Energy*, 2:1–24, 1999.
- [37] S. Derbyshire. Nieuwstadt’s stable boundary layer revisited. 116:127–158, 1990.
- [38] W. P. Elliott. The growth of the atmospheric internal boundary layer. *Trans. Amer. Geophys. Union.*, 39:1048–1054, 1958.
- [39] S. Frandsen. On the wind speed reduction in the center of large cluster of wind turbines. *J Wind Eng Ind Aerodyn*, 39:251–265, 1992.
- [40] S. Frandsen. Turbulence and turbulence-generated fatigue loading in wind turbine clusters. *Wind energy department, Risø National Laboratory, Roskilde, Denmark.*, 2003.
- [41] S. Frandsen, R. Barthelmie, S. Pryor, O. Rathmann, S. Larsen, and J. Hojstrup. Analytical modelling of wind speed deficit in large offshore wind farms. *Wind Energy*, 9:39–53, 2006.
- [42] S. Frandsen and M. Thogersen. Integrated fatigue loading for wind turbines in wind farms by combining ambient turbulence and wakes. *J Wind Engin*, 23:327–339, 1999.
- [43] J. R. Garratt. The internal boundary layer-a review. *Boundary-Layer Meteorol.*, 50:171–203, 1990.
- [44] J. R. Garratt. The atmospheric boundary layer. 1992. *Cambridge Univ. Press*, U.K.
- [45] G. Grotzbach. Direct numerical and large eddy simulations of turbulent channel flows. *Encyclopedia of Fluid Mechanics.*, 6:1337–1391, 1987.

- [46] M. Grubb and N. Meyer. Wind energy: Resources, systems and regional strategies. 1993. in *Renewable Energy*. Edited by T.B. Johansson et al, pp. 157-212. Island Press, Washington, D.C.
- [47] T. Hahm and S. Wuβow. Turbulent wakes in wind farm configuration. European Wind Energy Conference & Exhibition, 2006.
- [48] U. Hassan. A wind tunnel investigation of the wake structure within small wind turbine farms. 1992. E/5A/CON/5113/1890. UK Department of Energy, ETSU.
- [49] J. Hobson and A. Brown. Large-eddy simulations of neutrally stratified flow over surfaces with spatially varying roughness length. *Q. J. R. Meteorol. Soc.*, 125:1937–1958, 1999.
- [50] J. Hunt. Length scales in stably stratified turbulent flows and their use in turbulence models. *aaa*, pages 285–321, 1988.
- [51] L. Ivanova and E. Nadyozhina. Numerical simulation of wind farm influence on wind flow. *Wind Energy*, 24:257–269, 2000.
- [52] N. Jensen. A note on wind turbine interaction. *Riso-M-2411, Risoe National Laboratory, Roskilde, Denmark, 16 pp.*, 1983.
- [53] N. O. Jensen. Change of surface roughness and the planetary boundary layer. *Q. J. R. Meteorol. Soc.*, 104:351–356, 1978.
- [54] J. Jimenez. Turbulent flows over rough walls. *Ann. Rev. Fluid Mech.*, 36:173–196, 2004.
- [55] I. Katic. A simple model for for cluster efficiency. *Proc. European Wind Energy Association Conf. and Exhibition, Rome, Italy*, pages 407–409, 1986.

- [56] D. Keith, D. J. Denkenberger, D. Lenschow, S. Malyshev, S. Pacala, and P. Rasch. The influence of large-scale wind-power on global climate. *Proceeding of National Academy of Sci.*, 101:16115, 2004.
- [57] B. C. Khoo, Y. T. Chew, C. P. Lim, and C. J. Teo. Dynamic response of a hotwire anemometer. part i: A marginally elevated hotwire probe for near-wall velocity measurements. *Meas. Sci. Tech.*, 9:751–763, 1998.
- [58] H. Lettau. Note on aerodynamic roughness-parameter estimation on the basis of roughness-element description. *J. of Appl. Meteorol.*, 8:828–832, 1969.
- [59] C. Lin and W. Glendening. Large eddy simulation of an inhomogeneous atmospheric boundary layer under neutral conditions. *J. Atmos. Sci.*, 59:2479–2497, 2002.
- [60] M. Magnusson and A. Smedman. Air flow behind wind turbines. *J Wind Eng Ind Aerodyn*, 80:169–189, 1999.
- [61] L. Mahrt. Stratified atmospheric boundary layer and breakdown of models. *Theor. Comput. Fluid Dyn.*, 11:263–279, 1998.
- [62] I. Marusic and W. Heuer. Reynolds number invariance of the structure inclination angle in wall turbulence. *Phys. Rev. Lett.*, 99(11), 2007. DOI:10.1103/PhysRevLett.99.114504.
- [63] I. Marusic, G. Kunkel, and F. Porté-Agel. Experimental study of wall boundary conditions for large-eddy simulation. *J. Fluid Mech.*, 446:309–320, 2001.
- [64] P. Mason and N. Callen. On the magnitude of the subgrid-scale eddy coefficient in large-eddy simulations of turbulent channel flow. *J. Fluid Mech.*, 162:432–462, 1986.
- [65] P. J. Mason. The formation of areally-averaged roughness lengths. *Q. J. R. Meteorol. Soc.*, 114:399–420, 1988.

- [66] D. Medici and P. Alfredsson. Measurement on a wind turbine wake: 3d effects and bluff body vortex shedding. *Wind Energy*, 9:219–236, 2006.
- [67] D. Medici and P. Alfredsson. Measurement behind model wind turbines: further evidence of wake meandering. *Wind Energy*, 11:211–217, 2008.
- [68] D. Milborrow. The performance of arrays of wind turbines. *J Ind Aerodyn*, 5:403–430, 1980.
- [69] C. Moeng. A large-eddy simulation model for the study of planetary boundary-layer turbulence. *J. Atmos. Sci.*, 46:2311–2330, 1984.
- [70] A. S. Monin and A. M. Obukhov. Basic laws of turbulent mixing in the ground layer of the atmosphere. *Trans. Geophys. Inst. Akad. Nauk. USSR*, 151:163–187, 1954.
- [71] E. Morfiadakis, G. Glinou, and M. Koulouvari. The suitability of the von karman spectrum for the structure of turbulence in a complex terrain wind farm. *J Wind Engin*, 62:237–257, 1996.
- [72] P. J. Mulhearn. A wind-tunnel boundary layer study of the effects of a surface roughness change: Rough-to-smooth. *Boundary-Layer Meteorol.*, 15:3–30, 1978.
- [73] S. Nemoto. Some considerations on the atmospheric internal boundary layer over the ground surface. *Meteor. and Geophys.*, 23:121–134, 1972.
- [74] Y. Ohya. Turbulence structure in a stratified boundary layer under stable conditions. *Boundary-Layer Meteorol.*, 83:139–161, 1997.
- [75] Y. Ohya. Wind-tunnel study of atmospheric stable boundary layers over a rough surface. *Boundary-Layer Meteorol.*, 98:57–82, 2001.

- [76] Y. Ohya, R. Nakamura, and T. Uchida. Intermittent bursting of turbulence in a stable boundary layer with low-level jet. *Boundary-Layer Meteorol.*, 126:349–363, 2008.
- [77] V. Okulov and J. Sorensen. Stability of helical tip vortices in a rotor far wake. *J. Fluid Mech.*, 576:1–25, 2007.
- [78] H. A. Panofsky and A. A. Townsend. Change of terrain roughness and the wind profile. *Q. J. R. Meteorol. Soc.*, 90:147–155, 1964.
- [79] V. C. Patel. Calibration of the preston tube and limitations on its use in pressure gradients. *J. Fluid Mech.*, 23:185–208, 1965.
- [80] I. Pérez, M. García, M. Sánchez, and B. De Torre. Analysis and parameterisation of wind profiles in the low atmosphere. *Solar Energy*, 78:809–821, 2005.
- [81] U. Piomelli and E. Balaras. Wall-layer models for large-eddy simulations. *Ann. Rev. Fluid Mech.*, 34:349–374, 2002.
- [82] U. Piomelli, J. Ferziger, P. Moin, and J. Kim. New approximate boundary conditions for large eddy simulations of wall bounded flows. *Phys. Fluids*, 1:1061–1068, 1989.
- [83] D. Quarton and J. Ainslie. Turbulence in wind turbine wakes. *J Wind Engin*, 14:15–23, 1989.
- [84] S. Rajagopalan and R. Antonia. Some properties of the large structure in a fully developed turbulent duct flow. *Phys. Fluids*, 22:614–622, 1979.
- [85] K. S. Rao, J. C. Wyngaard, and O. R. Cote. The structure of the two-dimensional internal boundary layer over a sudden change of surface roughness. *J. Atmos. Sci.*, 31:738–746, 1973.

- [86] A. Rosen and Y. Sheinman. The power fluctuations of a wind turbine. *J Wind Eng Ind Aerodyn*, 59:51–68, 1996.
- [87] S. Roy and R. Avissar. Scales of response of the convective boundary layer to land-surface heterogeneity. 27:533–536, 2000.
- [88] S. Roy, S. Pacala, and R. Walko. Can large wind farms affect local meteorology? *J. Geophys. Res.*, 109:D19101, 2004.
- [89] S. Savelyev and P. Taylor. Internal boundary layers: I. height formulae for neutral and diabatic flows. *Boundary-Layer Meteorol.*, 115:1–25, 2005.
- [90] H. Schlichting. Boundary layer theory. *McGraw-Hill*, page 817, 1968.
- [91] U. Schumann. Subgrid scale model for finite difference simulations of turbulent flows in plane channels and annuli. *J. Comp. Phys.*, 18:376–404, 1975.
- [92] Y. Sheinman and A. Rosen. A dynamic model of the influence of turbulence on the power output of a wind turbine. *J Wind Eng Ind Aerodyn*, 39:329–341, 1992.
- [93] A. Smedman, U. Högström, and H. Bergström. Low level jets - a decisive factor for off-shore wind energy siting in the baltic sea. *J Wind Engin*, 20:137–147, 1996.
- [94] R. Smith. Gravity wave effects on wind farm efficiency. *Wind Energy*, page doi:10.1002/we.366, 2009.
- [95] R. Stoll and F. Porté-Agel. Dynamic subgrid-scale models for momentum and scalar fluxes in large-eddy simulations of neutrally stratified atmospheric boundary layers over heterogeneous terrain. *Water Resources Res.*, 42:W01409, 2006.
- [96] R. Stoll and F. Porté-Agel. Effect of roughness on surface boundary conditions for large-eddy simulation. *Boundary-Layer Meteorol.*, 118:169–187, 2006a.
- [97] R. Stull. An introduction to boundary layer meteorology. *Kluwer Academic Pubs*, page 670, 1988.

- [98] P. A. Taylor. Comments and further analysis on effective roughness lengths for use in numerical three-dimensional models. *Boundary-Layer Meteorol.*, 39:403–418, 1987.
- [99] A. A. Townsend. The response of a turbulent boundary layer to abrupt changes in surface conditions. *J. Fluid Mech.*, 22:799–822, 1965.
- [100] G. van der Berg. Wind turbine power and sound in relation to atmospheric stability. *Wind Energy*, 11:151–169, 2008.
- [101] V. Venugopal, F. Porté-Agel, E. Foufoula-Georgiou, and F. Carper. Multiscale interactions between surface shear stress and velocity in turbulent boundary layers. *J. Geophys. Res.*, 108:00–00, 2003.
- [102] L. Vermeer, J. Sorensen, and A. Crespo. Wind turbine wake aerodynamics. *Prog. Aerospace Sci.*, 39:467–510, 2003.
- [103] P. Vermeulen. An experimental analysis of wind turbine wakes. 1980. Third International Symposium on Wind Energy Systems. BHRA. 1980.
- [104] T. von Kármán. Progress in the statistical theory of turbulence. 34:530–539, 1948.
- [105] P. Vukoslavcevic and J. Wallace. The simultaneous measurement of velocity and temperature in heated turbulent air flow using thermal anemometry. *Meas. Sci. Tech.*, 13:1615–1624, 2002.
- [106] A. Wessel and B. Lange. A new approach for calculating the turbulence intensity inside a wind farm. 2004. In Proceedings of the Deutschen Windenergiekonferenz (DEWEK), Wilhelmshaven.
- [107] J. Wieringa. Roughness-dependent geographical interpolation of surface wind speed averages. *Q. J. R. Meteorol. Soc.*, 112:867–889, 1986.

- [108] D. H. Wood. Internal boundary layer growth following a step change in surface roughness. *Boundary-Layer Meteorol.*, 22:241–244, 1982.